Title
Systems and Synthetic Biology Approaches to Mechanobiology

Author
Hughes, Jasmine Hannah

Publication Date
2018

Peer reviewed|Thesis/dissertation

Systems and Synthetic Biology Approaches to Mechanobiology

By

Jasmine Hannah Hughes

A dissertation submitted in partial satisfaction of the

requirements for the degree of

Joint Doctor of Philosophy

with the University of California, San Francisco

in

Bioengineering

in the

Graduate Division

of the

University of California, Berkeley

Committee in charge:
Professor Sanjay Kumar, Chair
Professor Matthew Welch
Professor Zev Gartner

Spring 2018

Abstract

Systems and Synthetic Biology Approaches to Mechanobiology

By

Jasmine Hannah Hughes

Joint Doctor of Philosophy in Bioengineering
With the University of California, San Francisco

University of California, Berkeley

Professor Sanjay Kumar, Chair

Over the last several decades, it has become increasingly clear that cells throughout the body sense and respond to mechanical and biophysical cues and actively apply forces to their surroundings. Mechanobiologists have developed an increasingly clear picture of how this signal transduction occurs. However, many questions have been challenging to answer due to the often nonlinear relationships between protein activity and cell function and due to the crosstalk with other signaling pathways. Over the same period of time, the fields of synthetic biology, which aims to create de novo signaling systems using biological parts, and systems biology, which aims to describe cell behavior from a holistic perspective, have become rich fields with new tools for understanding and controlling cell behavior.

We first apply an inducible promoter system to answer fundamental questions about the regulation of stress fiber viscoelasticity. MLCK and the rho-associated kinases 1 and 2 (ROCK1 and 2) both activate myosin's motor activity through phosphorylation of its regulatory light chains (RLCs), and these light chains can be phosphorylated once at serine 19 (p-RLC) or twice at serine 19 and threonine 18 (pp-RLC). Prior on-off approaches using pharmacological inhibitors showed that these kinases act on distinct pools of stress fibers, with MLCK inhibition primarily regulating the viscoelastic properties of peripheral stress fibers and ROCK inhibition primarily influencing those of central stress fibers. It was unclear, however, whether these kinases had distinct effects on the two RLC phosphorylation states and how these phosphorylation states influenced these populations of stress fibers. To answer these questions, we stably transduced cells with a doxycycline-inducible promoter governing the expression of constitutively active (CA) mutants of ROCK or MLCK. By varying the concentration of doxycycline in the cell culture media, we show that graded MLCK activity produces a graded increase in p-RLC, which localizes to peripheral SFs. In contrast, graded ROCK activity produces a graded increase in pp-RLC, which localizes to central SFs. Viscoelasticity measurements of individual stress fibers through subcellular laser ablation further reveal that MLCK and ROCK regulate the mechanical properties of peripheral and central stress fibers, respectively, with phosphomimetic mutants phenocopying these findings. Interestingly, we observe nonlinear relationships between levels of phosphorylation and viscoelasticity parameters, demonstrating the power of our synthetic biology approach.

Next, we build on this toolkit by incorporating CRISPR-Cas9 gene editing to remove the endogenous protein. This strategy permits us to probe the relationship between a protein of interest and its role in cell signaling along a gradient of values from virtually zero activity to supraphysiological levels. We apply this approach to MLCK, allowing us to modulating p-RLC activity. Interestingly, we find that knockout of endogenous MLCK has very little effect on levels of p-RLC or on mechanobiological phenotypes like migration and focal adhesion formation, but that these phenotypes are sensitive to overexpression of CA-MLCK. One possible explanation is that the smooth muscle MLCK isoform, which is expressed from the same gene as the full-length non-muscle MLCK isoform but from an internal promoter site, is able to compensate for the loss of non-muscle MLCK.

Finally, we turn to the systems biology toolkit to determine why patient-derived stem-like glioblastoma (GBM) tumor-initiating cells (TICs) show reduced sensitivity to mechanical cues. GBM's poor prognosis is associated with a subpopulation of cells that share characteristics with neural stem cells in that they are able to self-renew and differentiate in response to morphogens. These cells are highly invasive and evade treatment, differentiating to re-establish the heterogenous tumor population after treatment. Prior work by our lab and by others found that some of these TICs are insensitive to mechanical cues, with reduced mechanosensitivity correlating with increased invasiveness. Furthermore, we previously found that differentiation of these cells with bone morphogenetic protein 4 (BMP4), which greatly limits their tumor-initiating capacity, sensitizes TIC spreading to substrate stiffness. In this chapter, we use RNA sequencing to identify transcriptomic changes in response to different matrix mechanical properties and to differentiation. We find that BMP4 suppresses expression of proteins associated with extracellular matrix signaling. Interestingly, we find that matrix stiffness has a pronounced effect on metabolic function, with stiff gels promoting expression of oxidative phosphorylation genes. This finding is not impacted by differentiation state, although the number of genes influenced by gel stiffness is amplified in differentiated cells. Guided by these bioinformatics analyses, we then inhibited oxidative phosphorylation, finding that cell spreading was dependent on ATP synthase activity in a stiffness- and differentiation-dependent manner. Together, this work integrated systems biology tools with mechanobiology assays to yield new insight into how morphogens influence mechanical signaling in GBM TICs.

I am grateful to my many mentors. First and foremost, Professor Sanjay Kumar; for his guidance through my doctoral work, and particularly for his optimism and steadiness when I encountered seemingly devastating problems with some of our biological tools. My other committee members; Professors Matt Welch and Zev Gartner, for their generosity in lending their expertise to my own research, and for helping me to identify the last few steps in wrapping up my dissertation and to navigate challenges I encountered in my PhD. Professor Tamara Alliston and Professor John Dueber, unofficial mentors in my role as president of the Bioengineering Association of Students, for being great role models for nurturing a healthy academic community. Kumar lab and Schaffer lab members past and present; Badri Ananthanarayanan, Andrew Rape, Yushan Kim, Joanna Mackay, Elena Kassianidou, Alyssa Rosenbloom, Kelsey Springer, Kayla Wolf, George Lin, Michael Kang, Jess Lee, Phil Kang, Stacey Lee, Andy Lopez, Joe Chen, Sophie Wong; for their help and support in the technical side as well as the emotional side of graduate school and bioengineering research. My mentors that have taught me to be a mentor teacher and mentor myself, Terry Johnson, Linda Von Hoene, Sabrina Soracco. For nurturing my interest in science as a very young scientist; Linda Meulenbroek, Professor Elizabeth Jones, Professor Richard Leask, Professor Tom Quinn, Professor Leonie Rouleau, Sarah Al-Roubaie.

I am also grateful for my support network. A special nod to my fellow bioengineering graduate students, and to the members of Beyond Academia. Community is important, and through my work with BEAST and Beyond Academia I have tried to make a great graduate student community even better. Thank you also to my family, my friends, and my partner – for being so understanding of the demands of a PhD and for encouraging me to balance these demands with recreational pursuits too, sometimes.

Chapter 1:
Introduction to Synthetic & Systems Mechanobiology

Jasmine H. Hughes[1,2] and Sanjay Kumar[1,2,3]*

[1] Department of Bioengineering, University of California, Berkeley
[2] UC Berkeley – UCSF Graduate Program in Bioengineering
[3] Department of Chemical and Biomolecular Engineering, University of California, Berkeley

Parts of this chapter have previously been published as "Synthetic mechanobiology: Engineering cellular force generation and signaling" in *Current Opinion in Biotechnology* (2016, 40: 82-89) and are reprinted here with permission.

Introduction

Cells sense mechanical and other biophysical properties of their environment, altering their morphology, migration and differentiation in response. In turn, cells also influence microenvironmental structure and mechanics by secreting, digesting and remodeling matrix components. This dynamic mechanobiological relationship features centrally in development, tissue homeostasis, and disease progression (1–3).

To explore and control these processes, a wide range of approaches for engineering the cellular microenvironment have been developed. There are increasingly sophisticated techniques for independently varying combinations of topographical cues, ligand density and ligand type, and substrate elasticity and viscoelasticity. These studies have shed considerable insight into the role biophysical signals play at molecular, cell, tissue and developmental scales. We now have a strong framework describing the general process by which mechanical and biophysical signals are transduced into phenotypic and epigenetic changes, and the field that studies this process has been called mechanobiology.

As the field of mechanobiology developed, technological advances in genetic engineering as well as in DNA sequencing and mass spectroscopy have given rise to the fields of synthetic biology and systems biology. Synthetic biology aims to build new artificial signaling pathways from protein and nucleic acid components, providing a powerful toolkit for engineering specific cell behaviors to target diseases or to expand our understanding of biological processes. Systems biology incorporates high-throughput assays, computer science and statistics to study the interactions between many biological components at a holistic level. It is only in more recent years that mechanobiology has begun to apply aspects of synthetic biology to control mechanobiological signaling pathways from within the cell instead of “outside-in” engineering of the microenvironment. More limited still has been the application of systems biology tools to mechanobiology, constrained in part by the difficulty in obtaining high-throughput read-outs of mechanobiological phenotypes and the challenges in modeling cells simultaneously at the biochemical level and at the biomechanical level.

In this chapter, I explore recent developments in mechanobiology in which synthetic and systems biology tools have been leveraged. I will first discuss recent advances in which genetic engineering and protein engineering strategies have been created to control mechanobiological phenotypes, such as migration and force generation, with a particular eye towards their temporal and spatial resolution. Second, I will discuss the application of bioinformatics and systems biology strategies to mechanobiology, highlighting challenges unique to mechanobiology.

Synthetic Mechanobiology:

Engineering cellular force generation and signaling

Complex phenotypes often arise from the activation of signals at specific times and places within tissue (or nanoscale regions of cells), and so comprehensive control of mechanobiological behaviors requires precise modulation of these signals over a wide range of spatial and temporal scales. For instance, whereas stress-induced activation of Src occurs over a few hundred milliseconds (4), mechanically-driven stem cell differentiation responds to stimuli presented over the course of several hours or days. Furthermore, because signaling events are frequently associated with accumulation of a molecular effector to some critical, local concentration (5–7) the duration of a signaling event is important in driving phenotype (8). Similarly, gradients in biophysical cues and signaling molecules are important for facilitating cell polarity and directing migration (9, 10).

In this section, we explore inside-out control of mechanobiological signaling and phenotype, with emphasis on spatial specificity and temporal dynamics. First, we will discuss studies that direct cell behavior by changing the expression of a target protein. Second, we will explore strategies that control behavior by changing the activity of a target protein. In the former category, we focus on inducible/repressible gene expression systems in which mechanotransductive signals are placed under the control of soluble inputs. In the latter category, we emphasize small-molecule induction of protein complexation. We then consider technologies in which nominally mechanotransductive signaling systems are re-engineered to be induced by non-mechanical inputs such as light and magnetic fields.

Controlled Induction of Gene Expression

Gene transcription represents an early point of control in regulating protein abundance and therefore activity. A range of conditional promoter systems have been deployed in mammalian cells, most of which place the transcription of specific genes under the control of light (11, 12) or small molecules that can be added to the culture medium, such as antibiotics (13, 14), steroid hormones (15, 16), or metabolites (17, 18). These systems are typically reversible, such that removal of the stimulus restores expression to basal levels. While these systems allow control of expression rates, they neither directly control protein activity levels nor evade native cell regulatory mechanisms.

To apply these strategies to mechanobiological signaling while circumventing endogenous feedback regulation, our laboratory has placed constitutively active (CA) mutants of key mechanotransductive genes under the control of conditional promoters. In an early effort, we used lentiviral delivery to create stable human glioma cell lines that express CA RhoA or CA myosin light chain kinase (MLCK) under the control of a tetracycline-repressible promoter. By varying the concentration of tetracycline in the medium, we achieved stably graded expression levels of these proteins. Moreover, because both RhoA and MLCK promote activation of the actin cytoskeletal motor myosin II, we were able to apply this strategy to control a variety of mechanobiological phenotypes in a graded and stable way, including random migration speed, cortical stiffness and traction force generation (19).

Provided mutually orthogonal promoters are selected, this strategy can be multiplexed to independently and simultaneously control several target proteins. This approach could allow for engineering more complex mechanobiological behavior, or permit one to map the "phase space" that describes how multiple proteins interact to control cell phenotype. For example, we used dual lentiviral transduction to simultaneously express CA RhoA and CA Rac1 under the control of doxycycline- and cumate-inducible promoters, respectively (20). These GTPases are canonically regarded to regulate opposing aspects of cell motility and mutually antagonize one another at several levels, making it challenging to independently manipulate them. By using this orthogonal promoter strategy, we circumvented this crosstalk and mapped the range of phenotypes observed in the otherwise inaccessible state of high-RhoA activation and high-Rac1 activation.

Inducible/repressible promoter strategies offer a number of important advantages, including highly stable expression and the ability to uniformly control gene expression in an entire population of cells, and in an easily scalable way. However, there are also a number of limitations, perhaps the most important of which is the slow dynamics of the expression system and the protein of interest. While in some scenarios, cells respond phenotypically within six hours (19, 21), some systems may take as long as ten days to reach a steady-state response (21, 22). This is compounded by system-to-system variations in the kinetics of transcriptional activation, protein folding and post-translational modifications, protein transport, and protein degradation, all of which may be key to the final phenotype.

Additionally, this strategy has inherently limited spatial resolution. Once the gene has been transcribed, there is no control over subcellular protein localization. However, several approaches for spatial control of gene expression at the cell population level have been proposed. For instance, inducers and repressors can be restricted to certain areas of a cell population through microfluidic control (22), by occlusion of membrane pores (21), or by sequestration of the agent within the material scaffold (23, 24). Several factors influence the extent of control over spatial activation of gene expression and thus pattern fidelity. Cell migration and slow delivery, induction, and expression kinetics may disrupt intended patterns. Shorter lag times between introduction of the inducer/repressor and protein expression allows for more faithful pattern formation (21).

Controlled Activation of Protein Activity

While modulating gene expression can produce graded and reversible changes in cell mechanobiology, the response time of this system is limited by transcription and translation rates as well as by protein and mRNA degradation rates. As a result, these approaches are most relevant for modulating processes that occur on time scales of hours to days or at a steady-state of protein activity. Direct control of protein activity, on the other hand, can influence signaling and thus cell behavior on the scale of seconds to minutes. Importantly, these rapid kinetics may also better replicate time scales associated with soluble ligand-induced signaling in cells (e.g. growth factors). Several techniques for selective activation of target proteins have been devised and are beginning to be applied to mechanobiology, including chemical, optical, and magnetic actuation.

Chemically Induced Protein Activity

One commonly employed chemical actuation system is to bring two proteins of interest into proximity through chemically induced dimerization (CID), such as the rapamycin-induced dimerization of FK506 binding protein (FKPB) and FKBP rapamycin-binding domain (FRB). In this approach, FKBP and FRB are each genetically fused to two target proteins. Subsequent addition of the small molecule rapamycin to the culture then induces the association and binding of the two proteins, triggering downstream signaling events. This approach also allows for control of protein localization by fusing one of these domains to an organelle-targeting domain. For example, by fusing FKBP to a membrane-localization sequence, FRB-RhoA and FRB-Rac chimeras have been recruited to the cell membrane upon addition of rapamycin, leading respectively to cell contraction and membrane ruffling (25).

Further refinements to this approach have enabled increasingly precise control of signaling. For instance, Karginov et al. selectively activated certain branches of the Src signaling cascade by inserting FKBP into the catalytic domain of Src, thereby deactivating its kinase activity. Addition of rapamycin induced binding of this construct with FRB, which allosterically rescued kinase activity (26, 27). This protein was co-expressed with either FAK or p130Cas constructs containing FRB instead of the Src-binding domain, allowing for specific induction of FAK-mediated or p130Cas-mediated effects of Src activation. Kapp et al. used computational methods to design versions of Cdc42 and its activator intersectin that acted orthogonally to the cell's native signaling machinery and dimerized upon rapamycin addition (28). Cells expressing both synthetic signaling molecules or both wild-type Cdc42 and intersectin demonstrated increased lamellipodium formation, while cells expressing one wild-type and one synthetic protein did not form lamellipodia.

While rapamycin-induced dimerization allows for the rapid and highly specific localization and activation of proteins, these effects are largely irreversible (29). Various reversible CID systems have been reported (30, 31). Alternatively, a second, orthogonal dimerizing agent can be used to relocate a rapamycin-induced FRB-FKBP complex from the plasma membrane to mitochondrial membranes to produce a pulse of localized protein activation (32, 33).

Whereas manipulation of gene expression produces changes in protein levels on a cell-wide scale, chemically-induced dimerization offers the opportunity to manipulate protein activity through the directed delivery of the inducer (e.g. rapamycin). Variants of these dimerization inducers can be conjugated with photocleavable domains that greatly reduce inducer activity through steric hindrance or by blocking passage through the cell membrane (34–37). Within a few minutes of illumination, the inactivating conjugate is released, allowing the inducers to enter the cell or enabling the dimerizing agent to catalyze dimerization. This strategy has been used to control the location of membrane ruffling (34, 35), extension of cell processes (36) and protein localization (37). An attractive feature of this approach is its potential for multiplexing, in that photocleavage occurs over a fairly narrow window of wavelengths (which can itself be tuned to different wavelengths), thus allowing for orthogonal activation of dimerization of more than one set of proteins (36). Microfluidic devices present an alternative method for spatial control over inducer delivery. Lin et al. cultured cells containing rapamycin-activatable Rac constructs in fluidically engineered cell-length rapamycin gradients and found that asymmetry in Rac activation could direct cell polarity and migration (38).

An alternative approach to chemical induction of protein activity is to design proteins that recognize exogenous ligands. Park et al. expressed in motile cells an engineered G protein receptor that responds solely to clozapine-*N*-oxide. This molecule acted as a chemotactic cue, directing cell migration towards areas of higher concentration. T-lymphocytes expressing this construct honed to CNO-releasing beads implanted in mice (39).

Optically Induced Protein Activation

The integration of light-sensitive domains in protein engineering has given rise to the field of optogenetics. These protein domains undergo conformational changes in response to absorption of light of a particular wavelength. These photoreceptors vary in their wavelength sensitivity, photochemical kinetics and activation mechanism. Some photoreceptors heterodimerize in response to the light-induced conformational change, allowing engineering approaches similar to those used with CID. Light oxygen voltage (LOV) photoreceptors operate through steric hindrance; proteins of interest can be fused to the C-terminal alpha helix, which unwinds in a light-induced conformational change. Light-gated ion channels, notably channelrhodopsins, open to allow the flow of ions in response to illumination. Non-channel classes of light actuators and their application to cell motility have been recently reviewed (40).

As with chemical induction of protein activity, light induction is rapid; depending on the photoreceptor system used, activation occurs on the order of one second. Importantly, many light-inducible systems are reversible, with light-induced states having a half-life of 10 seconds to 10 minutes. Optical induction also allows for precise spatial control over protein activation, and can target single cells or a specific region within a cell. Optical signals are minimally invasive and can reach cells embedded in three-dimensional materials and living tissue (41–43).

Light-gated ion channels offer a particularly elegant system for studying calcium-induced mechanobiological phenotypes such as muscle cell contraction. Bruegmann and coworkers expressed EYFP-tagged channelrhodopsin-2 (ChR2) in mice (44, 45). Illumination with blue light induced membrane depolarization and calcium influx in isolated cardiomyocytes and depolarized cardiomyocytes in live mouse hearts(44). Skeletal muscle explants contracted, and the magnitude of force generated could be modulated based on the intensity and duration of the light pulses (45). Sakar et al. differentiated skeletal muscle myoblasts expressing ChR2 in matrigel-collagen gels formed around Polydimethylsiloxane (PDMS) cantilever pairs (46). Optically stimulated myotubes generated contractile forces, quantified through cantilever deflection. This activation could be spatially restricted to single myotubes or expanded to target multiple myotubes, allowing for control over axial and rotational force generation in these devices.

An offshoot of this approach is to use protein engineering to create novel calcium-dependent signaling. Mills et al. fused calmodulin, which is activated when bound to calcium ions, to the GTPases Cdc42, Rac1 and RhoA (47, 48). By controlling calcium influx with an engineered light-sensitive calcium channel (49), the authors could direct filopodial extension and cell migration.

Magnetically Induced Protein Activity

In general, the above strategies all require some degree of gene/protein engineering, which may not be appropriate or even feasible in all systems. An appealing alternative is the use of functionalized magnetic nanoparticles (MNP) to activate signaling cascades by physically clustering signaling molecules. Originally restricted to cell-surface receptors (50, 51), recent efforts have used microinjection and other methods to place the MNP inside the cell.(52, 53) These particles can then be localized to an area of interest by application of a field with a magnetic tip (50, 54), or can been arranged into a concentration gradient (55, 56). Importantly, this process is rapid, occurring over seconds to minutes, and reversible, with particles dispersing after removal of the magnetic field.

In vitro functionalization of MNPs is challenging for large protein complexes that cannot be easily expressed and isolated from bacterial cultures. Etoc and coworkers addressed this issue by functionalizing MNPs in situ by injecting MNPs coated with a HaloTag ligand into cells expressing a protein of interest fused with HaloTag (53). HaloTag binds to its ligand irreversibly, recruiting the target protein to the MNP. Cdc42-functionalized MNPs concentrated with a magnetic field localized actin polymerization while membrane-bound Rac1 signaling was dynamically modulated by bringing MNPs functionalised with the Rac1 activator TIAM1 into and out of membrane proximity.

Synthetic Mechanobiology: Future Outlook

Mechanobiological behaviors are regulated by temporally and spatially precise cues. Depending on the phenotype of interest, a variety of strategies are available for controlling cell force generation and signaling. Small-molecule induction of gene expression represents one approach but only produces behavioural changes on the order of hours to days and does not offer subcellular resolution. On the other hand, direct control of protein activity allows for much more rapid actuation of signaling events, and incorporation of exogenous cues such as magnetic probes or light allows for subcellular control over protein activity. MNPs may also present translational advantages, since clinical applications of certain magnetic nanoparticles are already approved (57).

The advances discussed above are relatively simple implementations of genetic parts. Complex synthetic circuits that incorporate multiple responsive elements in series and parallel have been applied towards other ends. For example, a proof-of-concept study in HEK and Jurkat T cells synthesized 113 computational circuits, allowing for detection of multiple inputs and conditional expression of multiple fluorescent proteins (58). To increase the complexity of synthetic mechanobiology circuits, one important advance will be the design of synthetic mechanical actuators that can translate a force into a biological signal independent of endogenous signaling mechanisms. A possible approach could be to engineer existing molecular mechanical actuators, such as talin (59), to bind to target molecules that must be activated by proximity to each other.

Rewiring or tuning mechanobiological signaling circuits could have useful medical applications. For example, this approach could allow correction or control of mechanically-driven cell behavior in instances where inserting a scaffold or otherwise modifying the extracellular environment is impractical or impossible. Proof-of-principle experiments have shown that optical and chemical actuation of signals can control cell mechanobiology in vivo. A challenging but critical next step

will be to explore the use of these approaches in living organisms, with an eye towards eventual clinical use.

Systems Mechanobiology:

Incorporating forces into biochemical models of the cell

Systems biology seeks to understand how biological components interact and are integrated to produce a particular biological outcome. A typical project workflow is to begin with a large, annotated dataset, and to then use this dataset to generate predictive and testable hypotheses about important pathways or disease biomarkers or other outputs, through the application of statistics and/or mathematical models. One example dataset is the yeast deletion collection, an open-access systematic and complete set of over 21,000 mutant strains (60). The phenotype of a given mutation is probed by assessing the strains' growth rates, possibly in the presence of one or more chemicals. With an eye towards robust and reproducible measurements, a number of algorithms and pipelines were developed to identify gene interactions (60–62) and this collaborative project greatly improved our understanding of signaling systems in yeast (60). In more recent years, massively collaborative projects have begun to fully map human cells, taking advantages of genomics, genetic editing technologies and advanced microscopy techniques (63, 64). The ability to relatively easily perform genome-wide screens for gene contributions to phenotypes is further spurring systems-level characterization of cell biology (65).

While classical biology approaches have furnished us with considerable knowledge regarding the key players in mechanobiology, our understanding of how these molecules interact to produce mechanobiological outputs like cell migration or force generation could be much expanded through the application of systems biology techniques. Indeed, bioinformatics approaches famously identified YAP and TAZ as mechanosensitive transcription factors (66) in what is now one of the seminal works of mechanobiology with over 1500 citations. However, mechanobiology provides a number of unique challenges or hurdles compared to other fields in which systems biology has been applied. In this section, I will explore challenges unique to systems mechanobiology and approaches that are being developed to address these limitations. I will then describe some of the recent findings in systems mechanobiology.

Challenges in Systems Mechanobiology

Systems-level descriptions of cells incorporating mechanical signaling are difficult to test without a way to systematically generate a dataset with independent mechanobiological variables and/or dependent mechanobiological outcomes at high throughput. While mechanobiology can readily make use of library generation methods used in other fields, such as siRNA libraries or CRISPR gRNA libraries (67–69), it is the difficulty in presenting mechanical and biophysical stimuli and assessing mechanobiological readouts at high-throughput rates and in complex with proteomic or genomic information that particularly limits systems approaches in mechanobiology.

High Throughput Modulation of Mechanical Stimuli

The mechanobiology toolkit now encompasses a vast array of methods to modulate mechanical and biophysical properties. While these strategies have become powerful tools for probing the effects of a handful of proteins on mechanobiological processes, scale-up of these fabrication methods on a scale applicable to, for example, an entire library of knockouts will prove challenging. Varying just ECM protein coating is scalable, if not inexpensive, since it is straightforward to either manually or automatically pipette specific protein solutions into a well or into a micro-array prior to seeding cells (70). However, modulation of stiffness, by altering the extent of crosslinking or density of hydrogels such as polydimethylsiloxane (PDMS), polyacrylamide (PA) or hyaluronic acid, is more challenging. One of the major bottlenecks is that for two-dimensional gels it typically is necessary to polymerize or cure the hydrogel between a functionalized surface and a repellant surface to ensure a sufficiently smooth and flat surface, allowing for imaging-based assays and to present the cells with uniform mechanical cues. This approach is labor-intensive and demands no small amount of skill and dexterity. A number of innovations have been made to increase gel throughput. For example, borrowing nanofabrication technologies from the semiconductor industry, micropillars of varying stiffnesses and ECM coatings can be made by varying pillar height and by stamping the pillars with protein gradients (71, 72). Another approach is to punch smaller gel inserts out of a larger gel, reducing the amount of manual manipulation and allowing for culture in a 96-well plate or other small culture area (73–75). Alternatively, stiffness and matrix coating can be individually modulated within the same gel through orthogonal cross-linking strategies (76, 77) or by gel composition gradients (78). Perhaps most conducive to automated cell culture apparatus are strategies that polymerize gels directly within 96-well or 384-well plates, using specialized inserts for controlling surface smoothness during polymerization (79). Highly customized fluid handlers have been applied to encapsulate cells within environments that incorporate several independent ECM parameters (80).

High Throughput Mechanobiological Characterization

Mechanobiological phenotypes require special consideration for analysis in high-throughput. Traction force microscopy, in which the displacement of fluorescent beads embedded within the gel is used to calculate cellular force generation, is a highly informative assay that has been applied to great improve our ability to model mechanotransduction (81, 82), however the computational demands of particle imaging velocimetry and Fourier transforms may be limiting for large sample sizes. One alternative force generation assay is the use of a molecular tension sensor, in which fluorescence resonance energy transfer (FRET) is harnessed to produce a fluorescent readout when a protein is subject to a change in stretch. Tension sensors have been created to measure forces transmitted extracellularly or intracellularly (83–85). Experimental design may be limited by difficulty in pairing the use of FRET with other fluorescent markers due to fluorescent channel overlap.

Cell migration is perhaps more difficult to interpret since this process requires the coordination of focal adhesion assembly and disassembly, contractile force generation and protrusion force generation, and cell polarization. However, data collection and analysis is relatively straightforward; cell movement speed and persistence can be quantified from time lapse image series without the use of fluorescence microscopy or labelling (86). Even more technically simple

to implement is cell area or other cell shape descriptors, which requires just single images and can be easily incorporated into other imaging-based assays. This read-out has previously been used in an RNA interference screen for changes in mechanotransduction (87). However, like migration, cell area integrates many diverse mechanobiological processes and is also influenced by cell division and death, complicating interpretation of this readout. Many other workhorses of mechanobiology require manipulation of individual cells in ways that are challenging to automate, such as micropipette aspiration (88), laser ablation (89) and atomic force microscopy (90).

For probing pathways and processes for which a gene target is already known, a reporter line could be harnessed and conventional approaches like flow cytometry used to assess the impact of a mechanobiological manipulation on this pathway. One well-characterized mechanotransduction pathway is the YAP-TAZ/β-catenin cascade, which activates the T-cell factor (TCF) target promoters. TCF reporter lines have been used to understand abrogation of mechanotransduction during chronic inflammation (91) and to study transduction of mechanical strain cues (92).

Perhaps the most promising avenue for high-throughput characterization of cell mechanobiology is the incorporation of microfluidic devices. Forces can be applied to cells by moving them through constrictive channels or through the use of pneumatic valves (93–96). Mechanical information is then calculated from images of cells before and after deformation. One limitation is that cell mechanics are probed in suspension, however some efforts have been made to present suspended cells with ECM cues via cellular encapsulation (97). This approach is further strengthened by complexing with proteomic read-outs, like conventional flow cytometry (98) or single cell western blotting (99).

Data Integration in Systems Mechanobiology

Systems biology more broadly is still developing best practices for consolidating and comparing data collected from multiple sources (100). However, there exist standardized conventions and databases for referencing genes and proteins (101, 102), metabolites (103), and signalling pathways (104, 105) that facilitate this process. To fully describe a mechanical substrate would require standards for reporting on gel properties such as porosity and pore geometry, viscoelasticity, adhesion receptor identity and density, topography, degradation behavior, and swelling behavior. While mechanobiology publications will typically describe their systems in terms of one or more of these properties, differences in test methods and in data reporting can make these descriptions difficult to interpret (106). Data sharing infrastructures for systems mechanobiology may wish to adopt biomaterials testing standards such as those developed by institutions like the American Society of Mechanical Engineers (ASME) or the American Society of the International Association for Testing Materials (ASTM). Systems biology is further facilitated by resource depositions, such as Addgene for plasmids, the American Type Culture Collection (ATCC) for cell lines, or the previously mentioned yeast deletion collection for yeast knockouts. Due to difficulties in long-term storing of biomaterials without impacting their properties, it is unlikely that a biomaterials repository analogous to Addgene is ever developed, underscoring the importance of developing high-throughput, reproducible synthesis techniques.

Recent Advances in Systems Mechanobiology

Despite these challenges in characterizing mechanobiology at a systems-level, there is a burgeoning field of scientists bringing systems biology perspectives to mechanobiology. Some of these early efforts combine computational modeling of biochemical signaling with coefficients that incorporate mechanical input, or use mechanical modeling that allows for integration of chemical information. Others seek to understand these systems experimentally, applying transcriptomic or proteomic screens to understanding the impact of mechanical cues of signaling systems. Here, we discuss some of these recent studies in systems mechanobiology.

Computational Systems Mechanobiology

A key aspect of computational models in systems mechanobiology is the translation of mechanical and biochemical events to a common language. One approach is to model biochemical signaling with Michaelis-Menten kinetics but to incorporate the transduction of mechanical information in a reaction coefficient. For example, YAP/TAZ integration of mechanical and proliferative cues was computationally modelled by making phosphorylation of focal adhesion kinase (FAK) dependent on ECM elasticity (107). The degradation or synthesis of protein or of mRNA levels are a second place in which mechanical information can be incorporated. For example, lamin-A, a structural component of the nuclear lamina, and myosin II, a major component of the cytoskeletal force generation machinery, are thought to be regulated through strain-inhibited degradation (108, 109). With this approach, Dingal and Discher showed that if structural proteins such as lamin-A and myosin II activate expression of themselves under particular stiffness conditions, stable levels of expression, rather than unstable positive feedback, could be achieved provided degradation was also regulated by stiffness (110).

More complex modeling may require the incorporation of mechanics-driven models to fully capture the relationship between mechanical cues and biochemical systems. One well-developed model is the motor-clutch model, which abstracts adhesion as a stochastic model of molecular springs with stiffness-dependent loading and unloading rates (“clutches”) that link the actin-myosin cytoskeleton (“motors”) to the extracellular matrix (111, 112). Although abstract, insights from models based on this principle, combined with experimentation, have led to an improved understanding of molecular interactions at focal adhesions (81), of transduction of ligand spacing cues (82), and of integrin clustering driven by actin polymerization forces instead of myosin dependent forces (113). Using a similar model of focal adhesion formation, one group examined the effects of RNA interference on Rho- and Rac-mediated regulation of focal adhesion dynamics, a particularly interesting problem for the very different time lengths over which these processes occur and for the antagonistic signaling between RhoA and Rac1 (114).

Stress fiber generation and transmission of forces have also been modeled, treating stress fibers as contractile beams (115), or contractile element combined with non-linear spring elements (116, 117), and stress fiber assembly has been characterized with tension-dependent assembly and disassembly terms (117, 118). Combined with experimental data, this approach identified the importance of zyxin in regulating cytoskeletal transitions between fluid-like and elastic behaviors (116). More complex modelling of ECM mechanical components typically use cell-scale phenotypic changes as the integrators of chemical and mechanical cues as a simplification (119).

For example, Tepole applied a finite element model of ECM displacements under strain to look at the effects of diffusing chemokines, ECM composition and fiber orientation on cell proliferation and orientation in a wound healing context (120).

Mechanobiological interactions with cell signaling are not, however, limited to interpretation of extracellular cues. Cytoskeletal elements regulate signaling events by segregating or clustering proteins (121). To address this phenomenon, some models have been proposed that incorporate cytoskeletal spatiotemporal control of signaling by protein clustering and advective transport of signaling molecules (122, 123). With models becoming increasingly sophisticated, further insights may be garnished from feedback between biochemical and mechanical model components, such as through cytoskeletal regulation of signaling or remodelling of the matrix.

Bioinformatics in Mechanobiology

The above works have drawn heavily from insights yielded through classic biology experiments, and are sharply focused on signaling molecules canonically associated with mechanotransduction. However, mechanical signaling impinges on many other biological processes and bioinformatics experiments are beginning to shed more light on the impact of mechanical cues on a systems-level. The most prominent example of this was the work performed by Provenzano and colleagues and Dupont and colleagues. Provenzano et al. studied the role of collagen matrix density on breast cell phenotype, identifying via microarray that high density matrices promoted expression of genes associated with proliferation (124). This work was built on by Dupont et al., who identified in this dataset an enrichment for genes in the YAP/TAZ transcription factor pathway, and experimentally demonstrated nuclear localization of YAP/TAZ is a key mechanosensitive step in regulating their transcriptional activity (125).

Mirroring the development of mechanobiology in general, many bioinformatics applications in mechanobiology have occurred in the musculoskeletal and cardiovascular systems. For example, RNA sequencing of cardiac tissue subjected to different blood flow patterns identified differences in expression for 500-1000 genes, which were enriched for signalling associated with the extracellular matrix and translational elongation (126, 127). Defects in skeletal muscle formation, which delays bone ossification and reduces mechanical stimuli during bone development, alters the expression of approximately 1100 genes in developing mouse humeri cells, which show an enrichment in Wnt signaling and cytoskeletal components (128). Similarly, mechanical loading of adult mouse tibial bones altered expression of approximately 300 genes, predominately enriched for Wnt signaling and ECM-receptor interactions (129). While there are unsurprisingly tissue-dependent and stimuli-dependent components to transcriptional regulation, a common pattern emerges for mechanical stimuli regulating on the order of 100-1000 genes, with cytoskeletal or ECM components being particularly represented in these gene sets.

There have been fewer bioinformatics-driven studies where changes in mechanotransduction were mechanistically studied. One interesting report performed RNA sequencing on cells cultured on soft or stiff substrates with or without mutations in the LINC complex, which links the nucleoskeleton to the cytoskeleton (130). Intriguingly, they found that following disruption of the LINC complex, the direction of mechanosensitivity was reversed for the majority of genes that were differentially expressed across the two gel stiffnesses in control cells.

Some particularly creative applications of bioinformatics to mechanobiology have involved isolation of cellular components involved in adhesion or migration. For example, Kuo and colleagues used hypotonic shock followed by shearing away of cell bodies to isolate proteins from focal adhesions, which were then processed by mass spectrometry (131). They found that nearly three quarters of the 'adhesome' were downregulated by inhibition of actomyosin contractility. However, interestingly, they discovered that some proteins were enriched upon inhibition of contractility, the first such report of negative regulation of focal adhesion maturation by contractility. Mili and colleagues cultured cells on fibrous matrices, allowing cells to extend pseudopodia into the matrix. By scraping away the cell bodies, they were able to sequence only the mRNA present in the cell processes (132, 133). They identified a central role for adenomatous polyposis coli (APC) in regulating localization of contractility-associated mRNAs to protrusions, but also observed an APC-independent enrichment in genes associated with protein synthesis, post-translational modification and gene expression.

Bioinformatics tools have assisted in identifying signaling pathways impacted by mechanical cues, and revealed relatively modest changes at the transcriptomic level. Subcellular studies hint towards a role for localization of mRNAs as important for regulation of adhesion or migration. In recent years, additional tools have been developed to better shed light on this phenomenon, such as high-throughput in situ hybridization strategies to visualize mRNA localization (134) or ribosomal footprint sequencing to study mRNA translation dynamics (135). While transcriptomics identified YAP and TAZ as mechanosensitive regulators of gene expression, it is rare that mechanobiologists search for transcription factors in their RNA sequencing datasets. It will be interesting to see if additional mechanosensitive transcription factors will be identified.

Chapter 2:
Activation of ROCK and MLCK tunes regional stress fiber formation and mechanics via preferential myosin light chain phosphorylation.

Elena Kassianidou[1,2], Jasmine H. Hughes[1,2] and Sanjay Kumar[1,2,3]*

[1] Department of Bioengineering, University of California, Berkeley
[2] UC Berkeley – UCSF Graduate Program in Bioengineering
[3] Department of Chemical and Biomolecular Engineering, University of California, Berkeley

ABSTRACT

The assembly and mechanics of actomyosin stress fibers (SFs) depend on regulatory light chain (RLC) phosphorylation, which is driven by Myosin Light Chain Kinase (MLCK) and Rho-Associated Kinase (ROCK). While previous work suggests that MLCK and ROCK regulate distinct pools of cellular SFs, it remains unclear how these kinases differ in their regulation of RLC phosphorylation or how phosphorylation influences individual SF mechanics. Here, we combine genetic approaches with biophysical tools to explore relationships between kinase activity, RLC phosphorylation, SF localization, and SF mechanics. We show that graded MLCK overexpression increases RLC mono-phosphorylation (p-RLC) in a graded manner and that this p-RLC localizes to peripheral SFs. Conversely, graded ROCK overexpression preferentially increases RLC di-phosphorylation (pp-RLC), with pp-RLC localizing to central SFs. Interrogation of single SFs with subcellular laser ablation reveals that MLCK and ROCK quantitatively regulate the viscoelastic properties of peripheral and central SFs, respectively. The effects of MLCK and ROCK on single-SF mechanics may be correspondingly phenocopied by overexpression of mono- and di-phosphomimetic RLC mutants. Our results point to a model in which MLCK and ROCK regulate peripheral and central SF viscoelastic properties through mono- and di-phosphorylation of RLC, offering new quantitative connections between kinase activity, RLC phosphorylation and SF viscoelasticity.

Parts of this chapter have previously been published as “Activation of ROCK and MLCK tunes regional stress fiber formation and mechanics via preferential myosin light chain phosphorylation” in *Molecular Biology of the Cell* (2017, 28:3832-3842) and are reprinted here with permission.

Introduction

A single mammalian cell can exert tensile forces on its surroundings, which can regulate cell shape, motility, and in the case of stem cells, differentiation (136, 87, 137). At the multicellular level, such forces contribute significantly to collective cell migration, tissue morphogenesis during development and wound healing (138–140). Actomyosin stress fibers (SFs) are partly responsible for generating and transmitting these forces to the extracellular matrix (ECM) through direct attachment to focal adhesions as well as through interactions with other cytoskeletal structures (141–143, 115, 144). SFs are comprised of F-actin, structural proteins such as α-actinin, and the force-generating motor protein non-muscle myosin II (NMMII).

NMMII is a hexamer consisting of two essential light chains (ELCs), two regulatory light chains (RLCs) and two heavy chains (145, 146). Each heavy chain contains a globular head domain, which directly engages F-actin and hydrolyzes ATP. This ATP hydrolysis powers the contractile sliding of thick myosin filaments against actin filaments, creating tension within the SF (147). Myosin motor activity and filament formation are strongly regulated by phosphorylation of RLC at Ser19 and Thr18, which allows NMMII to uncoil and assemble into linear thick filaments (145). Mono-phosphorylation (p-RLC) at Ser19 alters the conformation of the NMMII head domains to permit ATPase activity (148) and di-phosphorylation (pp-RLC) of Thr18 and Ser19 further enhances ATPase activity (149–151). Each RLC phosphospecies appears to play different roles in governing SF assembly and tension generation, even though both can coexist within a single SF. For example, while p-RLC has been reported to contribute to SF assembly and to distribute along the entire SF length, pp-RLC preferentially localizes to the most contractile regions of the SF interior as observed during time-lapse imaging (152). While these and other observations hint that p-RLC and pp-RLC contribute differently to SF tensile functions, a causal relationship has not been established.

RLC can be phosphorylated by two orthogonal kinases: the Ca^{2+}/Calmodulin-dependent Myosin Light Chain Kinase (MLCK) and the RhoA effector Rho-Associated Kinase (ROCK). MLCK is encoded by one gene and exists in two forms; long MLCK (~211kDa) and short MLCK (~150kDa) which lacks the N-terminal extension thought to be associated with actin organization and localization differences (153). Both forms directly phosphorylate RLC whereas ROCK promotes RLC phosphorylation either by direct phosphorylation of RLC or by phosphorylating and inactivating RLC phosphatase. Precisely how these kinases differentially contribute to RLC phosphorylation remains unclear, with the few studies focused on this question producing differing results depending on the cellular system and method of perturbation. For example, pharmacologic ROCK inhibition has been reported to reduce pp-RLC but not p-RLC levels in epithelial cells and thrombin activated porcine aortic endothelial cells, whereas pharmacologic MLCK inhibition (via ML-9 or Ca^{2+} depletion) has been observed to affect neither phosphorylation state significantly (152, 154). In contrast, RLC mono-phosphorylation in human platelets is Ca^{2+} dependent, implying activation by MLCK (155). In reconstituted systems, however, MLCK has been reported to produce both p-RLC and pp-RLC (149, 156, 157). Complicating matters further, there are two mammalian isoforms of ROCK (ROCK1 and ROCK2), and recent isoform specific knockdown strategies have shown that ROCK1 induces pp-RLC and regulates actin microfilament bundle formation in fibroblasts whereas ROCK2 preferentially regulates RLC mono-phosphorylation, adhesion maturation and cortical contractility (158–160).

In addition to differences in phosphorylation state, MLCK and ROCK appear to act upon different subcellular pools of SFs, with MLCK preferentially contributing to the assembly of SFs at the periphery of the cell and ROCK preferentially contributing to the assembly of SFs at the cell center (161, 89, 162). Subcellular laser ablation (SLA) measurements reveal corresponding differences in the SF viscoelastic properties of these peripheral and central SFs, with peripheral SFs releasing more elastic energy than central SFs when photo-severed (89). The spatial distribution of p-RLC and pp-RLC appears to be much more nuanced, as both species are observed within both peripheral and central SFs. Perhaps for this reason, it has remained unclear how p-RLC and pp-RLC differentially contribute to the mechanical functions of each SF subpopulation (163–165). Overall, these observations raise the question of whether ROCK and MLCK preferentially control central and peripheral SF formation and mechanical properties by preferential phosphorylation of RLC.

In this study, we investigate mechanistic connections between MLCK and ROCK activity, RLC phosphorylation state, and SF viscoelastic properties using a combination of cell biological and single-cell biophysical approaches. We find that both ROCK1 and ROCK2 regulate central SF retraction kinetics via increased di-phosphorylation of RLC, whereas MLCK regulates peripheral SF retraction kinetics via increased mono-phosphorylation of RLC. An important innovation in our approach is the use of inducibly graded expression of ROCK and MLCK, which enables us to construct quantitative relationships between RLC phosphorylation and SF viscoelastic properties.

Results

To investigate functional contributions of MLCK and ROCK to RLC phosphorylation and SF function, we stably overexpressed constitutively active (CA) mutants of ROCK and MLCK under a doxycycline-inducible promoter in two cell lines, U2OS human osteosarcoma and U373MG human glioblastoma cells (Figure 2.1A) (166, 167). The mutants p160ROCK Δ3 (human CA-ROCK1) and ROCK CAT (bovine CA-ROCK2) lack the RhoA binding domain, thereby unleashing kinase activity in the absence of RhoA-GTP binding, whereas rabbit smooth muscle short MLCK ED785-786KK (CA-MLCK) lacks a functional autoinhibition domain (168–170). Importantly, doxycycline induction allows titration of gene expression over a continuous range, which in turn enables elucidation of quantitative relationships between expression and mechanobiological phenotype in a manner not possible with pharmacological inhibition or transient plasmid overexpression (167, 19, 171, 172). Understanding this dose-response relationship is an important experimental design consideration given that the relationship between myosin activation and mechanobiological phenotype is often highly nonlinear (167, 76).

We first confirmed that we can indeed express each kinase in a gradient by quantifying CA-MLCK (Figure 2.1B) and CA-ROCK2 (Figure 2.1C) levels as a function of doxycycline concentration for both cell lines. As expected, CA-MLCK and CA-ROCK2 were undetectable in the absence of doxycycline for both cell lines. The expression of each kinase increased in a statistically significant fashion with increasing doxycycline concentration (quantification shown in Fig. 1B and 1C; Spearman correlation coefficients $\rho_{U2OS,\ CA\text{-}MLCK} = 0.87$, $\rho_{U373,\ CA\text{-}MLCK} = 0.94$, $\rho_{U2OS,\ CA\text{-}ROCK2} = 0.82$, $\rho_{U373,\ CA\text{-}ROCK2} = 0.83$). We also successfully produced similarly graded expression of CA-ROCK1 as shown by increasing intensity of the Myc tag with doxycycline (Figure 2.2). Moreover, we compared the expression of the CA constructs relative to the levels of the endogenous kinases. We observed that the expression levels of CA-ROCK2 relative to endogenous were 0.85-fold for

U2OS and 1.66-fold at the highest doxycycline concentration for U373MG cells respectively (Figure 2.3). The expression levels of CA-MLCK relative to endogenous MLCK were higher for both cell lines ranging around 1-fold for U2OS and 4.8-fold for U373MG cells at the highest doxycycline concentrations (Figure 2.3, U2OS CA-MLCK was normalized to 130kDa MLCK whereas U373MG CA-MLCK was normalized to 211kDa MLCK). Overall, we observe that our system allows us to produce graded but modest overexpression of ROCK2 and MLCK in both cell lines over a range that enables us to study the relationship between kinase expression and mechanobiological phenotypes.

As described earlier, our and others' pharmacological studies have demonstrated that ROCK and MLCK regulate the formation of different subsets of SFs, with ROCK inhibition disrupting central SFs and MLCK inhibition disrupting peripheral SFs (89, 162). We therefore hypothesized that graded increases in the expression of each kinase would produce graded changes in each corresponding SF subpopulation, which may in turn drive alterations in cell morphology. The two cell lines chosen exhibit different central SF architectures: U2OS cells feature prominent ventral SFs (Figures 2.4A and 2.4C at 0 ng/ml doxycycline), which localize to the cell rear and terminate in FAs, whereas U373MG cells exhibit more transverse arcs, which lie parallel to the leading edge and anchor internally within the SF network (Figures 2.4B and 2.4D at 0 ng/ml doxycycline). With increasing doxycycline concentration, both U2OS CA-MLCK and U373MG CA-MLCK cells exhibited brighter and slightly thicker peripheral SFs (Figure 2.4A and B, highlighted insets and arrow heads point to peripheral SFs). Additionally, expression of CA-MLCK in U373MG cells resulted in the formation of smaller actin fibers close to the peripheral SFs (Figure 2.4B, 200 ng/ml inset). In contrast, CA-ROCK2 expression increased the density of central SFs for both cell lines (Figures 2.4C and 2.4D). Specifically, U2OS CA-ROCK2 cells exhibited thicker central SFs with increasing doxycycline concentrations compared to the 0 ng/ml doxycycline condition (Figure 2C, highlighted insets and arrow heads pointing to central ventral SFs). At higher concentrations, central SFs sometimes formed meshlike structures with indistinguishable SFs. Similarly, expression of CA-ROCK2 in U373MG cells led to the formation of ventral SFs within the cell center as compared to cells cultured the 0 ng/ml doxycycline condition, which exhibited a more poorly defined SF network (Figure 2.4D, highlighted inset and arrow heads point to central ventral SFs). At higher doxycycline concentrations, U373MG CA-ROCK2 cells also exhibited brighter and thicker central SFs (Figure 2.4D, 120 ng/ml doxycycline inset). We also saw similar effects on central SF architecture with expression of CA-ROCK1 (Figure 2.5). Thus, both cell lines exhibit similar ROCK-dependent enhancement of central SFs and MLCK-dependent enhancement of peripheral SFs.

To determine whether the CA constructs exhibit preferential localization, we performed immunostaining in both U2OS and U373MG CA-MLCK and CA-ROCK2 cells cultured in the presence and absence of doxycycline. Previous work has shown that MLCK has an actin binding domain in its N-terminus (173). Long MLCK preferentially localizes to SFs whereas short MLCK exhibits a more cytoplasmic localization (153). In both U2OS and U373MG cells, endogenous MLCK exhibits diffuse localization (Figure 2.6). Addition of doxycycline increases the fluorescence intensity due to expression of short CA-MLCK but does not change the localization patterns. Endogenous ROCK2 and CA-ROCK2 also exhibit diffuse localization for both U2OS and U373MG cell lines. Similar localization patterns were also observed with overexpression of

CA-ROCK1 in U2OS cells. Overall, the kinases do not seem to differ in their localization despite the distinct changes in SF architecture observed with expression of each kinase.

To quantify how changes in the expression of each kinase translate into levels of RLC mono- and di-phosphorylation, we performed Western blots using phospho-specific antibodies. First, we explored whether any changes in RLC phosphorylation were observed in the presence and absence of doxycycline induction of MLCK and ROCK (Figure 2.7). Induction of CA-MLCK produced a statistically significant increase in p-RLC but not in pp-RLC for both cell lines ($p_{U2OS,\ p\text{-}RLC\ (rabbit)} = 0.035$, $p_{U2OS,\ pp\text{-}RLC\ (rabbit)} = 0.75$, $p_{U373,\ p\text{-}RLC\ (mouse)} = 0.0092$, $p_{U373,\ pp\text{-}RLC\ (rabbit)} = 0.061$; Kruskal Wallis followed by Dunn's non-parametric test for U2OS and Student's t-test for U373MG). In contrast, induction of CA-ROCK2 increased pp-RLC but not p-RLC in both cell lines ($p_{U2OS,\ p\text{-}RLC\ (rabbit)} = 0.10$, $p_{U2OS,\ pp\text{-}RLC\ (rabbit)} = 0.0006$, $p_{U373,\ p\text{-}RLC\ (mouse)} = 0.072$, $p_{U373,\ pp\text{-}RLC\ (rabbit)} = 0.019$; Student's t-test of U373MG and ANOVA followed by Student's t-test for U2OS). We next asked how graded variations in the activity of each kinase altered phosphorylation states (Figure 2.8). In both cell lines, graded induction of CA-MLCK expression produced a monotonic increase in p-RLC (Figure 2.8A, empty grey circles; Spearman correlation coefficients $\rho_{U2OS,\ p\text{-}RLC\ (mouse)} = 0.65$, $\rho_{U373,\ p\text{-}RLC\ (mouse)} = 0.55$). Interestingly, CA-MLCK in both U2OS and U373MG cells slightly increased pp-RLC in a graded manner as well, consistent with a sequential phosphorylation mechanism (Figure 2.8A, solid triangles; Spearman correlation coefficients $\rho_{U2OS,\ pp\text{-}RLC\ (rabbit)} = 0.30$, $\rho_{U373,\ pp\text{-}RLC\ (rabbit)} = 0.50$). In both cell lines, increasing the expression of CA-ROCK2 increased pp-RLC Figure 2.8B, solid triangles circles; Spearman correlation coefficients $\rho_{U373,\ pp\text{-}RLC\ (rabbit)} = 0.38$, $\rho_{U2OS,\ pp\text{-}RLC\ (rabbit)} = 0.61$), while no graded change was observed in p-RLC in both U2OS and U373MG cells (Figure 2.8B, empty grey circles; Spearman correlation coefficients $\rho_{U2OS,\ p\text{-}RLC\ (mouse)} = -0.17$, $\rho_{U373,\ p\text{-}RLC} = -0.28$). We also observed the same trends with CA-ROCK1 expression in U2OS cells (Figure 2.7), suggesting that both ROCK1 and ROCK2 isoforms preferentially produce pp-RLC.

Given the strong influence of ROCK1/2 on central SFs and pp-RLC levels, and that of MLCK on peripheral SFs and p-RLC levels, we wondered whether the observed kinase-dependent RLC phospho-species localized to the respective kinase-dependent SF subpopulations. RLC-phospho-specific immunostaining of CA-MLCK (Figure 2.9A) and CA-ROCK2 cells (Figure 2.9B) indeed revealed an MLCK-dependent increase in p-RLC in the cell periphery (Figure 2.9A, highlighted inset) and a ROCK-dependent increase in pp-RLC in the cell center (Figure 2.9B, highlighted inset). Quantification of this localization revealed a statistical increase in p-MLC in both peripheral (black) and central SFs (grey) for both U2OS and U373MG CA-MLCK cells for both U2OS and U373MG cells (Figure 2.9C, top row). The details of this relationship varied with cell line. U2OS cells exhibited a much greater enhancement of p-RLC in peripheral SFs than central SFs (U2OS: 2.6-fold for peripheral versus 1.6-fold for central; U373MG: 2.0-fold for peripheral versus 1.92) as well as a slight increase in the amount of pp-RLC in peripheral SFs (U2OS: 1.3-fold increase; U373MG: 1.1-fold increase) (Figure 2.9C, bottom row). Induction of CA-ROCK2 produced an increase in pp-RLC in central SFs for both cell lines (U2OS: 1.94-fold; U373MG: 1.2-fold) (Figure 2.9D, bottom row). For U2OS cells, a small increase in the amount of p-RLC was also observed in central SFs (U2OS: 1.28-fold increase) (Figure 2.9D, top row). Taken together with our earlier SF morphometric observations (Figure 2.4) and Western blots (Figure 2.8), these results indicate that ROCK promotes formation of central SFs and an associated central localization of pp-RLC,

whereas MLCK promotes formation of peripheral SFs and an associated peripheral localization of p-RLC.

To determine if the localized changes in RLC phosphorylation caused by each kinase produced changes in the mechanical properties of the associated SFs, we performed SLA to sever individual central and peripheral SFs of U2OS CA-ROCK2 and U2OS CA-MLCK cells cultured in the presence and absence of doxycycline. As in our previous studies, we photo-severed single SFs and fit the time-dependent retraction of the two SF ends to the Kelvin-Voigt model of viscoelasticity. This model is described by two parameters: a viscoelastic time constant (τ), reflecting the SF's effective viscosity to elasticity ratio, and a plateau retraction distance (L_o), reflecting the elastic energy dissipated by half of the severed SF (Figure 2.10A) (115, 174, 175). Whereas L_o and τ for peripheral SFs were insensitive to CA-ROCK2 induction (Figure 2.10B), both parameters statistically increased with CA-MLCK induction (Figure 2.10B). For central SFs, both L_o and τ were influenced by CA-ROCK2 induction but not by CA-MLCK induction (Figure 2.10C). Notably, both CA-ROCK1 and CA-ROCK2 influenced SF mechanics in a similar manner (Figure 2.11, Figures 2.10B-C). Thus, ROCK and MLCK preferentially regulate the viscoelastic properties of central and peripheral SFs, respectively.

As noted earlier, an important advantage of graded, inducible expression systems is the ability to construct quantitative relationships between effector level and phenotype. Given our ability to associate RLC phosphorylation levels at a specific doxycycline concentration (Figure 2.8) and our ability to elucidate SF viscoelastic properties at these same doxycycline concentrations, we were uniquely well positioned to explore correlations between phospho-RLC levels and SF mechanics. To answer this question, we performed SLA on U2OS cells expressing either CA-MLCK (Figure 2.12A) or CA-ROCK2 (Figure 2.12B) cultured in varying doxycycline concentrations. We observed statistical differences in the dissipated elastic energy (L_o) and viscoelastic time constant (τ) for peripheral SFs of CA-MLCK (grey, Figure 2.12A) and in both L_o and τ for central SFs of CA-ROCK2 cells (orange, Figure 2.12B, Kruskal Wallis test followed by Dunn's nonparametric test). We also observed that graded expression of CA-MLCK, which increases p-RLC (x-axis is from Figure 2.8A), preferentially increased both the elastic energy dissipated by the fiber (L_o) and the viscoelastic time constant (τ) of peripheral SFs (dark grey circles) in a graded manner but did not alter the properties of central SFs (orange circles) (Figure 2.12C) (Spearman correlation for L_o: $\rho_{peripheral} = 0.31$, $\rho_{central} = 0.018$; Spearman correlation for τ: $\rho_{peripheral} = 0.23$, $\rho_{central} = 0.028$). The increase in L_o and τ of peripheral SFs with increased p-RLC follows a nonlinear relationship with the properties not changing significantly until p-RLC reaches at least a 2.5-fold increase (Figure 2.12C). Graded expression of CA-ROCK2, which led to an increase in the amount of pp-RLC (x-axis is from Figure 2.8B), preferentially increased the elastic energy dissipated by the fiber after SLA (L_o) and the viscoelastic time constant (τ) of central SFs (orange circles) (Figure 2.12D) (Spearman correlation for L_o: $\rho_{peripheral} = 0.026$, $\rho_{central} = 0.56$; Spearman correlation for τ: $\rho_{peripheral} = 0.077$, $\rho_{central} = 0.29$). L_o appeared to increase linearly with pp-RLC, and at approximately a 3.5-fold increase in pp-RLC above basal levels, the viscoelastic character of central SFs matched that of peripheral SFs. The increase in τ followed a decaying nonlinear curve, eventually reaching a plateau at approximately a 3.5-fold increase in pp-RLC (Figure 2.12D). These results suggest that SF mechanical properties are indeed tunable based on the type and amount of phosphorylated RLC present.

Our results indicate that ROCK and MLCK phosphorylate RLC in a preferential manner; MLCK primarily mono-phosphorylates RLC (Ser19) whereas ROCK 1 and ROCK 2 preferentially di-phosphorylate it (Thr18 and Ser19) (Figure 2.8 and Figure 2.3). We also show that these changes in phosphorylation have specific localizations – MLCK-induced p-RLC localizes primarily in the periphery of the cell whereas ROCK-induced pp-RLC localizes in the center (Figure 2.9). Finally, we show that SF mechanical properties are also regulated preferentially via the kinases – ROCK controls central SF retraction kinetics, whereas MLCK controls peripheral retraction kinetics (Figures 2.10 and 2.12). However, these results leave open the question of whether ROCK and MLCK-induced changes in RLC phosphorylation and SF properties are causally linked as opposed to unrelated epiphenomena. To provide a direct link between the kinases, MLC phosphorylation states and SF mechanics, we transduced U2OS RFP-LifeAct cells with mono-phosphomimetic RLC, where Ser19 was mutated to Asp (RLC-AD), or with di-phosphomimetic RLC, where both Thr18/Ser19 were mutated to Asp (RLC-DD) (165). We first noted that U2OS phosphomimetic-expressing cells phenocopy the SF architecture of U2OS CA-MLCK and CA-ROCK2 cells. Specifically, U2OS GFP RLC-AD cells show an elongated phenotype with bright peripheral SFs whereas U2OS GFP RLC-DD cells exhibit bright central SFs (Figures 2.13A and B). We then wished to determine whether these phosphomimetic species localize in similar patterns as the ones observed earlier (Figure 2.8). GFP-RLC AD localizes strongly on peripheral SFs (Figures 2.13A and B, white arrows) whereas GFP-RLC DD localizes primarily on central SFs (yellow arrows). We quantified the GFP-signal of RLC-AD and RLC-DD on both peripheral and central SFs and calculated a localization ratio in which > 1 indicates preferential localization to peripheral SFs whereas < 1 indicates preferential localization to central SFs. Analogous to the immunostaining studies (Figure 2.8), we observed that GFP RLC-AD localizes preferentially to peripheral SFs whereas GFP RLC-DD localizes to central SFs (Figure 2.13C). Finally, we performed SLA on peripheral (Figure 2.13D) and central SFs (Figure 2.13E) of RLC-AD and RLC-DD cells. Overexpression of RLC-AD affected only the elastic energy (L_o) dissipated by peripheral SFs ($p = 0.029$) and not central SFs ($p = 0.63$), phenocopying the results seen with CA-MLCK expression (Figure 2.13D). In turn, overexpression of RLC-DD affected only the elastic energy (L_o) dissipated by central SFs ($p < 0.0001$) and not peripheral SFs ($p = 0.72$), phenocopying the results obtained via CA-ROCK2 expression (Figure 2.13E). These results suggest that the changes in the viscoelastic retraction parameters observed from the increased expression of kinases are directly due to the changes in RLC phosphorylation.

Discussion

ROCK and MLCK are broadly understood to govern RLC phosphorylation, thereby regulating the assembly and contraction of SFs. While there is much evidence that ROCK and MLCK respectively regulate the assembly and contractility of central and peripheral SFs (161, 89, 162), it has remained unclear how each kinase controls RLC phosphorylation state or how these states influence SF viscoelastic properties. By combining cell and molecular biological approaches with mechanical measurements of single SFs in living cells, we have provided support for a model in which MLCK and ROCK distinctly regulate peripheral and central SF mechanics via differential phosphorylation of RLC. Specifically, MLCK stimulates production of p-RLC, which localizes to and controls peripheral SF viscoelasticity. In contrast, both ROCK isoforms stimulate production of pp-RLC, which localizes to and controls central SF viscoelasticity (Figure 2.14). The mechanical effects of each kinase can be recapitulated with overexpression of a corresponding mono- or di-phosphomimetic RLC, strongly supporting a causal link between kinase activity, RLC phosphorylation state, and SF viscoelastic properties.

As noted earlier, previous efforts to dissect contributions of ROCK and MLCK to RLC phosphorylation have produced results that vary with the method used to study and perturb each kinase. In reconstituted preparations, MLCK has been observed to produce both p-RLC and pp-RLC; however, pp-RLC requires comparatively high MLCK concentrations (0.1-1 μM), leaving open the question of which phosphospecies is favored under more physiological conditions (Takeo Itoh et al. 1989; Ikebe & Hartshorne 1985; Ikebe et al. 1986). While pharmacological inhibition in cell culture of either ROCK or MLCK has been observed to reduce di-phosphorylation of RLC (152), the interpretation of these results is complicated by the fact that MLCK and ROCK inhibitors can produce SF and FA disassembly at sufficiently high dose, create off-target effects, and lack isoform selectivity. Moreover, studies of ROCK/MLCK effects on RLC phosphorylation have not been systematically coupled to measurements of contractile function. Our study begins to close this loop by combining controlled expression of each kinase with measurements of viscoelastic properties of individual SFs. We show that overexpression of CA-ROCK1 and CA-ROCK2 preferentially increase the viscoelasticity parameters of central SFs (Figures 2.5, 2.10, 2.12). Our results also reveal that overexpression of a short CA-MLCK that does not localize to SFs preferentially increases the stored elastic energy (as reflected by L_o) and viscoelastic time constant (τ) of peripheral SFs. It should be informative to apply long MLCK mutants of varying actin-binding abilities and determine how the viscoelastic properties of peripheral SFs are altered by direct MLCK binding.

While SF tension generation has been shown to depend on RLC phosphorylation, it has remained unclear whether graded changes in myosin activation produce graded changes in SF tension generation, or whether there are instead activation thresholds at which SF tension changes in a concerted fashion (177). We find that graded increases in the expression of either CA-MLCK or CA-ROCK2 produce monotonic increases in both RLC phosphorylation and SF elastic energy. To our knowledge, this represents the first indication that SF viscoelastic properties can be tuned over a continuous range based on kinase activity. Furthermore, we were able to quantitatively map the relationship between whole-cell RLC phosphorylation levels and individual SF properties. Surprisingly, the viscoelastic properties of peripheral SFs depend much more nonlinearly on p-RLC levels than central SF mechanics depend on pp-RLC levels, indicating that central SFs may

be more sensitive to small perturbations above basal RLC phosphorylation levels than peripheral SFs. Moreover, these correlations juxtapose properties of single SFs against whole-cell measurements of p-RLC and pp-RLC, which is a consequence of our inability to perform SLA in live cells while simultaneously performing antibody-based detection of phospho-RLC levels. It should be noted that our measured fold changes in RLC phosphorylation cannot be used to infer stochiometric ratios of p-RLC and pp-RLC within a given cell or SF. It would be valuable to revisit these MLCK and ROCK manipulations, measure the effects on p-RLC/pp-RLC ratios (e.g. with mass spectrometry or urea/glycerol gel electrophoresis), and ask if these ratios are predictive of SF viscoelastic properties. Additionally, fiber-by-fiber correlations of phospho-RLC state and viscoelastic properties may be facilitated in the future by geometric standardization of SFs (115) or through the use of live-cell kinase probes. Finally, further work is required to discern the relationship of each kinase to NMMIIA and IIB heavy isoform and their respective localization to central and peripheral SFs (146, 174, 178).

Within the region of ROCK isoform activities probed, we did not observe strong differences between ROCK1 and ROCK2 in regulation of RLC phosphorylation, SF formation or SF viscoelastic properties. Recent ROCK isoform-specific knockdown studies have revealed that ROCK1 preferentially regulates pp-RLC whereas ROCK2 preferentially regulates p-RLC in CHO.K1 and REF52 cells and that the two isoforms play differential roles in migration (158, 179). Moreover, ROCK1 knockdown in MCF-7 cells specifically reduced p-RLC localization to adherens junctions suggesting that ROCK1 preferentially regulates contractility in adherens junctions (180). On the other hand, ROCK1 and ROCK2 have also been observed to serve redundant functions in other settings; ROCK1- and ROCK2-null fibroblasts showed similarly small reductions in RLC di-phosphorylation and cell contractility relative to wild type controls with statistically significant effects seen only when both ROCK isoforms were removed (181). Additional differences may arise from the method of ROCK isoform perturbation (i.e., overexpression versus knockdown). These distinct regimes of kinase activity may produce divergent effects on RLC phosphorylation state due to the complex and potentially non-linear relationships between these RLC activators, ROCK-inhibited RLC phosphatase and RLC phosphorylation (177, 182). It is important to acknowledge that previous work has suggested that phosphomimetic RLCs (TE or EE) may not mimic endogenous phosphorylated RLC in *in vitro* assays and in *Drosophila*. We observed that phosphomimetic RLCs used in this study (AD and DD) emulated the localization patterns of p-RLC and pp-RLC, phenocopied the SF architecture changes triggered by MLCK-induced p-RLC and ROCK-induced pp-RLC and congruently alrered SF viscoelastic changes (151, 183, 184). Nonetheless, additional characterization of these and related RLC mutants would help assess the degree to which they capture the effects of phosphorylation.

Overall, our work highlights a potential mechanism for cells to spatially and temporally regulate the distribution of contractile forces via preferential phosphorylation from different kinases. Increased ATPase activity of pp-RLC induced primarily by ROCK isoforms may need to be localized in central regions of the cell to modulate cell migration and shape maintenance whereas MLCK-induced p-RLC leads to less sustained force in the periphery. The distinct contributions of each phosphospecies to SF viscoelasticity may involve multiple protein-protein interactions, given that highly reductionist myosin sliding assays do not detect differences in velocities between p-RLC and pp-RLC (149). Nevertheless, with the many recent efforts to develop multiscale

mechanochemical models of SF function (185–189), data such as ours may offer valuable new inputs for these models and facilitate incorporation of distinct subcellular pools of SFs.

Materials and Methods

Cell lines and reagents

Myc tagged human p160ROCK Δ3 (kindly provided by Dr. S. Narumiya, Kyoto University, Japan), Flag-tagged rabbit smooth muscle MLCK ED785-786KK (kindly provided by Dr. P. J. Gallagher, Indiana University, USA) and bovine ROCK CAT (kindly provided by Dr. K. Kaibuchi, Nagoya University, Japan) were subcloned into the lentiviral vector pSLIK containing the TRE tightdoxycycline-inducible promoter (Addgene # 84647 for CA-MLCK and #84649 for CA-ROCK2) (166, 167). p160ROCK Δ3 is a constitutively active (CA) mutant of the ROCK1 isoform whereas ROCK CAT is a CA mutant of the ROCK2 isoform. Our sequencing reveals that this CA-MLCK bears 98% identity to rabbit smooth muscle MLCK (~150kDa) but harbors a mutation within the autoinhibitory site (ED773-774KK of construct, which aligns with ED785-786KK in wild type MLCK). This mutation has previously been shown to confer CA function in bovine smooth muscle MLCK through disruption of auto-inhibition (169, 190). Empty pSLIK vectors were also used to establish control cell lines. Viral particles for each pSLIK plasmid and for the pFUG-RFP-LifeAct vector were packaged in 293T cells. U2OS osteosarcoma cells (ATCC HBT-96) were transfected with pFUG-RFP-LifeAct and sorted on a DAKO-Cytomation MoFlo High Speed Sorter based on RFP fluorescence (191). U2OS RFP LifeAct cells were further stably transduced with the pSLIK vectors at an MOI of 0.5 IU/cell. Cells were further sorted based on RFP and Venus fluorescence. U373MG glioblastoma cells (ATCC HTB-17, also known as U-373 MG) were transfected with the pSLIK plasmids at an MOI of 0.5 IU/cell, and cells receiving the construct were selected based on Venus fluorescence. U373MG cells containing the pSLIK plasmid were then transfected with pFUG-RFP-LifeAct at an MOI of 1.5 IU/cell and cells receiving the LifeAct vector were selected using 0.6 μg/mL puromycin. ATCC U373MG cells have been established to be derived from a common progenitor with U251 cells and SNB 19 cells , although the lines have diverged and exhibit some phenotypic and karyotypic differences (192). Both cell lines were confirmed by short tandem repeat profiling and mycoplasma testing was carried out every four months.

Plasmids containing phosphomimetic myosin light chains (pEGFP RLC-DD, pEGFP RLC-AD) were kindly provided by Dr. A. R. Horwitz (University of Virginia, USA) (165). The RLC-GFP constructs were digested from the plasmid backbone using EcoRI and XhoI and ligated into the lentiviral vector pLVX-AcGFP-N1 (Clonetech). Successful ligation was verified via sequencing. Viral particles for each plasmid were packaged in 293T cells. U2OS RFP-LifeAct cells were stably transduced with the viral particles at an MOI of 0.5 IU/cel. Cells were then sorted based on RFP and GFP fluorescence.

U2OS cells were cultured in DMEM supplemented with 10% fetal bovine serum (JR scientific), 1% penicillin/strep (Thermo Fischer Scientific) and 1% Non-Essential Amino Acids (Life Technologies). U373MG cells were cultured in DMEM supplemented with 10% calf serum (JR scientific), 1% penicillin/strep, 1% Non-essential amino acids and 1% sodium pyruvate (Thermo Fischer Scientific). Doxycycline (Fisher Bioreagents) was added at the required concentration two days prior to all experiments to activate the constitutively active constructs.

Western blots

As described previously, cells were lysed in RIPA buffer with phosphatase and protease inhibitors (EMD Millipore, Billerica, MA) (115, 166). Protein content was measured by BCA and used to normalize samples before loading to the lowest concentration. Lysates were boiled, run on 4-12% Bis-Tris gels and transferred onto a PVDF membrane. The following primary antibodies were used: anti-phosphorylated myosin light chain 2 (Thr18/Ser19) (Cell Signaling Technology), anti-phosphorylated myosin light chain 2 (Ser19) produced in rabbit or in mouse (both obtained from Cell Signaling Technology), anti-GAPDH (Sigma-Aldrich, St. Louis, MO), mouse anti-MLCK (Sigma-Aldrich, St. Louis, MO) and rabbit anti-MLCK (abcam), anti-ROCK 2 (Sigma-Aldrich, St. Louis, MO), anti-Myc tag (Cell Signaling Technology), anti-ROCK1 (Cell Signaling Technology). The following secondaries were used: IRDye 800 Goat anti-mouse IgG, IRDye 700 Goat anti-rabbit IgG (Licor) and HRP-conjugated anti-mouse (Life Technologies). All bands except Myc-tag for CA-ROCK1 visualization (Figure 2.2) were visualized using an Odyssey system and were quantified with the built-in gel analyzer tool in ImageJ (NIH). Myc-tag bands were visualized using ECL reagent.

Immunofluorescence staining

Cells were seeded on glass coverslips coated with 25 μg/ml of fibronectin (EMD Millipore Corporation). After doxycycline incubation, cells were fixed with 4% paraformaldehyde for 10 minutes at room temperature. After PBS washes, cells were permeabilized in 0.5% Triton-X for 15 minutes, and blocked in 5% goat serum (GS) (Thermo Fisher Scientific) for at least 1 hour. U2OS cells were incubated in 1% GS and primary antibody for 2 hours at room temperature or overnight at 4°C in a humidity chamber. U373MG cells were incubated in 1% GS and primary antibody overnight at 4°C. Following primary incubation, cells were washed in 1% GS (3 x 5 minutes) and then incubated in secondary antibody for 1 hour at room temperature. We used the following antibodies: anti-phosphorylated myosin light chain 2 (Thre18/Ser19) produced in rabbit (Cell Signaling Technology), anti-phosphorylated myosin light chain 2 (Ser19) produced in mouse (Cell Signaling Technology), anti-MLCK (Sigma-Aldrich, St. Louis, MO), anti-ROCK2 (Sigma-Aldrich, St. Louis, MO), anti-ROCK1 (Cell Signaling Technologies), Alexa-fluor 647 anti-mouse, Alexa-fluor 488 anti-rabbit and Alexa-fluor 633 anti-rabbit (Thermo Fisher Scientific). F-actin was stained with 546-phalloidin. U373MG cells were mounted on glass slides using ProLong Gold Antifade Mountant (Thermo Fischer Scientific). Figure 2.9 immunofluorescence images were obtained using a swept-field upright confocal microscope equipped with a 60x water immersion lens (Prairie Technologies) and a Nikon TE2000 microscope equipped with a 60x oil immersion lens. U2OS MLCK, ROCK1 and ROCK2 images were obtained on a Zeiss LSM 510 Meta Confocal microscope equipped with a 63x oil immersion objective whereas U373MG images were obtained using a Nikon TE2000 microscope equipped with a 60x oil immersion lens. For presentation purposes, the contrast and brightness of fluorescence images were optimized using ImageJ (NIH).

Analysis of immunofluorescence images

All analyses were performed using ImageJ (NIH). To quantify the localization of p-RLC and pp-RLC, images were overlaid with phalloidin and background was subtracted. Alignment of images was verified using Template Matching plug-in (193). A line of 0.6 µm thickness was manually drawn over peripheral or central SFs for multiple SFs per cell and a measurement of raw integrated intensity of p-RLC and pp-RLC was recorded across each traced line. The intensities were then normalized to the length of the drawn line and averages of normalized intensities were calculated per cell. To account for experiment-to-experiment variations in fluorescent intensity, values were normalized to the mean value of the appropriate control – i.e., CA-ROCK2 or CA-MLCK cells cultured in 0 ng/ml doxycycline for each specific experiment.

To quantify the localization of GFP RLC-AD and GFP RLC-DD, cells were seeded on 25 µg/ml fibronectin coated coverslips and fixed using 4% paraformaldehyde. Cells were permeabilized and incubated with Alexa 546-tagged phalloidin. Images of SFs and phosphomimetic species were obtained using a 63x oil immersion objective. A line of 0.6 µm was drawn over peripheral and central SFs and the intensity of the GFP signal was recorded. The intensities were then normalized to the length of the drawn line and averages of normalized intensities were calculated per cell. The ratio of peripheral to central SF localization was then determined.

SF photo-disruption

SF SLA experiments were performed on a Zeiss LSM 510 Meta Confocal microscope equipped with a MaiTai Ti:sapphire femtosecond laser (Spectra Physics, Newport Beach, CA) (143, 89, 174). 10,000 cells were seeded on 35 mm glass bottom dishes (MatTek Corporation) coated with 25µg/ml of fibronectin (EMD Millipore Corporation) and incubated in doxycycline for 2 days. Media was changed to Live Cell Imaging Solution (Invitrogen) prior to SLA. For SF photodisruption, the femtosecond laser was used at 770nm resulting in an energy deposition of 1-2 nJ on a single SF (115, 89, 174). All images were acquired with a 40x water-immersion objective (N.A = 0.8).

Data analysis of SF retraction

SF retraction distance was recorded every 1.96 seconds for 49 seconds following SLA occurring after 3 seconds. The SF ends were manually traced using Image J to determine the retraction dynamics. Results were fitted to a Kelvin-Voigt model defined by the following equation:

$$L = D_a + L_o\left(1 - exp\left(\frac{-t}{\tau}\right)\right)$$

where L is defined as half the distance between the two severed SF ends, D_a is the length of SF destroyed by the laser, L_o is the retraction plateau distance and τ is the viscoelastic time constant. Curve fitting to extract parameters L_o and τ was performed using CurveFit (MATLAB) (115, 89, 174).

Statistical analysis

All statistical analyses and graph generation were performed using GraphPad Prism and R. Unless otherwise noted, samples were compared using non-parametric t-tests such as Mann-Whitney. Normality was assessed based on Shapiro-Wilk Normality test. Experiments that used cells seeded and assayed on different days were deemed independent, and at least three independent experiments were performed for each assay.

Acknowledgements

Subcellular laser ablation and confocal imaging were performed at the CRL Molecular Imaging Center supported by NIH 3R01EY015514-01S1. Confocal images were also obtained at the CIRM/QB3 Stem Cell Shared Facility. FACS was performed with the help of H. Nolla in the Flow Cytometry Facility at the University of California, Berkeley. The authors gratefully acknowledge financial support from the following sources: Howard Hughes Medical Institute International Student Research Fellowship and Siebel Scholars Program (E.K.); Natural Sciences and Engineering Research Council (NSERC) of Canada (PGS D 555229) and Siebel Scholars Program (J.H.H.); National Institutes of Health (R21CA174573, R21EB016359, R01GM122375, R01NS074831), National Science Foundation (CMMI 1055965), and W.M. Keck Foundation (S.K.).

Figures & Figure Legends

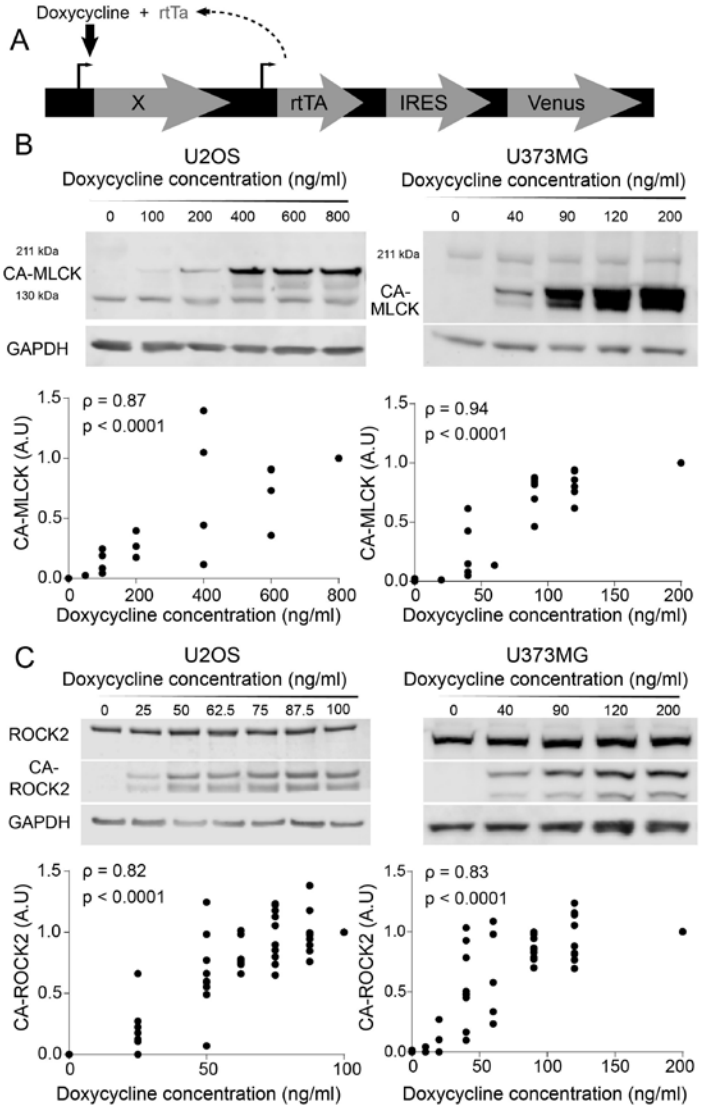

Figure 2.1: Graded control over the expression of a constitutively active form of MLCK (CA-MLCK) and ROCK2 (CA-ROCK2). (A) Schematic of doxycycline inducible lentiviral system. (B) Representative Western blot showing expression levels of endogenous MLCK, CA-MLCK and GAPDH in U2OS (left) and U373MG cells (right) as a function of doxycycline concentration. U2OS cells were probed with rabbit ant-MLCK (Abcam 76092) and U373MG cells were probed with mouse anti-MLCK (Sigma M7905). Expression levels of CA-MLCK were quantified, normalized to GAPDH and the highest doxycycline concentration for each cell line and plotted below the respective Western blots (n = 4 blots for U2OS and n = 6 blots U373MG). (C) Representative Western blot showing expression levels of endogenous ROCK2, CA-ROCK2 and GAPDH in U2OS (left) and U373MG (right) cells in the presence of varying amounts of doxycycline. Expression levels of CA-ROCK2 were quantified, normalized to GAPDH and the highest doxycycline concentration, and plotted below the respective Western blots (n = 10 blots for U2OS and n = 10 blots for U373MG at the maximum doxycycline concentration). Statistical parameters shown represent the Spearman's rank correlation coefficient (ρ) and p-value.

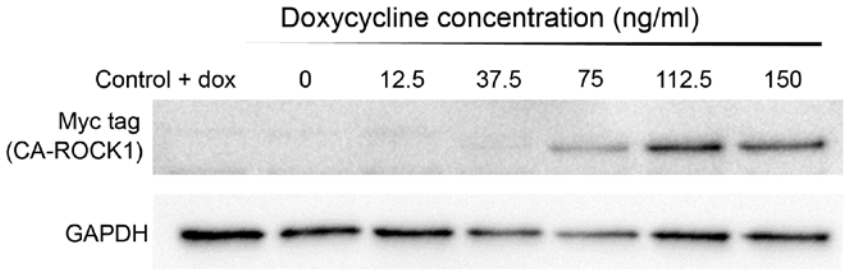

Figure 2.2: Representative Western Blot showing gradient expression of CA-ROCK1 as indicated by Myc-tag in U2OS cells cultured in varying doxycycline concentrations.

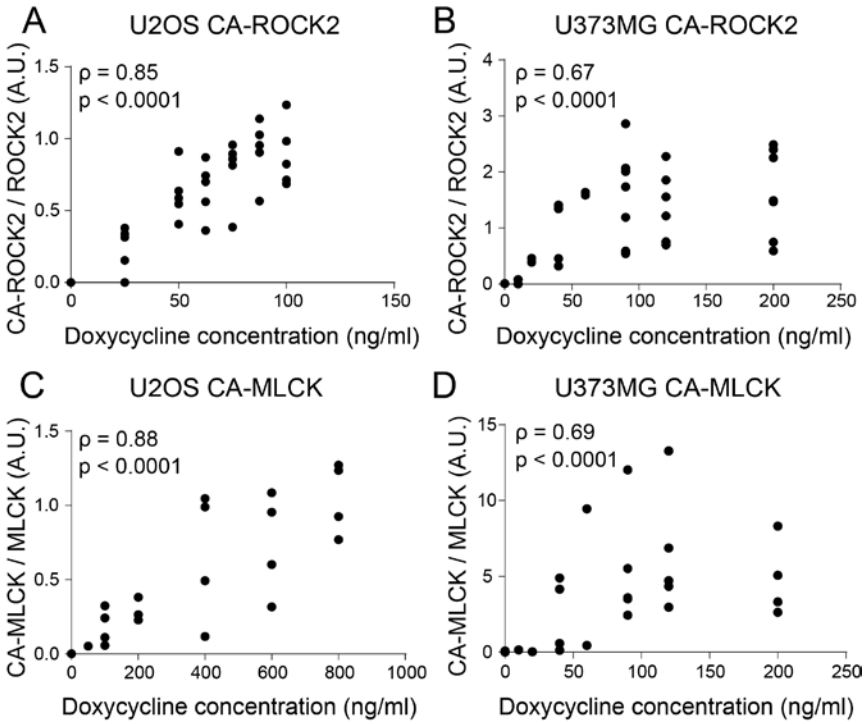

Figure 2.3: Quantification of the ratio of construct to endogenous ROCK2 and MLCK. (A) Ratio of CA-ROCK2 to endogenous ROCK2 in U2OS cells cultured in varying concentrations of doxycycline (n = 9 blots). (B) Ratio of CA-ROCK2 to endogenous ROCK2 in U373MG cells cultured in varying concentrations of doxycycline (n = 7 blots). (C) Ratio of CA-MLCK to 130kDa endogenous MLCK as determined by Abcam rabbit anti-MLCK in U2OS cells cultured in varying concentrations of doxycycline (n = 4 blots (D) Ratio of CA-MLCK to 210kDa endogenous MLCK as determined by Sigma mouse anti-MLCK in U373MG cells cultured in varying amounts of doxycycline (n = 5 blots). Statistical parameters shown represent the Spearman's rank correlation coefficient (ρ) and p-value.

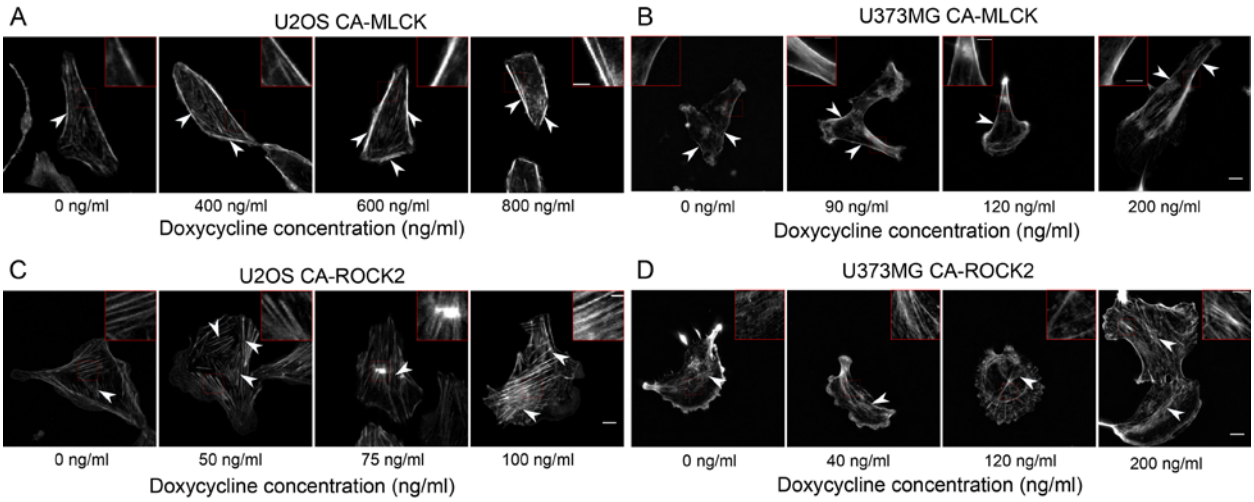

Figure 2.4: Graded expression of CA-MLCK alters peripheral SF architecture whereas CA-ROCK2 expression alters central SF architecture. F-actin images of (A) U2OS CA-MLCK and (B) U373MG CA-MLCK cultured in varying doxycycline concentrations. Arrow heads point to peripheral SFs and insets highlight peripheral SFs of interest. F-actin images of (C) U2OS CA-ROCK2 and (D) U373MG CA-ROCK2 cultured in varying doxycycline concentrations. Arrow heads point to central SFs and insets highlight central SFs of interest. Fluorescent intensity was normalized to the 0 ng/ml doxycycline concentration for all panels with the exception of (B) where the 0 ng/ml doxycycline condition is set at a higher intensity than the others. Scale bars = 10 µm, inset scale bars = 2 µm.

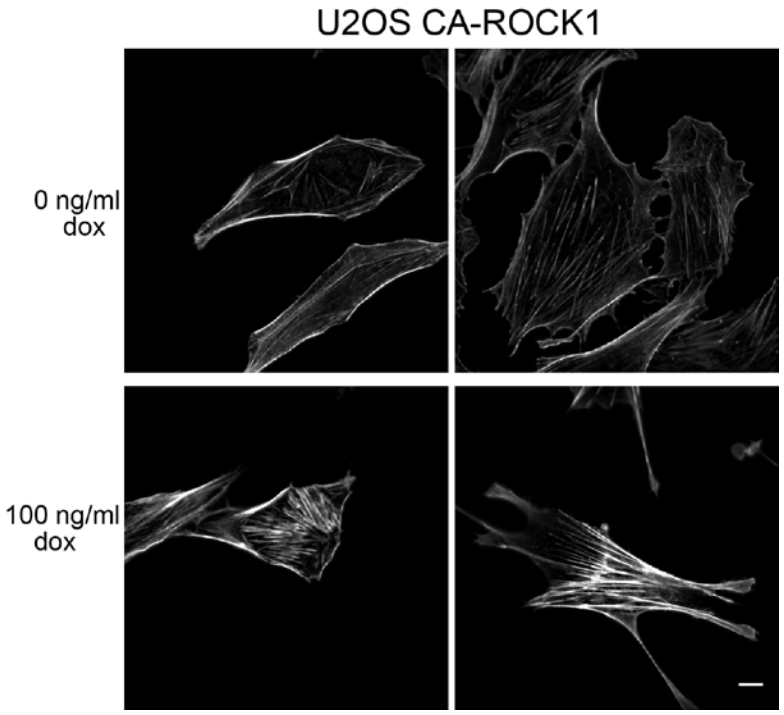

Figure 2.5: Representative images of F-actin in U2OS CA-ROCK1 cells cultured in the presence and absence of doxycycline. F-actin stain is based on phalloidin. Scale bars = 10 μm.

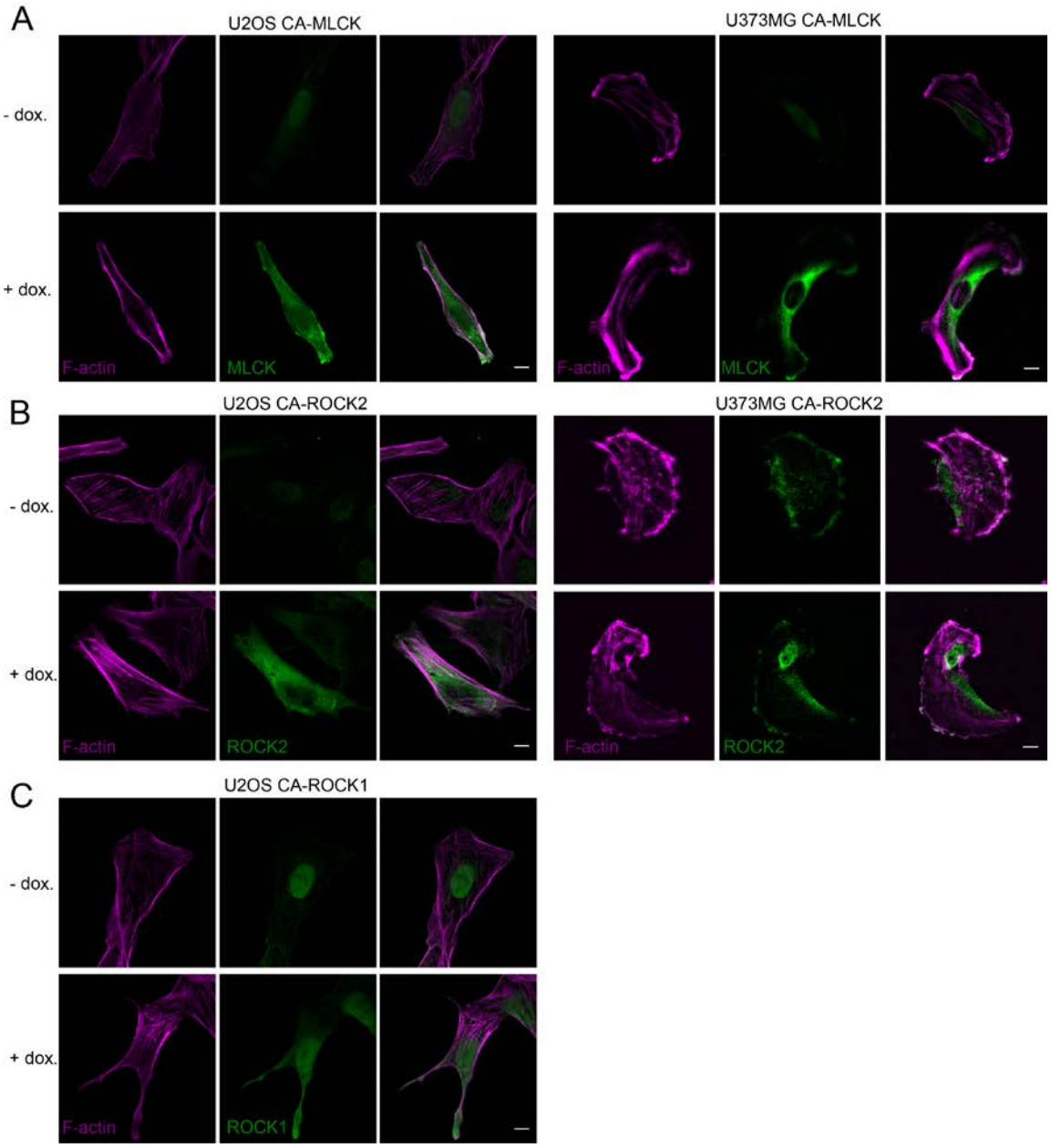

Figure 2.6: (A) Representative images of U2OS CA-MLCK (left) and U373MG CA-MLCK (right) cells cultured in the absence (top) and presence (bottom) of doxycycline. Cells were stained for MLCK (green, both endogenous and CA-MLCK) and F-actin (magenta). U2OS cells were stained with Abcam rabbit anti-MLCK and U373MG cells were stained with Sigma mouse anti-MLCK. (B) Representative images of U2OS CA-ROCK2 (left) and U373MG CA-ROCK2 (right) cells cultured in the absence (top) and presence (bottom) of doxycycline. Cells were stained for ROCK2 (green, both endogenous and CA-ROCK2) and F-actin (magenta). (C) Representative images of U2OS CA-ROCK1 cells cultured in the absence (top) and presence (bottom) of doxycycline. Cells were stained for ROCK1 (green, both endogenous and CA-ROCK1) and F-actin (magenta). Intensity of all images is normalized to the no-doxycycline conditions. Scale bars = 10 μm.

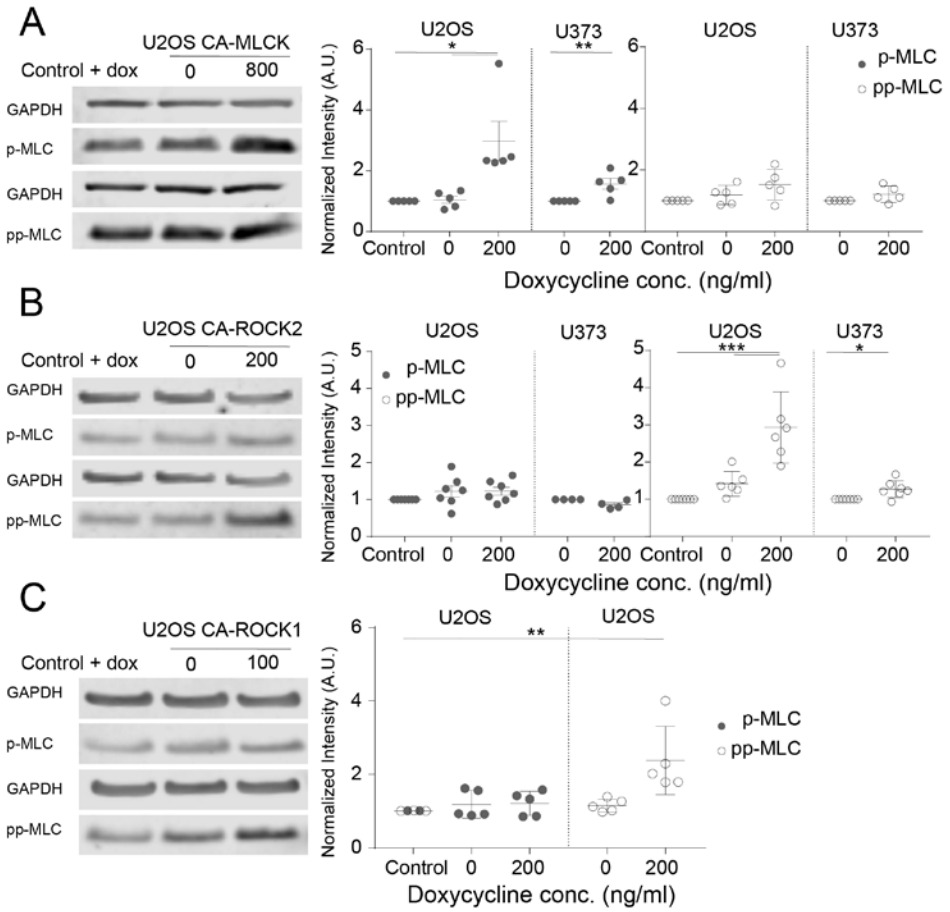

Figure 2.7: ROCK isoforms and MLCK preferentially phosphorylate MLC in the presence and absence of doxycycline. (A) Representative Western blots of U2OS CA-MLCK cells cultured in the presence and absence of doxycycline and probed for p-MLC or pp-MLC. Plots show quantification of p-MLC (grey circles, left graph) and pp-MLC (black circles, right) for both cell lines. For U2OS, bands were normalized to GAPDH and to control cell lines transduced with an empty vector and cultured in doxycycline. For U373MG, bands were normalized to GAPDH and to the 0 ng/ml doxycycline condition (n = 5 blots for both cell lines). (B) Representative Western blots of U2OS CA-ROCK2 cells cultured in the presence and absence of doxycycline and probed for p-MLC or pp-MLC. Plots show quantification of p-MLC (grey circles, left graph) and pp-MLC (black circles, right) for both cell lines. For U2OS, bands were normalized to GAPDH and to the control cell lines transduced with an empty vector and cultured in doxycycline. For U373MG, bands were normalized to GAPDH and to the 0 ng/ml doxycycline condition (U2OS: n = 6 blots; U373MG: n = 4 blots for p-MLC and n = 7 blots for pp-MLC). (C) Representative Western blots of U2OS CA-ROCK1 cells cultured in the presence and absence of doxycycline and probed for p-MLC or pp-MLC. Graphs show quantification of p-MLC (grey circles, left graph) and pp-MLC (black circles, right). Bands were normalized to GAPDH and to the control cell lines transduced with an empty vector and cultured in doxycycline (n = 5 blots). For all plots, statistical differences (* = $p < 0.05$, ** = $p < 0.01$, *** = $p < 0.005$) were using identified using ANOVA followed by Student's t-test (U2OS CA-ROCK2), Kruskal Wallis followed by Dunn's non-parametric test for U2OS CA-MLCK and U2OS CA-ROCK1, and Student's t-test for U373MG CA-MLCK and CA-ROCK2 cells.

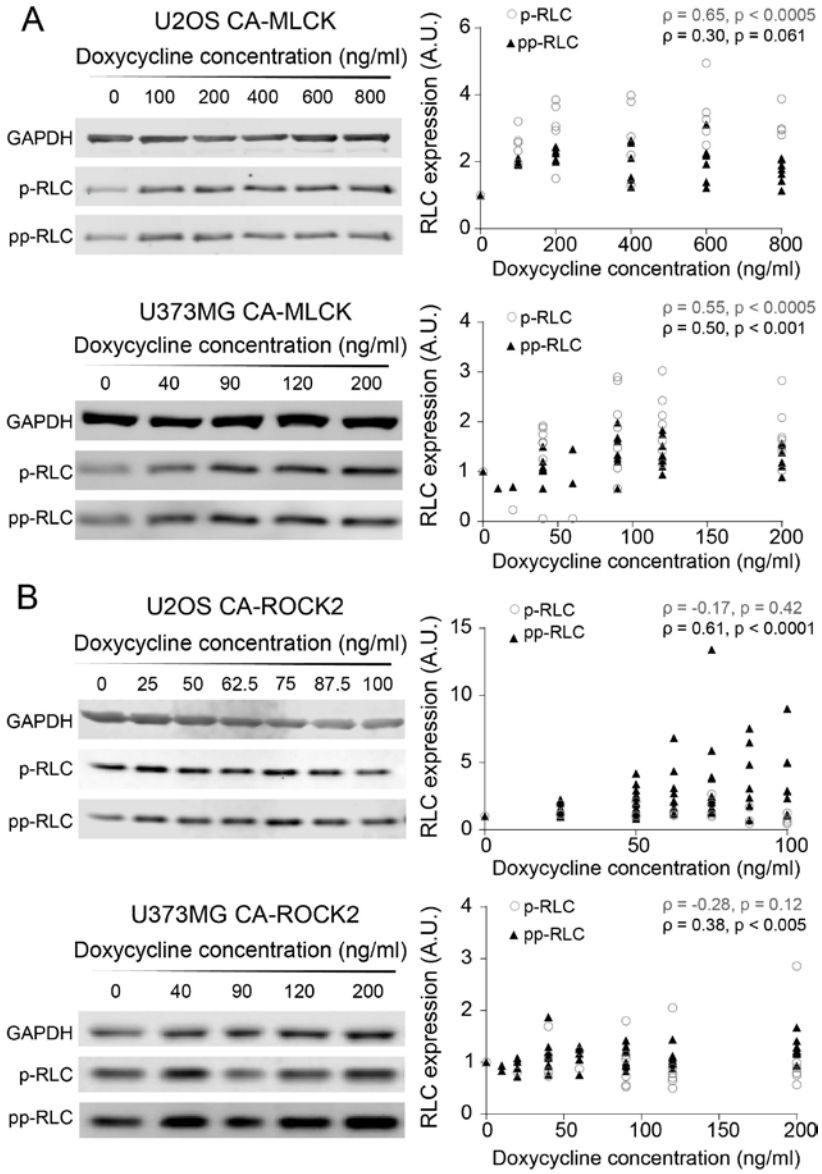

Figure 2.8: Graded increases in CA-MLCK and CA-ROCK2 produce graded changes in p-RLC and pp-RLC. (A) Representative Western blots probed for p-RLC and pp-RLC in U2OS CA-MLCK (top) and U373MG CA-MLCK (bottom). Phosphorylation levels were quantified, normalized to GAPDH and CA-MLCK + 0 ng/ml doxycycline for each cell line and plotted below the respective Western blots. p-RLC is shown by empty grey circles whereas pp-RLC is shown by dark grey circles (U2OS: n = 6 blots for p-RLC (mouse) and 7 blots for pp-RLC (rabbit) blots; U373MG: n = 8 blots for p-RLC (mouse) and n = 9 blots for pp-RLC (rabbit)). (B) Representative Western blots probed for pp-RLC and p-MCL in U2OS CA-ROCK2 (top) and U373MG CA-ROCK2 (bottom). Phosphorylation levels were quantified, normalized to GAPDH and CA-ROCK2 + 0 ng/ml doxycycline for each cell line and plotted below the respective Western blots. p-RLC is shown as empty, black circles whereas pp-RLC is shown as solid, dark grey circles (U2OS: n = 4 blots for p-RLC (mouse) and n = 11 blots for pp-RLC (rabbit) expression; U373MG:

n = 9 blots for pp-RLC (rabbit) and n = 6 blots for p-RLC (mouse)). Statistical parameters shown represent the Spearman's rank correlation coefficient (ρ) and p-value.

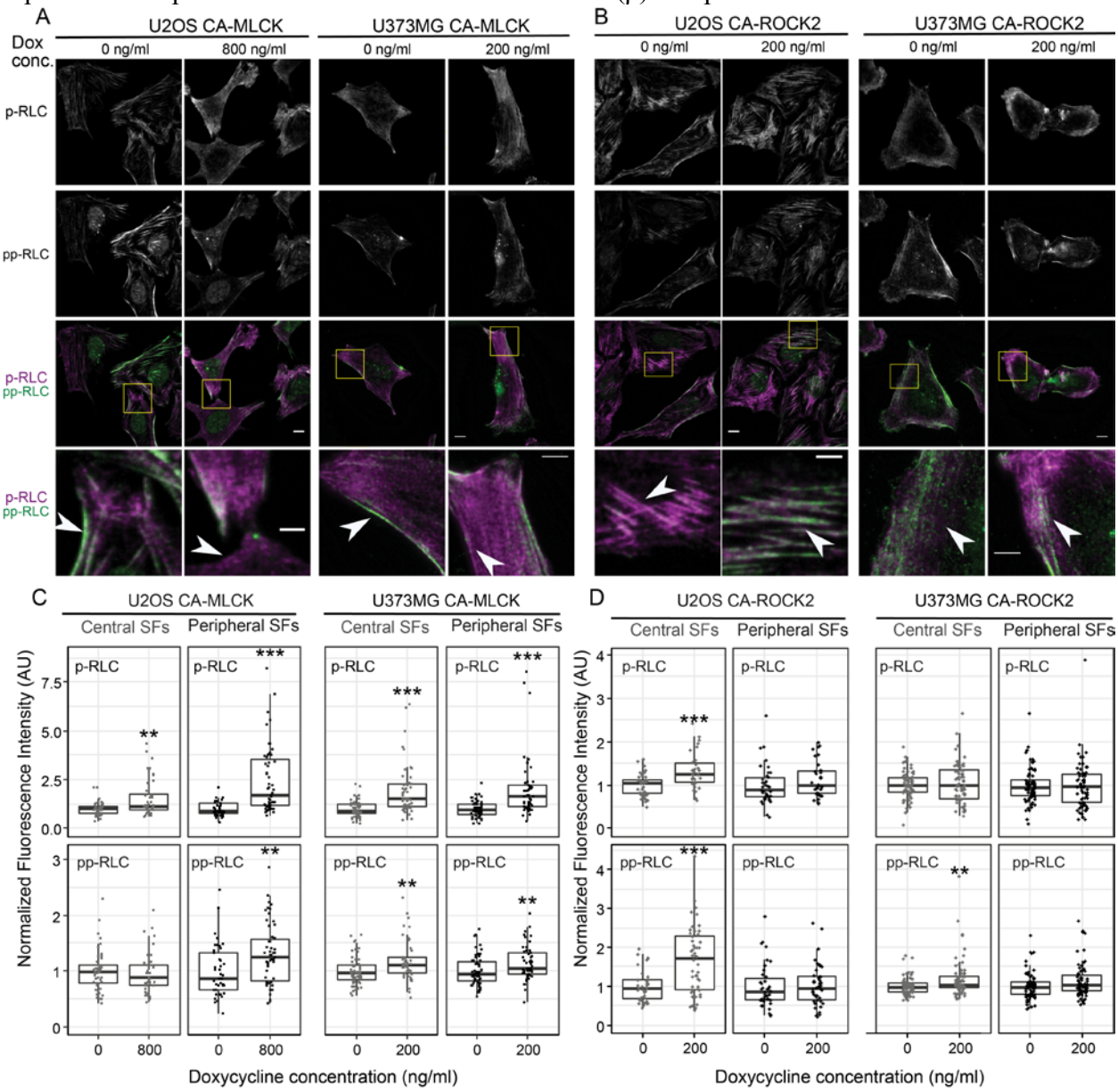

Figure 2.9: CA-MLCK expression regulates RLC phosphorylation in peripheral SFs whereas CA-ROCK2 expression regulates RLC phosphorylation in central SFs. Representative fluorescence images of (A) U2OS CA-MLCK (left) and U373MG CA-MLCK (right) cells and (B) U2OS CA-ROCK2 and U373MG CA-ROCK2 cells cultured in the presence and absence of doxycycline stained for p-RLC (top row, third and fourth row in magenta) and pp-RLC (second row, third and fourth row in green). Scale bars = 10 µm, inset scale bars = 5 µm. Fluorescence intensity of all images is normalized to that of 0 ng/ml doxycycline for each condition. (C) Quantification of immunofluorescence intensity of p-RLC (top row) and pp-RLC (bottom row) within central (grey) and peripheral (black) SFs for U2OS and U373MG CA-MLCK cells cultured in the presence and absence of doxycycline (n = 46, 46, 41, 55, 62, 53, 60, 51 cells collected from 3 independent

experiments for each condition, respectively from left to right). Intensities were normalized to the average intensity value of either U2OS or U373MG CA-MLCK cells cultured in the absence of doxycycline for each experiment. (D) Quantification of immunofluorescence intensity of p-RLC (top row) and pp-RLC (bottom row) within central (grey) and peripheral (black) SFs for U2OS and U373MG CA-ROCK2 cells cultured in the presence and absence of doxycycline (n = 41, 32, 39, 31, 75, 72, 75, 71 cells collected from 3 independent experiments analyzed per condition respectively from left to right). Intensities were normalized to the average intensity value of either U2OS or U373MG CA-ROCK2 cells cultured in the absence of doxycycline per each experiment. (* = $p < 0.05$, ** = $p < 0.01$, *** = $p < 0.001$, Mann-Whitney Test).

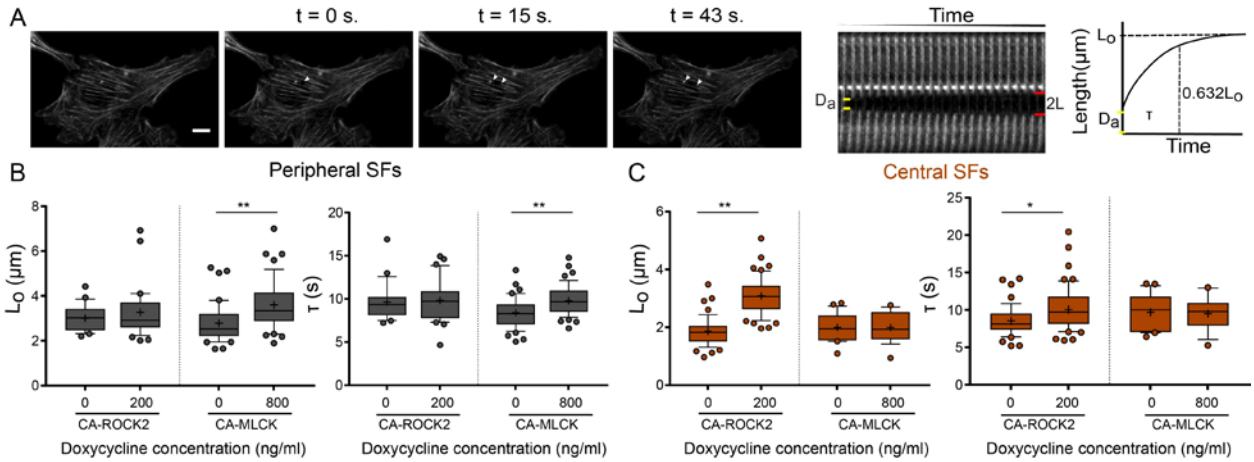

Figure 2.10: CA-MLCK and CA-ROCK2 regulate the viscoelastic properties of distinct SF subpopulations. (A) SF Retraction analysis. D_a: SF material destroyed by ablation, 2L: distance between SF ends over time (L is the retraction distance of a severed SF fragment), t: time. L-t curves for each stress fiber are fit to a Kelvin-Voigt model to determine L_o, whose magnitude correlates with the SF's dissipated elastic energy, and τ, the viscoelastic time constant which reflects the ratio of viscosity to elasticity. (B) L_o and τ values of peripheral SF ablation for U2OS CA-ROCK2 and CA-MLCK cells cultured in the presence and absence of doxycycline (n = 21, 32 for U2OS CA-ROCK2, n = 42, 47 for U2OS CA-MLCK) (C) L_o and τ values of central SF ablation for U2OS CA-ROCK2 and CA-MLCK cells cultured in the presence and absence of doxycycline (n= 49, 51 for U2OS CA-ROCK 2, n = 22, 19 for U2OS CA-MLCK). Boxes represent 25^{th} and 75^{th} percentiles; whiskers represent 10^{th} and 90^{th} percentiles. Cross represents the mean of the distribution. Statistical differences calculated using Mann-Whitney (* = $p<0.005$, ** = $p<0.0005$). Scale bars = 10 μm.

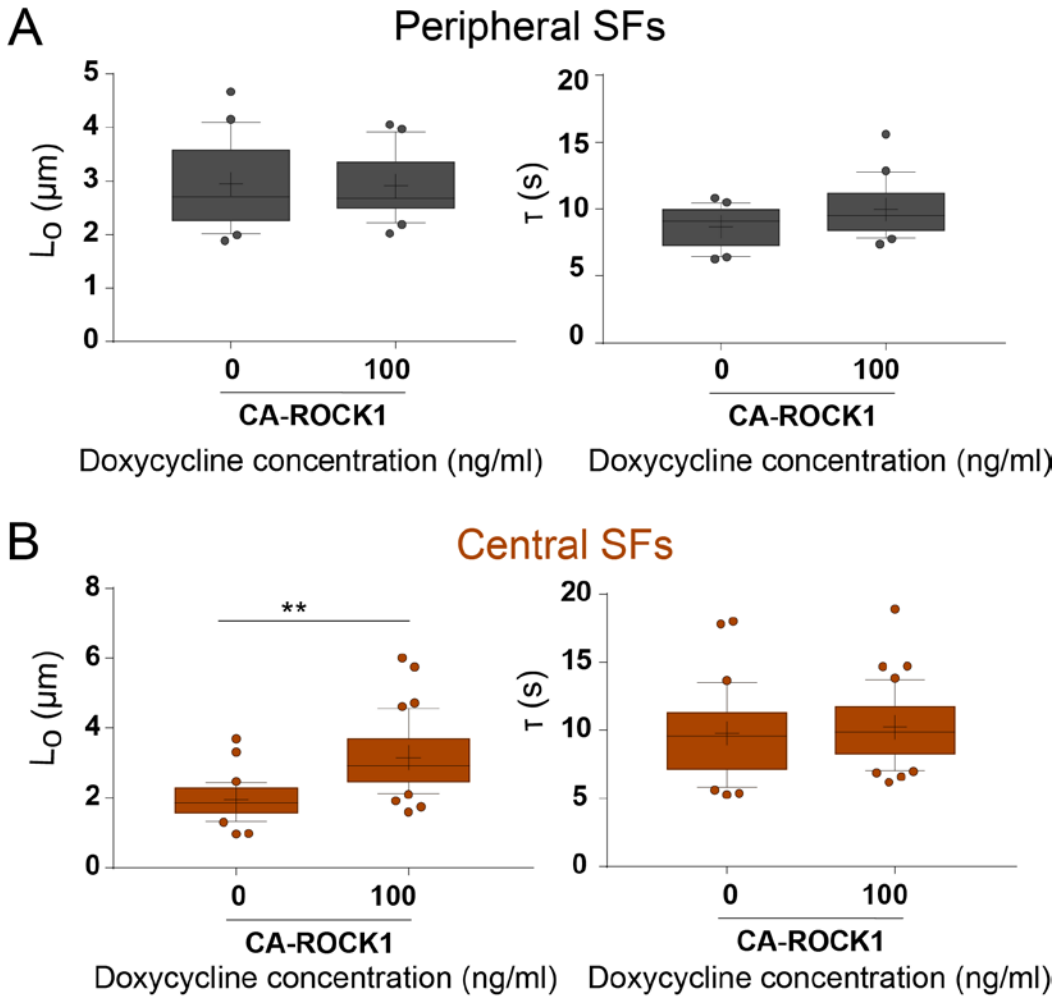

Figure 2.11: In U2OS cells, CA-ROCK1 preferentially regulates the viscoelastic properties of central SFs. (A) L_o and τ values of peripheral SF ablation of U2OS CA-ROCK1 cells cultured in the presence and absence of doxycycline (n = 24 and 24 respectively). (B) L_o and τ values of central SF ablation of U2OS CA-ROCK1 cells cultured in the presence and absence of doxycycline (n = 34 cells for 0 ng/ml and 43 cells for 100 ng/ml doxycycline). Boxes represent 25th and 75th percentiles; whiskers represent 10th and 90th percentiles. Cross represents the mean of the distribution. Statistical differences were calculated using Mann Whitney test. (** = $p < 0.001$).

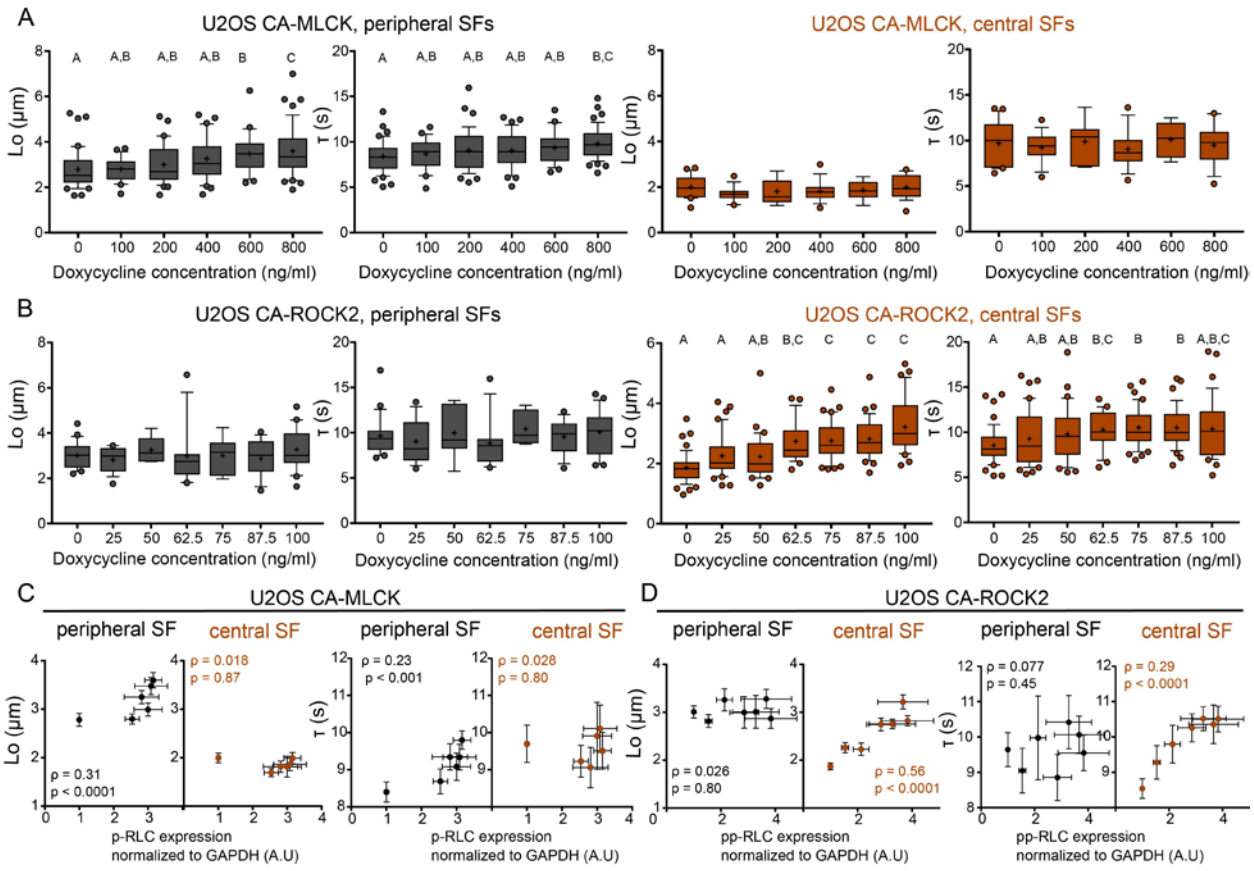

Figure 2.12: SF mechanical properties increase in a graded manner following graded expression of RLC phosphorylation. (A) L_o and τ values of peripheral (left, dark grey) and central (right, orange) SF ablation of CA-MLCK cells cultured in varying concentrations of doxycycline (n = 42, 24, 39, 37, 25, 47 cells for peripheral SF ablation of CA-MLCK, n = 22, 14, 7, 14, 9, 19 cells for central SF ablation). (B) L_o and τ values of peripheral (left, dark grey) and central (right, orange) SF ablation of CA-ROCK2 cells cultured in varying concentrations of doxycycline (n = 21, 15, 6, 16, 6, 14, 21 cells for peripheral SF ablation, n = 49, 41, 31, 25, 40 and 38 cells for central SF ablation). A, B, and C statistical families show statistical differences ($p < 0.05$) determined using Dunn's test for multiple comparisons of nonnormally distributed data. Boxes represent 25th and 75th percentiles; whiskers represent 10th and 90th percentiles. Cross represents the distribution mean. (C) Viscoelastic retraction parameters L_o and τ of peripheral (black) and central SFs (orange) of U2OS CA-MLCK cells plotted versus the observed increase in p-RLC (replotted from Figure 2.8A). (D) Viscoelastic retraction parameters Lo and τ of peripheral (black circles) and central SFs (solid orange circles) and peripheral (black circles) of U2OS CA-ROCK2 cells plotted versus the observed increase in pp-RLC (replotted from Figure 2.8B). Orange values correspond to central SF ablation Spearman's rank correlation coefficient analysis whereas black values correspond to Spearman's rank correlation coefficient analysis for peripheral SF ablation. Error bars of x-axes values were determined based on Western blot quantifications shown in Figure 2.8. All error bars represent SEM.

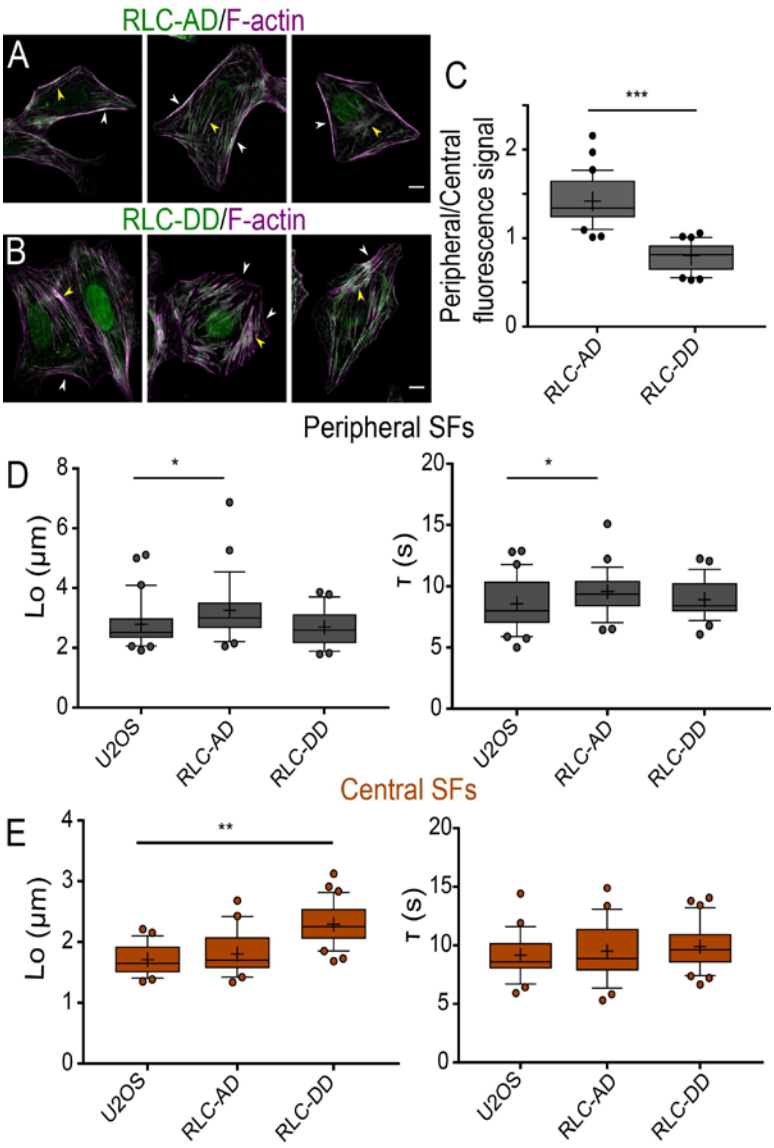

Figure 2.13: Expression of phosphosmimetic p-RLC and phosphomimetic pp-RLC phenocopy the changes in SF viscoelasticity induced by CA-MLCK and CA-ROCK. Representative images of (A) U2OS RFP-LifeAct GFP-RLC AD and (B) U2OS RFP-LifeAct GFP-RLC DD. Images are taken using the GFP channel for the phosphomimetic constructs and phalloidin for SFs. White arrows point to peripheral SFs whereas yellow arrows point to central SFs. (C) Quantification of GFP signal localization as a ratio of localization on peripheral over central SFs (n = 36 for GFP-RLC AD and 30 for GFP-RLC DD). (D) L_o and τ values of peripheral SF ablation for U2OS RFP-LifeAct, U2OS RFP-LifeAct GFP RLC-AD and U2OS RFP-LifeAct GFP RLC-DD cells (n = 21, 28, 28 cells respectively). (D) L_o and τ values of central SF ablation for U2OS RFP-LifeAct, U2OS RFP-LifeAct GFP RLC-AD and U2OS RFP-LifeAct RFP RLC-DD cells (n = 22, 23, 31 cells respectively). Boxes represent 25^{th} and 75^{th} percentiles; whiskers represent 10^{th} and 90^{th} percentiles. Cross represents the distribution mean. Statistical differences calculated using Mann-Whitney tests (* = $p < 0.05$, ** = $p < 0.001$, *** = $p < 0.0001$). Scale bars = 10 μm.

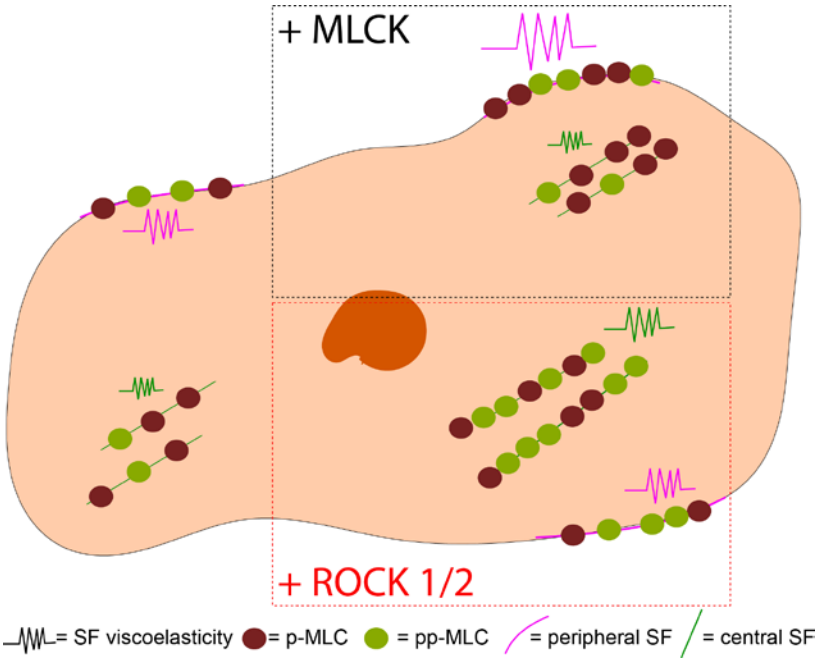

Figure 2.14: Model of subcellular regulation of RLC phosphorylation and SF viscoelastic properties. Schematic to illustrate findings. MLCK-induced p-RLC localizes and regulates the viscoelastic properties of peripheral SFs them whereas ROCK1 and 2-induced pp-RLC localizes and regulates viscoelastic properties of central SFs.

Chapter 3:
Engineering protein activity using CRISPR/Cas9 gene editing and an inducible promoter

Jasmine H. Hughes[1,2], Kirsten L. Fetah[2], Paola A. Lopez[1,2], Sanjay Kumar[2,3,4]

[1]UC Berkeley - UCSF Graduate Program in Bioengineering, [2]Department of Bioengineering, and [3]Department of Chemical and Biomolecular Engineering, University of California, Berkeley, Berkeley, CA.

ABSTRACT

Non-muscle myosin II (NMII) plays a central role in the transduction of mechanical signals from the extracellular matrix (ECM), and interpretation of these signals plays a vital role in cell processes such as focal adhesion formation and cell migration. NMII is strongly regulated by phosphorylation of its light chains (RLCs), however the relationship between NMII activity and cell behavior is often nonlinear. Important contributions to our understanding of mechanotransduction have been made by tuning the properties of synthetic ECMs along gradients of stiffnesses, topographies or ligand densities. However, relatively few options exist for modulating protein activity across a gradient. Here we present a genetic strategy for controlling the activity of NMII by the RLC kinase mysoin light chain kinase (MLCK) from virtually zero to supraphysiological levels of activity. Our approach combines an inducible promoter system with CRISPR/Cas9-mediated knockout of the endogenous protein. We demonstrate the power of this approach by varying RLC phosphorylation levels along a gradient. We find that knockout of the long non-muscle MLCK (nmMLCK) isoform impacts cell processes like migration and focal adhesion formation to a very modest degree, but that these behaviors are quite sensitive to overexpression of the shorter, smooth muscle MLCK (smMLCK) isoform. Subsequent efforts to knock out smMLCK were unsuccessful, suggesting that expression of smMLCK or of both isoforms is important for cell survival.

Introduction

Cells continuously pull on their surrounding microenvironment, generating contractile forces through the interaction of non-muscle myosin II (NMII) and cytoskeletal actin filaments. This force is transmitted through focal adhesions to the cell-matrix interface, and resisted by the stiffness of the extracellular matrix. This process is vital for mediating mechanical regulation of adhesion, cell migration and cancer progression (145). However, our understanding of this signal transduction pathway is attenuated by its sometimes nonlinear behavior and our lack of tools for probing nonlinearity in biology (194).

For example, focal adhesion size appears to biphasically depend on NMII activity, with increasing contractility increasing focal complex maturation until the focal adhesions can no longer sustain the force exerted (195). Similarly, actin retrograde flow speeds biphasically regulate force generation at focal adhesions (196). The activity of NMII is strongly promoted by phosphorylation of its regulatory light chains (RLCs), which can be phosphorylated once (p-RLC) or twice (pp-RLC), and the effects of phosphorylation produce nonlinear changes in myosin's tension-generating capacities. An early study found increasing smooth muscle myosin II RLC phosphorylation increases its force generation capacity until saturating at 20% phosphorylation (197). We have recently shown that actomyosin stress fiber viscoelasticity varies non-linearly depending on NMII light chain (RLC) phosphorylation levels (198).

Mechanistic models have provided valuable insight to nonlinear behaviors in mechanobiology (199). These models have been refined through experimental efforts in which extracellular matrix parameters, such as ligand spacing or substrate stiffness, were modulated along a gradient, enhancing our understanding of the key molecular players in mechanotransduction (81, 82). Despite NMII's central role in the mechanotransduction process, there exist relatively few analogous tools available to probe NMII-dependent behaviors from within the cell that similarly allow for graded control. Much of our present understanding arose from pharmacological inhibition or RNA interference. For example, it was recently shown that the optimum substrate stiffness for cell migration speeds could be modified by inhibition of myosin motors by the myosin inhibitor blebbistatin (111). However, these on-off approaches mask non-linearity and prohibit exploration of the effects of graded NMII activity, as encountered physiologically. Quantitatively relating myosin activity to downstream phenotypic outputs would enhance our ability to understand and control these biomechanical processes (172).

Our lab has developed a genetic system to produce graded changes in NMII activity through the application of an inducible promoter governing expression of a constitutively active (CA) copies of the NMII activators myosin light chain kinase (MLCK) or rho-associated kinases 1 and 2 (ROCK1 and ROCK2) (19, 198). With this system, we demonstrated that ROCKs and MLCK differentially contribute to actomyosin stress fiber viscoelasticity by preferentially producing different phosphospecies of RLC. However, these studies were performed by inducing overexpression of these kinases on top of the endogenous background. We have previously induced expression of dominant negative (DN) mutants to study sub-physiological levels of activity on mechanobiological outputs, however DN constructs have fallen out of favor due to their poorly-defined off-target effects (20). Furthermore, this strategy did not permit modulation of NMII activity from sub-physiological to supraphysiological thresholds within a single cell line.

Here, we present a technique to control a target protein from virtually zero activity to supraphysiological activity levels within a single cell line by combining CRISPR/Cas9 gene editing with an inducible promoter. We show we can use this system to control MLCK activity, and thus control levels of p-RLC. Interestingly, we discover that focal adhesion formation and cell migration are regulated by overexpression of CA-smMLCK but not by knockout of the endogenous non-muscle MLCK isoform. Our findings suggest that these isoforms may play compensatory roles, highlighting a need to target both isoforms in RNA interference or knockout approaches.

Results

Design and implementation of inducible expression plus endogenous knockout

While inducible protein constructs have provided insight into the relationships between protein activity or protein expression and cell behaviors, these studies were undertaken with expression of the endogenous protein present. In consequence, it has not yet been possible to explore the impact of a protein of interest on a phenotype of interest at graded levels of expression below endogenous levels. Furthermore, results may be confounded by regulation of the activity of the endogenous protein. We sought to improve this strategy by combining it with CRISPR/Cas9 editing to halt expression of the endogenous protein (Figure 3.1A).

As a proof-of-concept experiment, we chose to use MLCK as our protein of interest due to the availability of a well-characterized constitutively active (CA) mutant (19, 198). This rabbit smooth muscle MLCK construct is mutated in the auto-inhibitory binding domain, rendering it constitutively active (CA) (169, 198). We performed this experiment in U373MG glioblastoma cells because they are mechanosensitive and highly motile. Immunoblotting with the K36 monoclonal anti-MLCK antibody showed this cell line expressed just one MLCK isoform at approximately 220 kDa, corresponding most likely to the non-muscle MLCK (nmMLCK) isoform. The gene for MLCK encodes for two isoforms with the same catalytic domain: the full-length nmMLCK and as well as a 130kDa smooth muscle MLCK (smMLCK) isoform, which is transcribed beginning from a promoter within intron 14. The smMLCK isoform is identical to the C-terminus of nmMLCK and lacks several of the actin-binding domains present in the nmMLCK N-terminus (200, 201).

We transduced cells first with the pSLIK promoter system controlling expression of CA smooth muscle MLCK (CA-smMLCK), then transduced with lentiCRISPR v2 containing Cas9 and a guide RNA (gRNA) targeted at exon 9 (Figure 3.1A). Because CA-smMLCK was isolated from rabbit, this gRNA targets only the endogenous human gene. As a control, we also produced a cell line containing a non-targeting gRNA and an empty pSLIK vector that we refer to here as “n.t..”

We hypothesized that this strategy should allow us to control total MLCK expression, and thus MLCK activity given our use of a CA construct, by modulating the concentration of doxycycline in the culture media (Figure 3.1B). We predicted a plateauing relationship between doxycycline concentration and construct expression based on past experience with this promoter system (198). This strategy would therefore allow us to quantitatively map the relationship between MLCK activity and phenotype (Figure 3.1C).

Validation of genetic strategy

To ensure we obtained a uniform knockout of the endogenous protein at both chromosomes, we clonally expanded and tested 20 cell lines, eventually settling on one clonal line, referred to here as "gRNA-C," for further experimentation. We observed a complete absence of a band at 220 kDA, indicating that translation of full-length nmMLCK had indeed been halted (Figure 3.2A). CA-smMLCK is lower in molecular weight than nmMLCK, allowing us to easily distinguish between the mutant and the endogenous protein. By varying the concentration of doxycycline in the media, we were able to modulate CA-smMLCK expression (Figure 3.2A-B). This graded control over MLCK activity produced a concomitant increase in phosphorylation of Ser19 of RLC (p-RLC; Figure 3.2A, C). Interestingly, we noted a much tighter dependence of CA-smMLCK expression and p-RLC expression on doxycycline concentration compared to our past work with this system (198). We hypothesize this decrease in noise is due to clonal expansion, which eliminates variation in the number of pSLIK cassettes received by each cell. By plotting p-RLC (Figure 3.2C) against CA-smMLCK (Figure 3.2B), we were able to examine the correlation between construct expression and RLC activation (Figure 3.2D). Interestingly, this relationship had a non-zero y-intercept. We have previously demonstrated that MLCK activity primarily phosphorylates RLC to p-RLC, while the Rho-associated kinases 1 and 2 (ROCK1 and ROCK2) chiefly produce diphosphorylation of RLC at Ser19 and Thr18 (pp-RLC) (198). It is possible that one of these other kinases produces a basal level of p-RLC.

CA-smMLCK expression but not nmMLCK knockout modulates mechanobiological phenotypes

Although we were able to increase p-RLC levels to approximately two-fold by altering doxycycline concentrations, we were surprised to note that knockout of nmMLCK did not reduce p-RLC levels compared to the cells receiving a non-targeting gRNA (Figure 3.3A). Interestingly, many mechanobiological phenotypes that we tested could be modulated by overexpression of the CA-smMLCK construct, but were not influenced by the nmMLCK knockout. For example, expression of CA-smMLCK increased migration speed while knockout of nmMLCK had no effect (Figure 3.3B). Migration persistence however did show a weak increase upon knockout of nmMLCK that was rescued with expression of smMLCK (Figure 3.3C). Increasing smMLCK activity but not knockout of nmMLCK altered cell area (Figure 3.3D), although neither alteration in MLCK activity changed the ability of the cells to polarize (Figure 3.3E). Cells with high levels of smMLCK activity showed a dramatic increase in the number of focal adhesions (Figure 3.3F-G) but not in the median focal adhesion size (Figure 3.3H), while knockout of nmMLCK showed no effect on focal adhesion number or size. We found it surprising that modulation of smMLCK could have such prominent effects on migration speed and focal adhesion formation while removal of endogenous nmMLCK had so little impact.

MLCK antibodies show isoform-specific binding despite recognizing homologous regions

Because overexpression but not knockout of MLCK appeared to impact mechanobiology, we wished to verify that our finding that our cells expressed only the nmMLCK isoform was correct. The K36 monoclonal antibody we used to screen knockouts has been reported by the manufacturer (Sigma-Aldrich M7905, produced in mouse) and by other academic labs to recognize the a protein at 200-200 kDa as well as a protein at 130-150 kDa, presumably corresponding to the nmMLCK

and smMLCK isoforms (202–204). In our hands, this antibody detects only a band at 220 kDa in U373 cells. To confirm this finding, we probed for MLCK with a different MLCK antibody (clone EP1458Y, Abcam 7609, produced in rabbit). Because the two antibodies were produced in different species, we were able to visualize band recognition with both antibodies simultaneously. To our surprise, the rabbit MLCK antibody detected a protein at 130 kDa and did not detect a protein at 220 kDa (Figure 3.4). We hypothesize that the U373MG cells do indeed express both smMLCK and nmMLCK and that these two antibodies do not always recognize both MLCK isoforms. This finding is challenging to confirm via RT-PCR due to the homology between the two isoforms.

nmMLCK/smMLCK -/- cells could not be clonally expanded

In light of the discovery that this cell line expresses both smMLCK and nmMLCK, we attempted to knock out the smMLCK protein. We designed paired gRNAs targeting each side of the internal promoter site (ex: exon 12 and exon 15), since targeting this region has been shown to greatly inhibit smMLCK expression (205). We screened over 100 clonal populations, and although these lines showed heterogenous levels of smMLCK expression, none showed a complete absence of smMLCK (data not shown).

While a few groups have reported knockout of both isoforms in mice (206, 207) we wondered if perhaps the knockout of both isoforms was too lethal for our cells. We tried using the MLCK inhibitor ML7 (208) to test this hypothesis. ML7 is thought to bind to MLCK competitively with respect to ATP, inhibiting its kinase activity (209). Interestingly, inhibition of MLCK with ML7 did not lower p-RLC levels (Figure 3.5A-B) nor did it inhibit proliferation (Figure 3.5C-D). We did attempt higher concentrations of ML7 (Figure 3.6), which was lethal to cells, however at these concentrations ML7 could have off-target effects (208).

Discussion

Although some processes in biology show nonlinear dependence on protein activity, there exist relatively few tools for investigating the relationship between a phenotype and a protein's activity at multiple activity levels. Here, we present a strategy to vary the activity of MLCK from virtually zero to supraphysiological levels of activity by combining a doxycycline-inducible promoter with CRISPR/Cas9 gene editing. We demonstrate that we are able to vary p-RLC levels along a gradient. However, we were surprised to find that the phenotypes that could be modulated by overexpression of CA-smMLCK were not influenced by nmMLCK knockout. By trying alternative antibodies, we subsequently find that U373 cells express both smMLCK and nmMLCK isoforms. While attempts to target endogenous smMLCK were not successful, the lethality of complete MLCK knockout could not be demonstrated since we did not see reduced proliferation upon pharmacological inhibition of MLCK.

While the phenotypes studied here were altered only by activating MLCK above physiological levels and not below endogenous levels, our approach could be applied to other proteins of interest or in other cell types. The engineering considerations presented here should apply to other systems equally. First, it is important that the induced protein not be targeted by the gRNA. This can be achieved, as we have done here, by using cDNA isolated from another species. Alternative approaches include introducing silent point mutations in the cDNA, or transiently transfecting cells

with Cas9 and allowing for it to degrade prior to transduction with the inducible construct instead of lentiviral delivery of Cas9. Second, endogenous regulation of the target protein must be considered. We avoided this issue by using a CA mutant of MLCK. Learning from our experience here presents a third consideration of where to target the endogenous gene. We chose to target a relatively early exon due to fears to creating a partial protein from the N-terminus that may create a DN mutant or other mutant with unexpected behavior (210). However, this strategy did not similarly delete the unexpected smMLCK isoform. To specifically disrupt MLCK's kinase activity, it may have been more effective to target a region of the catalytic domain. Fourth, we established a control line using a non-targeting gRNA, however we did not clonally select this population. While this line may therefore exhibit additional heterogeneity than the experimental line, we reasoned that at least this variation would likely bracket the clonally expanded population whereas a clonally-selected control line may, by chance, be somewhat different from the clonally selected experimental line. Finally, based on the results we show here, others who apply inducible promoter systems even in the absence of CRISPR/Cas9-mediated genetic editing may wish to clonally select cells to reduce variation in protein expression in response to doxycycline.

Due to the high homology between smMLCK and nmMLCK, most studies attempting to differentiate between the isoforms use separation by molecular weight followed by antibody detection (211, 212). Based on our finding that absence of a 130 kDa or 210 kDa band is not necessarily indicative of an absence of that protein, we caution against using this screening approach and instead recommend using multiple anti-MLCK antibodies or alternative detection methods where possible for screens.

That we were unable to inhibit expression of both MLCK isoforms could suggest that some MLCK activity may be necessary for the Ser19 phosphorylation event in at least this cell line. However, this result is difficult to resolve with the findings by two independent groups who report MLCK knockout mouse models. The first group to publish this result noted embryos develop to full size, greatly surprising the authors, but die within hours after delivery (206). These pups show abnormalities in cardiac development, and their smooth muscle cells reportedly show no MLCK of either isoform detectable via Western blot. However, this study is difficult to interpret since no western blots or other validation data is shown. The second report of MLCK-null mice describes more detailed methodology of the Cre/LoxP system and shows more thorough characterization of the knockout (204, 207). The authors validated knockout through RT-PCR and through western blot with the K36 antibody. They reported variation in the efficacy of the knockout between different tissues, and so proceeded with further characterization in smooth muscle cells, which showed the highest level of knockout. The authors observed significant gastrointestinal abnormalities in the mice, and found that the knockout smooth muscle cells showed dramatically decreased levels of p-RLC and contractile ability. It is however, somewhat difficult to assess the knockout since not every blot includes both isoforms, the isoforms expressed in a given tissue type are not always consistent, and some blots show partial knockout while others show complete knockout (204, 207).

The question therefore remains regarding the relative contributions of the MLCK isoforms and of the ROCK isoforms towards production of p-RLC. We have previously demonstrated that MLCK preferentially produces p-RLC while ROCK preferentially produces pp-RLC (198) and even high levels of ROCK activity did not impact p-RLC levels. It is not clear whether ROCK can produce

p-RLC in physiological conditions in the absence of MLCK. This hypothesis has been difficult to test in part because ROCK promotes RLC phosphorylation indirectly through inhibition of myosin phosphatase (MYPT1), which dephosphorylates NMII, as well as through direct kinase activity (213). The relative roles of nmMLCK and smMLCK are similarly unclear. We find here that inhibition of only the nmMLCK isoform does not reduce p-RLC levels. It has been reported elsewhere that in smooth muscle cells, inhibition of only the smMLCK isoform did not reduce p-RLC levels (201). Our finding that ML7 does not decrease p-RLC was surprising, but this result has been reported by others (152). It is also possible that MLCK plays an RLC-independent role important for cell survival (204, 210). Some of these questions could be resolved by repeating the process described here with cells cultured in doxycycline continuously following introduction of Cas9 such that some level of MLCK is always expressed.

Acknowledgements

The authors gratefully acknowledge financial support from the following sources: the Natural Sciences and Engineering Research Council of Canada (NSERC, PGS D 555229 awarded to J.H.H.), the Siebel Scholars program (J.H.H.), UC Berkeley's Student Mentoring and Research Teams (SMART) program (K.L.F. and J.H.H.), the National Sciences Foundation (NSF, awarded to P.A.L.), the W.M. Keck Foundation (S.K.) and the National Institutes of Health (R01GM122375 awarded to S.K.). The authors thank E. Kassianidou for insightful discussions on this topic, Bob Lesch and Professor Randy Schekman for the use of their Odyssey, and Jacob Corn and Elena Zelin for their help with nucleofection of Cas9.

Methods

Cell lines and reagents

Flag-tagged MLCK ED785-786KK (kindly provided by Dr. Gallagher, Indiana University, USA) was cloned into the lentiviral vector pSLIK-Venus containing the TRE tight doxycycline-inducible promoter (Addgene # 84647 for CA-smMLCK) (13, 166, 169). This rabbit smooth muscle MLCK construct is mutated in the auto-inhibitory binding domain (ED773-774KK of the construct, which aligns with ED785-786KK in wild-type MLCK), rendering it constitutively active (CA) (198). Control cell lines were also established containing empty pSLIK. Guide RNAs (gRNAs) were designed using E-CRISP (214) and lack of recognition of the rabbit MLCK was confirmed using NCBI BLAST. The following gRNAs were then cloned into lentiCRISPR v2 (215): nmMLCK-targeting gRNA-A: CGGGATTCCAAAGCCTGAAG; nmMLCK-targeting gRNA-C: GTCCAGCCACCTTCCCCACC, non-targeting (n.t.), confirmed previously (216): GCTGATCTATCGCGGTCGTC. Lentiviral particles for each plasmid were packaged in 293T cells. Human U373 glioblastoma cells (ATCC HTB-17) were first transfected with pSLIK empty vectors or with pSLIK CA-smMLCK vectors at an MOI of 0.5 IU/cell. Venus-positive pSLIK CA-MLCK cells were then transfected with lentiCRISPR plasmids containing an MLCK-targeting gRNA and venus-positive pSLIK Empty cells were transfected with lentiCRISPR plasmids containing the non-targeting gRNA. Each line was selected with 0.6 μg/mL puromycin, and was then seeded at one cell per well in a 96-well plate using serial dilution. 10-20 colonies per cell line were expanded, and deletion of endogenous MLCK was confirmed via western blot. The clonal

knockout line isolated for gRNA-A showed a shift in molecular weight for the CA-smMLCK construct so we proceeded exclusively with the gRNA-C line for future experiments. The following gRNAs were designed for smMLCK: CACGGGCACGTACACCTGCG (exon 11), CTTGGACAGTCATAGTGACC (exon 12), GTGACCGCTATGGGTCCCTG (exon 15), TGGCACCTTCTCAGGCACGG (exon 15), GTTCAGCGTCCAGATGATGG (exon 15), GTGCTCCTGCCAAGTCACCG (exon 16), TGTGTAGCCAAGAATGACGC (exon 16) and pairwise combinations of these gRNAs were delivered with Cas9 through nucleoporation as described previously (217). Cells were sorted into two 96-well plates per combination and cell lines were clonally expanded. ATCC U373MG cells have been demonstrated to be of the same genetic origin as U251 cells, although these two lines have since diverged and demonstrate some phenotypic and karyotypic differences (192). Short tandem repeat sequencing confirmed the identity of these cells. Cells were confirmed mycoplasma-negative thrice per year. Cells were cultured in DMEM supplemented with 10% calf serum (JR scientific), 1% penicillin/strep, 1% Non-essential amino acids and 1% sodium pyruvate (Thermo Fischer Scientific). Doxycycline was added to the culture media at the specified concentration two days before each experiment to induce CA-MLCK. ML7 (1-(5-Iodonaphthalene-1-sulfonyl)-1H-hexahydro-1,4-diazepine hydrochloride, Sigma Aldrich, I2764) was dissolved to 10 mM in dimethyl sulfoxide (DMSO,), and equal volumes of DMSO were used as a vehicle control.

Western blots

Lysis buffer was prepared from 1% protease inhibitor cocktail (Cell Signaling Technologies, #5871S), 1% phosphatase inhibitor (EMD Millipore, 524624), 4.1 μg/ml sodium molybdate and 1.4 μg/ml sodium fluoride in radioimmunoprecipitation assay (RIPA) buffer (Sigma-Aldrich, R0278). Cells were lysed on ice to preserve protein phosphorylation and all reagents were pre-chilled. Protein concentration was determined via bicinchonic acid (BCA) assay (Thermo Fisher Scientific, 23228) and sample concentration was normalized by adding appropriate volumes of lysis buffer. Lysates were reduced with lithium dodecyl sulfate (LDS, Thermo Fisher Scientific, NP0007) and reducing agent (Life Technologies, NP0009) at 95˚C for 5 minutes. Electrophoresis was performed in an XCell SureLock chamber (Thermo Fischer Scientific) at 170 V for 65 minutes in a 4-12% Bis-Tris gel (Invitrogen, NP0323) in MOPS buffer (Life Technologies, NP001). Protein was then transferred onto a polyvinylidene difluoride (PVDF) membrane (Life Technologies, LC2002) at 4V for 16 hours at 4°C in transfer buffer (Invitrogen, NP0006) with 10% methanol. Membranes were blocked (LI-COR, 927) for at least 1 hr, then primary antibodies were added and the membrane was incubated overnight at 4°C. Unbound primary was washed off in tris-buffered saline and Tween-20 (TBST), and membranes were then incubated in secondary antibodies diluted in blocking buffer for 1 hr at room temperature. Unbound secondary was washed off in TBST and membranes were imaged on an Odyssey system. The following primary antibodies were used: anti-MLCK (Abcam 76092, produced in rabbit), anti-MLCK (Sigma-Aldrich M7905 clone K36, produced in mouse), anti-GAPDH (Sigma-Aldrich, G8795), anti-phosphorylated myosin light chain 2 (Ser19) (Cell Signaling Technology, 3675). The following secondary antibodies were used: IRDye 680RD goat anti-rabbit (LI-COR, 925-68071), IRDye 800RD goat anti-mouse (LI-COR, 925-32210). ImageJ's (NIH) standard gel analyzer tool was used to quantify background-subtracted band intensity (218).

Focal adhesion staining

Glass coverslips were coated with 30 mg/ml of fibronectin for 2 hr at 37°C, then rinsed in PBS. Cells were seeded on the coverslips at 4000 cells/cm^2 in media of the appropriate doxycycline concentration and cultured for two days to allow expression of the inducible construct to stabilize. Cells were fixed in 3% paraformaldehyde (PFA; Fisher Scientific, #30525-89-4) in Dulbecco's PBS (Sigma-Aldrich, D1283) for 10 minutes at room temperature. Samples were washed thrice in PBS, permeabilized with 0.5% Triton-X for 15 minutes at room temperature, then blocked in 3 washes of 5% goat serum (GS) for a total time of 1 hr. Cells were then incubated in 1:150 anti-vinculin antibody (Sigma-Aldrich, V9131, produced in mouse) diluted in 1% GS overnight at 4°C. Cells were washed in 1% GS, incubated in 1:200 goat anti-mouse Alexa Fluor 647 conjugate (Thermo Fisher Scientific, A21235) and 1:200 546-phalloidin (Thermo Fisher Scientific, A22283). Coverslips were mounted on glass slides with ProLong Gold Antifade Mountant (Thermo Fisher Scientific, P36930), which contains 4',6-diamidino-2-phenylindole (DAPI). Immunofluorescence images were taken with a Nikon TE2000 microscope fitted with a 60x oil immersion lens.

Quantification of focal adhesions and cell shape

All image analyses were performed using ImageJ (NIH) (218–220). Cell area and aspect ratio were quantified by manually tracing cell borders in the phalloidin channel. To quantify focal adhesion parameters from the vinculin channel, areas of interest were first manually traced around individual cells and image background was subtracted. The local contrast of the image was improved by the CLAHE plugin (Contrast Limited Adaptive Histogram Equalization) and the Laplacian of Gauss (LoG3D) plugin was used to smooth the image and suppress noise (220). Particle counts and shape descriptors were then taken from thresholded images. Background was subtracted from representative images for display pruposes.

Cell migration

Cells were cultured in appropriate concentrations of doxycyline for 2 days to induce expression of the CA-smMLCK construct. To increase the number of isolated cells for analysis, cells were re-seeded at approximately 4000 cells/cm^2 the day before analysis onto glass wells coated with fibronectin as described above. Live phase contrast imaging was performed at 37°C and 5% CO_2 with a TE2000-E2 or a Ti-E microscope fitted with a motorized stage and a 10X objective. Images were taken every 15 minutes for at least 6 hours. Cell tracks of 24 frames were traced using ImageJ's Manual Tracking plug-in (218). The x-y position of the cell center was used to calculate cell speed, defined here as the displacement of the cell over the observed time interval, and persistence, defined here as the end-to-end net distance traveled divided by the total distance travelled during the observed time interval.

Cell proliferation

Cells were seeded at 10,000 cells/cm^2 and cultured in DMSO or 20 μM ML7 for two days, then fixed and stained as described above, with the following antibodies and dilutions: 1:200 anti-KI67 (Agilent, GA62661-2), 1:200 647-anti-rabbit (Thermo Fisher Scientific A-21245), 20 μg/ml DAPI. Whole-well immunofluorescence images were taken with a Nikon TE2000 microscope or a Nikon Ti-E microscope equipped with a 4X objective. Background was subtracted from the images, and the number of particles in the Ki67 channel was divided by the number of particles in

the DAPI channel to quantify the fraction of cells actively proliferating. Three to six wells were analyzed per experiment and the experiment was conducted twice independently.

Statistical analysis

Statistical analysis and graphing were performed in R. Data normality was assessed by plotting histograms and by conducting a Shapiro-Wilks Normality Test (with $p < 0.1$ indicating that the dataset cannot be assumed to be normally distributed). All experiments were conducted independently at least three times unless otherwise stated, with experiments deemed independent if cells were seeded on different days and assays were conducted on different days.

Figures & Figure Legends

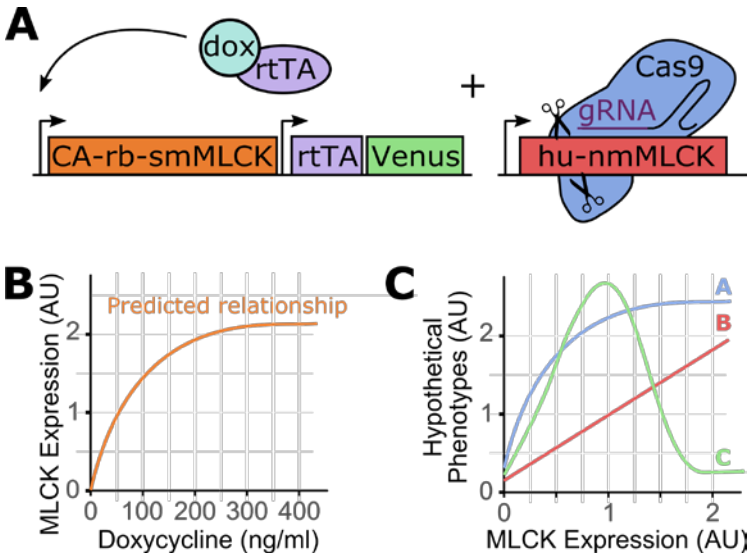

Figure 3.1: Proposed combined conditional expression/endogenous knockout genetic engineering strategy in a human cell line. **(A)** Schematics of pSLIK system, which constitutively expresses a reverse tet transactivator (rtTA) that activates expression of constitutively active rabbit smooth muscle MLCK (CA-rb-smMLCK, CA-smMLCK) upon binding to doxycycline (dox), and of CRISPR/Cas9-mediated knockout, designed to target the human version of MLCK and not the rabbit exogenous version. **(B)** The proposed system would allow total MLCK expression to be controlled from zero to supraphysiological levels by modulation of doxycycline in the cell culture media. **(C)** By measuring mechanobiological phenotypes at varying levels of MLCK expression, the relationship between MLCK expression and phenotypes can be quantitatively explored.

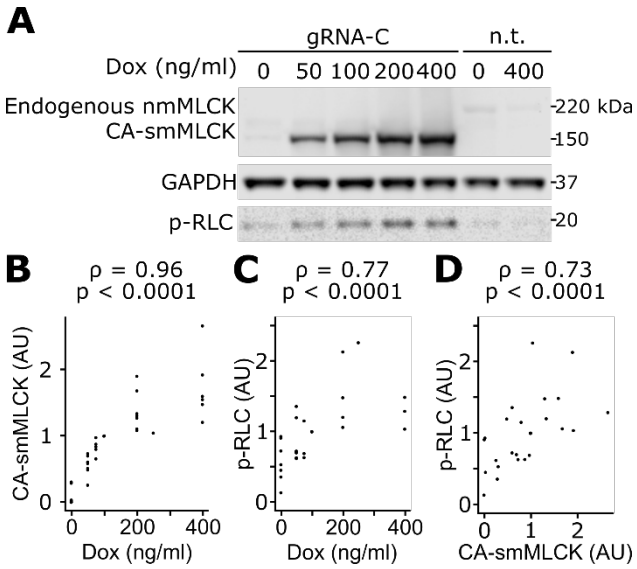

Figure 3.2: Validation of knockout + inducible strategy. **(A)** Representative western blot showing endogenous nmMLCK, CA-smMLCK, GAPDH and p-RLC as functions of doxycycline (Dox) for clonally selected cells receiving the targeting gRNA ("gRNA-C") and for cells receiving a non-targeting gRNA ("n.t."). MLCK was probed using mouse anti-MLCK (Sigma M7905). **(B)** Quantification of CA-smMLCK band-intensity in gRNA-C cells, normalized first to GAPDH and then to the intensity of the normalized CA-smMLCK band for the 100 ng/ml condition. (n = 8 total blots.) **(C)** Quantification of p-RLC band intensity in gRNA-C cells, normalized first to GAPDH and then to the intensity of the normalized p-RLC band for the 100 ng/ml condition. (n = 7 total blots.) **(D)** Replotting of (B-C) to show relationship of p-RLC as a function of CA-smMLCK. Statistical parameters shown for (B-D) represent the Spearman's rank correlation coefficient (ρ) and p value.

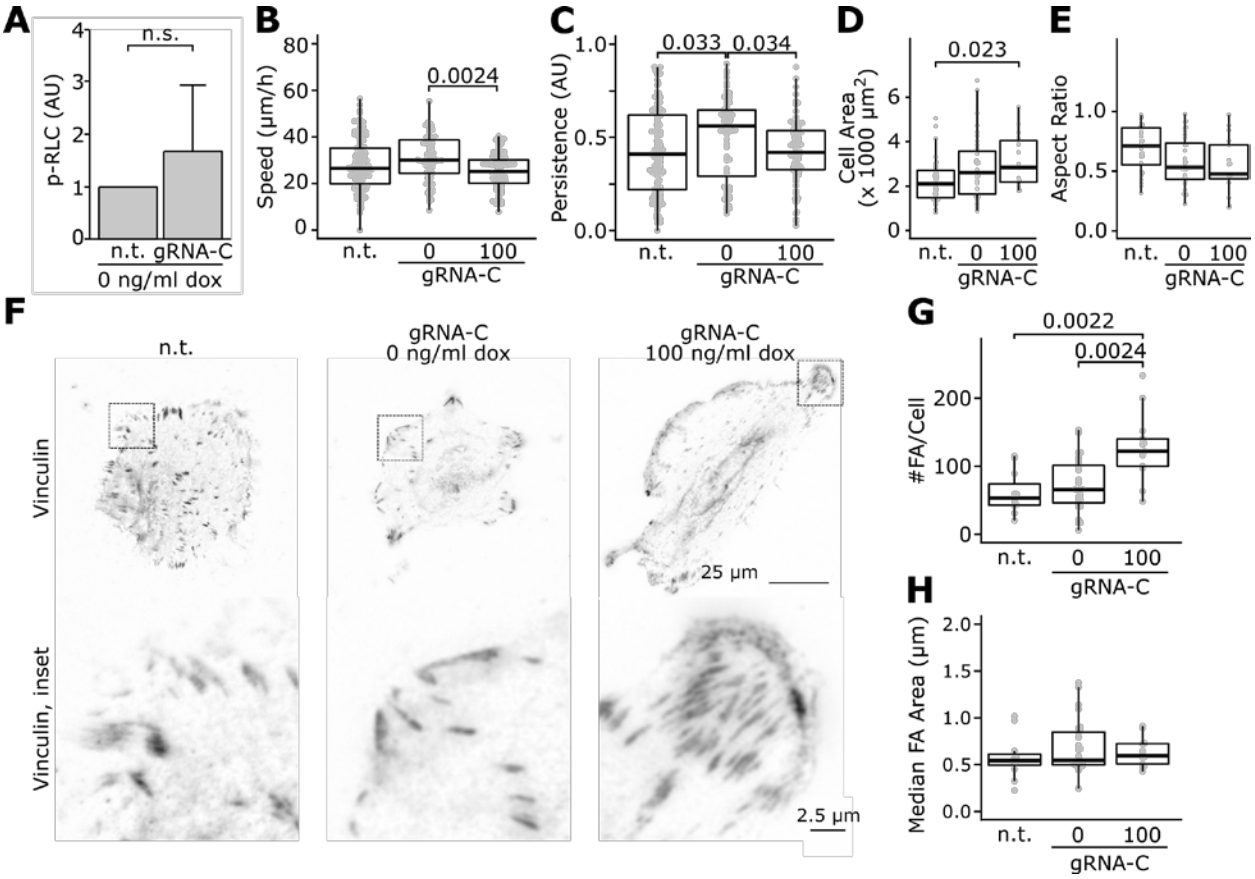

Figure 3.3: Non-muscle MLCK knockout does not influence tested mechanobiological phenotypes that are regulated by CA-smMLCK. **(A)** Quantification of western blots probed for p-RLC, with gRNA-C band intensities normalized first to within-sample GAPDH intensity and then to the within-experiment normalized intensity for the non-targeting condition. Bar shows mean intensity, with error bar indicating standard deviation. Means are not significantly different according to a t-test (p = 0.15, n = 9). **(B)** Migration speed and **(C)** persistence of n.t. cells and gRNA-C cells cultured in 0 or 100 ng/ml doxycycline (n = 116, 68, 82 cells per condition, respectively from left to right). **(D)** Quantification of cell area and **(E)** cell aspect ratio (n = 33, 32, 17 cells respectively from left to right). **(F)** Representative images for cells stained with vinculin (top row) with details enlarged to show focal adhesion size and density (bottom row). **(G)** Quantification of number of vinculin-positive focal adhesions per cell **(H)** and median area of vinculin-positive focal adhesions per cell (n = 11, 28, 13 cells per condition, respectively from left to right). In (B-E, G-H), numbers above horizontal bars indicate adjusted p-value shown, calculated by a Kruskal-Wallis one-way analysis of variance followed by a post hoc Kruskal Dunn test with Holm's method for adjusting for multiple comparisons.

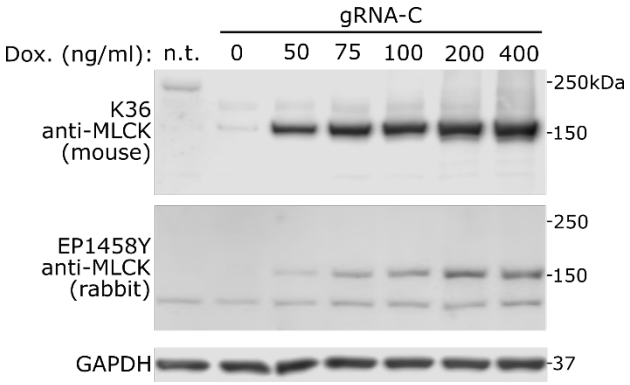

Figure 3.4: Antibodies reveal discrepancies in MLCK isoform expression. The K36 monoclonal anti-MLCK antibody (produced in mouse, purchased from Sigma-Aldrich) detects an endogenous protein at approximately 220 kDa as well as the exogenous CA-smMLCK construct. The EP1458Y monoclonal antibody (produced in rabbit, purchased from Abcam) recognizes an endogenous protein at 130 kDa, as well as the CA-smMLCK construct.

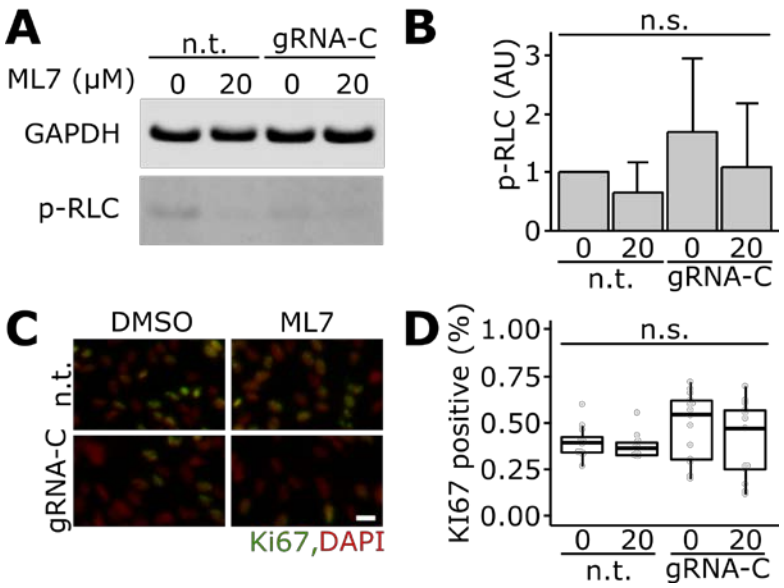

Figure 3.5: Pharmacological inhibition of MLCK with ML7 does not impact phosphorylation of RLC or proliferation. **(A)** Representative western blot and **(B)** quantification for p-RLC, with band intensities normalized first to within-sample GAPDH intensity and then to the within-experiment normalized intensity for the non-targeting condition cultured in DMSO. Bar shows mean intensity, with error bar indicating standard deviation. Means are not significantly different, according to a one-way ANOVA (p = 0.17, n = 6). **(C)** Representative images (scale bar indicates 25 μm) and **(D)** quantification of Ki67 immunostaining. Distributions were not significantly distinct, according to a Kruskal-Wallis rank sum test (p = 0.29, n = 17, 13, 13, 12 technical replicates collected from two independent experiments, respectively from left to right).

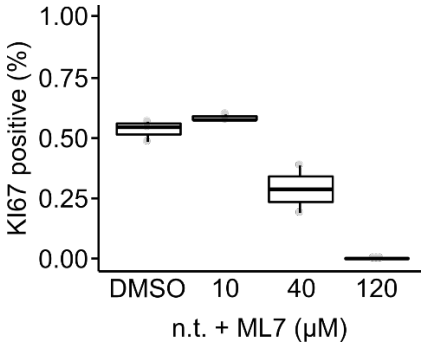

Figure 3.6: ML7 impacts cell viability at very high concentrations. Data is collected from 1 independent experiment with n = 3, 2, 2, 3 technical replicates respectively from left to right.

Chapter 4:
Transcriptomic analysis reveals that BMP4 sensitizes glioblastoma tumor-initiating cells to mechanical cues

Jasmine H. Hughes[1,3], Jeanette M. Ewy[2,3], Sophie Y. Wong[1,3], Sanjay Kumar[3,4*]

[1]UC Berkeley - UCSF Graduate Program in Bioengineering,
[2]Department of Molecular and Cell Biology,
[3]Department of Bioengineering,
[4]Department of Chemical and Biomolecular Engineering, University of California, Berkeley, Berkeley, CA.
* To whom correspondence should be addressed.

ABSTRACT

The poor prognosis of glioblastoma (GBM) is associated with a highly invasive stem-like subpopulation of tumor-initiating cells (TICs) that drive recurrence and whose differentiated progeny contribute to intra-tumoral heterogeneity. We and others have shown that undifferentiated TICs are more capable of escaping microenvironmental mechanical restrictions on invasive motility than their more differentiated progeny. However, comparatively little is known about the molecular basis of the relationship between TIC differentiation and mechanotransduction, limiting therapeutic development of this finding. Here we explore the relationship between morphogen-induced differentiation and mechanotransduction through a combination of whole-genome mRNA sequencing, transcriptional analysis, and cell culture studies. We show that TIC differentiation induced by bone morphogenetic protein 4 (BMP4) suppresses expression of proteins relevant to extracellular matrix signaling and sensitizes TIC spreading and nuclear translocation of canonical mechanotransductive signals to matrix stiffness. Moreover, our findings point towards a previously unappreciated connection between BMP4-induced differentiation, mechanotransduction, and metabolic function, with inhibition of oxidative phosphorylation influencing the ability of cells to spread in a stiffness- and differentiation state-dependent manner. Our work integrates bioinformatic analysis with targeted molecular measurements and perturbations to yield new insight into how morphogen-induced differentiation influences how GBM TICs process mechanical inputs.

Introduction

Glioblastoma (GBM) is the most common and most lethal primary brain cancer. Difficulty in treating this disease has been attributed to a rare but important subpopulation of cells that evade chemotherapeutic treatment, diffusely invade the surrounding tissue, and establish secondary tumors (221–223). These tumor-initiating cells (TICs) share characteristics with neural stem cells (NSCs) in that they self-renew, express high levels of common molecular markers (e.g., SOX2, nestin), and are isolated from tissue by neurosphere suspension culture (224, 225). Like NSCs, GBM TICs are multipotent, differentiating in response to morphogens to produce cells expressing neural, oligodendrocytic and astrocytic markers. Through the process of self-renewal and differentiation, TICs and their progeny establish the heterogenous cell populations that make up the bulk of the tumor (226–228). Indeed, GBMs frequently arise in brain regions associated with adult NSC populations, suggesting that many GBMs may originate from NSCs that have acquired oncogenic mutations (228–230).

Mechanical and biophysical cues have become increasingly accepted as important factors in tumor progression and metastasis (2, 231) and in stem cell self-renewal (232, 233). In recent years, attention has turned to how these mechanobiological cues govern TIC self-renewal, invasion and tumor-initiating capacity (234–237). Interestingly, in contrast to the vast majority of cell types, some GBM TICs show reduced sensitivity to mechanical cues. For instance, rather than showing the characteristic rounded cell morphologies and reduced migration speeds on soft substrates, many TICs are able to spread and migrate equally well on a wide range of substrate stiffnesses. Furthermore, this lack of mechanosensitivity is associated with increased invasive potential (166, 238, 239).

There is accumulating evidence that TIC stem-like state, mechanical signaling and invasive capacity are closely intertwined. For example, mechanical cues influence TIC self-renewing capacity and stem marker expression (240, 241). Several integrins, which directly link cells to the surrounding extracellular matrix (ECM), have been identified as overexpressed in GBM TICs and have been demonstrated to play key roles in invasion and self-renewal (239, 242–244). Stem-like breast cancer cells showed increased myosin IIB expression compared to genetically-matched differentiated breast cancer cells, allowing improved invasion through small pores (245). Similarly, GBM TICs show upregulated Rho GTPase activity compared to less invasive genetically matched bulk tumor cells (239). Invasive capacity in GBM cells is correlated with enriched expression of markers commonly associated with stem cells, including SOX2 (246), CD44 (247) and nestin (99).

In a recent study, we showed that patient-derived GBM TICs demonstrate surprisingly little sensitivity to ECM mechanical cues (166). These cells do not exhibit the rounded morphologies and inhibited migration speeds seen in continuous GBM cell lines cultured on very soft substrates (248). However, constitutively activating actomyosin contractile forces sensitized these cells to matrix stiffness, and greatly inhibited their ability to invade *in vitro* and *in vivo*. These responses could also be partially restored by treatment with bone morphogenetic protein 4 (BMP4), which restored sensitivity of cell spreading to ECM stiffness. More broadly, BMP proteins have arisen as morphogens of interest in GBM TICs due to the crucial instructive role they play in the adult NSC niche (227, 249). BMP4 has been found to inhibit tumor-initiating capacity as well as induce

expression of differentiation markers in TICs (227).Thus, an important open question raised by our study is the molecular basis of the relationship between lack of sensitivity to ECM mechanical cues and morphogen-induced differentiation processes.

In this report, we investigate connections between stemness and mechanosensitivity in GBM TICs by using a combination of RNA sequencing, bioinformatics analysis, and cell culture studies. While changes in ECM stiffness intrinsically alter expression of a relatively limited subset of genes, this number is greatly broadened by treatment with BMP4. Interestingly, the set of mechanically-regulated genes is strongly enriched in genes relevant to ribosome function and oxidative phosphorylation. Throughout, we validate that stiffness- and BMP4-modulated transcripts are also enriched at the level of protein expression. We also show for the first time that inhibition of oxidative phosphorylation alters cell spreading in a differentiation- and stiffness-dependent manner. To our knowledge, this is the first report of mechanical regulation of metabolic machinery in GBM TICs, and sheds insight on how the microenvironment could regulate cellular responses to therapeutics that target energy production.

Results

BMP4 sensitizes cell spreading and nuclear translocation of mechanotransductive signaling factors to matrix stiffness

As described earlier, we had previously shown that the spreading and invasion of GBM TICs are comparatively insensitive to stiffness cues, with BMP4 differentiation inducing stiffness sensitivity. Since publication of that study, we have developed an improved method of conjugating laminin and other ECM proteins to PA gel surfaces using 2PCA-based N-terminal conjugation rather than the traditional sulfo-SANPAH conjugation via side-chain lysines (191). To benchmark our new protocol against our earlier result, we seeded TICs cultured in growth factor-enriched self-renewal medium (+GF) or BMP4-supplemented differentiation medium (+BMP4) on 2PCA-confugated soft or stiff polyacrylamide gels. Consistent with our published results, TICs cultured in growth factor-enriched media did not show a difference in cell spreading area between soft gels and stiff gels (p = 0.96). BMP4-treated cells were significantly smaller than control cells, and furthermore showed an 18% reduction in median cell area on soft gels compared to stiff gels (Figure 4.1A-B).

Having reestablished our earlier finding, we next asked whether these morphological changes were accompanied by activation of signals canonically associated with mechanotransduction. The transcriptional coactivator TAZ (transcriptional coactivator with PDZ-binding motif, also known as WW domain-containing transcription regulator protein 1, or WWTR1), has been identified as a key mediator of mechanotransduction. Specifically, matrix stiffening induces TAZ to localize from the cytoplasm to the nucleus, where it engages specific cofactors to modulate gene expression (66, 250). We therefore hypothesized that BMP4 treatment may enhance nuclear mobilization of TAZ on stiff ECMs. Indeed, we found that there was no statistically significant difference between control cells grown on either soft or stiff gels or BMP4-treated cells on soft gels, but that BMP4-treated cells on stiff gels showed a 22% increase in median nuclear localization of TAZ compared to BMP4-treated cells on stiff gels (Figure 4.1C-D). Thus, BMP4-mediated differentiation

sensitizes GBM TICs to matrix stiffness cues at the level of cell morphology and activation of mechanotransductive signals.

BMP4 influences a broader subset of transcripts than matrix stiffness and increases the number of stiffness-sensitive genes

The results above strongly suggest that BMP4-mediated signaling and mechanotransductive signaling interact in complex ways. To gain a more comprehensive molecular picture of mechanisms that might define these connections, we applied whole-genome RNA sequencing to TICs exposed to soft or stiff substrates, with or without BMP4 treatment. BMP4 elicited a pronounced effect on the transcriptome, consistent with the pro-differentiation effect of BMP4 on TICs (Figure 4.2A, left two panels). BMP4 treatment altered expression (FDR < 0.05) of 4473 named genes on soft matrices (downregulated 2469, upregulated 2003) and 3333 named genes on stiff matrices (1850 downregulated, 1428 upregulated) in comparison to stiffness-matched GF-treated controls. Most of the genes influenced by BMP4 treatment were common to cells on both matrix stiffnesses (2886 genes in common), although 447 genes and 1587 genes were unique to cells differentiated on stiff gels and soft gels respectively (Figure 4.2B).

In comparison with BMP4 treatment, substrate stiffness impacted the transcriptome to a relatively modest degree (Figure 4.2A, right two panels; Figure 4.2B). Just 171 genes were differentially expressed across soft gels and stiff gels for cells cultured in GF-enriched media (166 genes upregulated and 68 genes downregulated by high stiffness, FDR < 0.05). For BMP4-treated cells, this figure was higher by three-fold; 466 genes were differentially expressed between cells grown on soft gels versus stiff gels (354 genes upregulated and 268 genes downregulated by high stiffness, FDR < 0.05). Only a small subset of these genes (35 genes; Figure 4.2A, right two panels; Figure 4.2C) were significantly differentially expressed (FDR < 0.05) at different substrate stiffness for both GF-treated and BMP4-treated cells. These 35 common genes were largely expressed at higher levels on stiff substrates compared to soft, although two genes (AGT and EMP1) showed a switch in the directionality of their mechanosensitivity (Figure 4.2D).

BMP4 treatment alters the transcriptome to a much larger extent than a change in stiffness does. This finding is consistent with the broad phenotypic changes associated with differentiation, including alterations in cell morphology, marker expression, and functional maturation. Our transcriptomic findings are also consistent with three observations from our earlier work (166): First, the distribution of marker-positive progeny in response to BMP4 treatment does not depend strongly on matrix stiffness, implying that stiffness does not bias or instruct differentiation. Second, undifferentiated TICs are largely insensitive to mechanical cues (166). Third, BMP4 sensitizes these cells to substrate stiffness.

Pathway analysis reveals BMP4 downregulates signaling associated with ECM interaction

To better understand how BMP4 alters gene expression, we next mined our RNAseq data to identify signaling systems that might be preferentially impacted by BMP4 expression compared to stiffness-matched controls. We found that BMP4 significantly upregulated genes associated with axon guidance, such as ephrins, ephrin receptors, and several semaphorins (Figure 4.3A, Figure 4.4). We also found that BMP4 suppressed PI3K-Akt signaling, including downregulation

of MAP2K1 (Mek1) (Figure 4.3). Both findings are consistent with BMP4's observed pro-differentiation and anti-proliferative effects on TICs (227). BMP4 treatment also downregulated genes associated with ECM-receptor interactions, focal adhesions and proteoglycans, such as many integrin subunits, zyxin, paxillin and CD44 (Figure 4.3, Figure 4.4).

Our findings support at a more systems-level past reports that identified integrins, RhoGTPases and myosin II as distinguishing more invasive or more stem-like TICs from less invasive or more differentiated TICs (239, 242–245). BMP4 treatment had a pronounced inhibitory effect on the expression of the actomyosin force generation activators myosin light chain 12A (MYL12A) and ROCK2, which is somewhat surprising given that we had shown that activation of the actomyosin contractility sensitized this TIC line to mechanical cues. However, mechanotransduction is also strongly regulated by posttranslational modification, subcellular localization, and other factors, which may collectively render the relationship between gene expression and signaling activity markedly nonlinear (195, 198).

BMP4 elicits a pro-differentiation effect at the transcriptional level. Several investigators have reported transcriptional or proteomic changes in specific markers in GBM TICs treated with BMP4 or have identified specific markers associated with TIC stemness (227, 251). Consistent with these reports, we found BMP4 upregulated expression of the neural marker βIII tubulin (TUBB3) and the astrocytic marker glial fibrillary acidic protein (GFAP) (Fig 3B). We did not observe an appreciable change in expression of the oligodendrocyte marker galactosylceramidase (GALC), consistent with the findings by Piccirillo and colleagues that this lineage was the least commonly produced by BMP4-treated TICs (227). Of the core four transcription factors that have been reported to drive GBM propagation (251), two (OLIG2, POU3F2) were significantly downregulated by BMP4 treatment, one (SALL2) was upregulated by BMP4 treatment and one (SOX2) was not impacted by BMP4 treatment (and thus excluded from Fig. 3B, along with GALC). A BMP4-dependent increase in SALL2 expression may reflect its somewhat mixed pro-tumorigenic and tumor-suppressive effects (252–254).

Substrate stiffness regulates expression of ribosomal protein and oxidative phosphorylation genes

To determine how substrate stiffness alters the transcriptomic profile of these TICs we next performed pathway analysis on the list of genes differentially expressed (FDR < 0.05) in cells grown on different stiffnesses in either GF-enriched (Figure 4.3C) or BMP4-supplemented (Figure 4.3D) media. To our surprise, changes in substrate stiffness produced similar transcriptomic changes in both BMP4-treated and GF-treated cells. Somewhat unexpectedly, one of these conserved pathways included ribosome proteins and oxidative phosphorylation (OXPHOS). Moreover, deeper inspection of the other gene sets (e.g. Parkinson's Disease, Cardiac Muscle Contraction) reveals that the differentially expressed genes in these sets overlap almost entirely with oxidative phosphorylation (Figure 4.3E, orange). We then examined how single genes within each set change with stiffness in each medium condition (Fig. 3F). Ribosome protein expression is upregulated by both BMP4 treatment and by matrix stiffening (Figure 4.3F, orange points). OXPHOS genes follow a more mixed picture; although BMP4 upregulates a few OXPHOS genes its net effect is to downregulate OXPHOS genes, while stiffness universally upregulates OXPHOS genes (Figure 4.3F, blue points).

Transcriptional response to matrix stiffness cannot be fully explained by canonical mechanotransduction transcription factors

Given that matrix stiffening induces TAZ nuclear translocation (Fig. 1), and given the demonstrated importance of YAP and TAZ in mediating mechanotransduction, we wondered if YAP/TAZ targets might be differentially expressed across different stiffness in our cells. Surprisingly, relatively few previously identified YAP/TAZ targets (66, 255) changed expression as a function of stiffness (Figure 4.3G). Instead, the phenotypically mechano-insensitive stem-like cells showed a significantly (Pearson's χ^2 p value < 0.05) higher proportion of stiffness-altered genes that were targets of YAP/TAZ (9/171) compared to the BMP4-treated cells (8/466). This finding suggests that some other transcription factor(s) are also important in the transcriptomic response of these cells to mechanical cues, either independently or in concert with YAP/TAZ signaling.

Proteomic confirmation of RNA sequencing predictions

To validate our transcriptomic data at the proteomic level, we identified a short list of protein targets that were associated with one or more of the KEGG pathways shown in Figure 4.3 and Figure 4.4 that exhibited a foldchange at the transcriptional level of at least two. We ultimately selected mitogen-activated protein kinase kinase (MAP2k1, also known as MEK1), α-actinin-1 (ACTN1), TAZ and zyxin (ZYX) for their strongly validated roles in mediating mechanotransductive signals (Figure 4.5A). Each of the targets probed showed a significant change in expression in the predicted direction (Figure 4.5B-C). To our knowledge, these findings are the first evidence that these mediators of mechanotransduction alter during BMP4-induced differentiation. Our observation that TAZ decreases in expression after BMP4 treatment is consistent with our finding that YAP/TAZ target genes are not strongly differentially expressed across different substrate stiffnesses in BMP4-treated cells.

Integrin signaling has been previously observed to be upregulated in patient tumor samples compared to normal brain (244). At the transcriptomic level, we observed significant downregulation of integrin expression in response to BMP4 treatment (Figure 4.3A; Figure 4.4F) with the exception of Integrin α_2 (ITGA2), which instead shows a large increase in expression. ITGA2 complexes exclusively with Integrin β_1 (ITGB1) and binds collagen, laminin and E-Cadherin (CDH1) (256). While several integrins have received close attention in the context of GBM cancer stem cells (242, 243), comparatively less is known about ITGA2. Some evidence indicates ITGA2 is lower in breast cancer cells compared to healthy tissue and decreased ITGA2 is associated with increased invasiveness and poorer prognosis (257–259).

Interestingly, we discovered that the α_2 subunit is also upregulated by BMP4 at the transcriptional (Figure 4.5D) and protein level (Figure 4.5E). ITGA2 signal in GF-treated cells was mostly diffusely cytoplasmic. Increased localization of ITGA2 was observed at cell peripheries and at cell-cell contacts in BMP4-treated cells cultured on stiff gels compared to those on soft gels (Figure 4.5F), suggesting ITGA2 may be playing a role in adhesion and mechanotransduction. As previously described, these cells do not exhibit well-defined focal adhesions (166), and we were unable to co-stain ITGA2 with other focal adhesion proteins (not shown).

Inhibition of oxidative phosphorylation impacts cell spreading in a differentiation state- and stiffness-dependent manner

Because of the surprising enrichment of OXPHOS in the genes regulated by stiffness, we wondered if inhibition of this process would alter cell spreading in a stiffness-dependent manner. We treated the cells with 5 μM oligomycin, an ATP synthase inhibitor that prevents conversion of ADP to ATP through OXPHOS (260). Over the course of 30 minutes we observed that GF-treated TICs showed a noticeable retraction of protrusions (Figure 4.6A, white arrows). This change in cell spreading was particularly dramatic for the GF-treated TICs on stiff gels, where some cells became much more rounded and sometimes collapsed into clumps of cells. In contrast, BMP4-treated cells showed lower levels of protrusion retraction and indeed often showed protrusion extension (yellow arrows). Quantification of cell area before and after oligomycin addition (Figure 4.6B) demonstrated that while GF-treated TICs became less spread, the BMP4-treated cells were able to spread in the presence of oligomycin. For the GF-treated TICs, this change in cell area was stiffness-dependent, with the cells on soft gels decreasing in area by a median of 8.7% while the cells on stiff gels decreased in area by a median of 17.8%. This finding is consistent with our RNA sequencing data, in which oxidative phosphorylation was upregulated on stiff substrates. While we had expected to see more of a difference in the BMP4-treated cells, the lack of effect seen may be due to lower metabolic rates. Indeed, this finding is consistent with the BMP4's suppressive effect on PI3K signaling (Figure 4.3A), which is known to influence metabolism and decrease oxygen consumption (261, 262). Together, these results highlight the relationship between differentiation and metabolism, and provides new evidence of the regulation of metabolism by matrix stiffness.

Discussion

Increasing evidence suggests that stem-like GBM TICs show reduced sensitivity to mechanical cues and heightened invasive potential. One facet that remained unclear is how differentiation of TICs alters their ability to sense and respond to their mechanical environment. We show here that BMP4's pro-differentiation effect sensitizes cell spreading and nuclear translocation of TAZ to substrate stiffness. Through RNA sequencing, we discovered that BMP4 down-regulates signaling associated with communication with the ECM. We also found that stiffness cues regulate expression of ribosome proteins and oxidative phosphorylation proteins regardless of differentiation state, but that differentiation triples the number of genes differentially expressed across different matrix stiffnesses. Through inhibition of oxidative phosphorylation, we show that cell spreading depends on oxidative phosphorylation in a stiffness- and differentiation-dependent manner.

The dysregulation of mitochondria and metabolism in cancer has been an area of particular focus, and these efforts have shed considerable light into how mitochondrial signaling regulates proliferation, survival and response to chemotherapy (263). Metabolic pathways may change as stem-like cells differentiate (264). For example, glioma stem cells rely less on glycolysis than more differentiated glioma cells (265). Our RNA sequencing data supports this finding, with BMP4

treatment eliciting a net suppressive effect on genes associated with oxidative phosphorylation. The role that the mechanical microenvironment plays in modulating the function of mitochondria, which are anchored to the cytoskeleton is only beginning to be investigated (266, 267). Recent studies have demonstrated that metabolic parameters can be strongly influenced by ECM physical properties such stiffness and fiber alignment. For example, the ATP:ADP ratio in migrating cells is higher in dense matrices or when cytoskeletal force generation is inhibited, and lower in aligned matrices where migration is facilitated (268). Basal metabolic rates are higher on stiff substrates, and both stiffness and fiber alignment modulate cellular responses to metabolic stress (75). Metabolism also appears to be coupled to forces transmitted through the actin cytoskeleton and through cell-cell adhesions (269, 270). The link between ECM mechanics and transcriptional modulation of mitochondrial function is less clear. We recently showed that actomyosin-mediated YAP/TAZ signaling regulates uncoupled respiration in brown adipose tissue (271). Our transcriptional data further support a role for stiffness in transcriptional regulation of oxidative phosphorylation. While blocking oxidative phosphorylation has been shown to impact cell shape (272), to our knowledge this is the first evidence that stiffness modulates this relationship.

A challenge in studying the differentiation of TICs is their epigenetic plasticity, allowing them to revert to more stem-like states after differentiation by culturing in supraphysiological levels of growth factors (273–276). In particular, there is some evidence that SOX2 mediates this plasticity, with SOX2 knockout inhibiting de-differentiation of GBM cancer stem cells (274) and incomplete chromatin remodeling observed at sites with SOX binding motifs even after differentiation (273). It is therefore interesting that we do not observe changes in SOX2 expression between differentiated and undifferentiated cells. One intriguing question is whether de-differentiated TICs regain mechanosensitivity along with re-entry of the cell cycle.

Although we found that stiffness-induced TAZ localization is heightened in BMP4-treated cells, we were surprised to find there is little overlap between the genes we identify here as mechanically regulated and previously validated YAP/TAZ target genes (66, 255). Also unexpected was the finding that rather than simply amplifying the number of genes that are differentially expressed, BMP4-treatment eliminates the mechanoresponsiveness of some genes while sensitizing other genes to mechanical cues. Together, these findings suggest that mechanical regulation of transcription goes beyond YAP and TAZ, either by the modulation of the activity of these transcription factors by other transcription factors or via additional presently unidentified mechanosensitive transcription factors acting independent of YAP/TAZ.

Overall, our work demonstrates that BMP4's pro-differentiation effect sensitizes GBM TICs to substrate stiffness, and hints towards the importance of the mechanical microenvironment in regulating metabolism and ribosome biogenesis. Since tumors often have different mechanical properties than surrounding tissue (277, 278), this work may help shed light on heterogeneous responses to chemotherapeutics targeting metabolic pathways. In future work, it will be valuable to identify transcription factor interactions that could integrate mechanical signals to regulate genes associated with oxidative phosphorylation.

Acknowledgements

This work used the Vincent J. Coates Genomics Sequencing Laboratory at UC Berkeley, supported by NIH S10 Instrumentation Grants S10RR029668 and S10RR027303. We thank Dr. Mary West of the CIRM/QB3 Shared Stem Cell Facility at UC Berkeley for technical support. Confocal microscopy was performed in the SSCF. We also thank Bob Lesch and Professor Randy Schekman for the use of their Odyssey, and Kelsey Springer for her assistance with rheological measurements. We gratefully acknowledge financial support from the following sources: the Natural Sciences and Engineering Research Council of Canada (NSERC, PGS D 555229 awarded to J.H.H.), the Siebel Scholars program (J.H.H.), the W.M. Keck Foundation (S.K.) and the National Institutes of Health (R01GM122375, R21025017).

Methods

Tumor-initiating cell culture

The L0 patient-derived classical subtype tumor-initiating cells were a kind gift from Professor Brent Reynolds (224) and were further characterized by our lab in a recent publication (166). Cells were cultured in Neurocult (Stem Cell Technologies, 05751) supplemented with 20 ng/m epidermal growth factor (EGF; Peprotech, 236-EG-200) and 10 ng/ml fibroblast growth factor (FGF; R&D Systems 233-FB-025/CF). Under these conditions, TICs grow in suspended neurospheres, which were serially passaged every 5-7 days by dissociation with 0.05% trypsin/ethylenediaminetetraacetic acid for 2 min at 37˚C followed by quenching in trypsin inhibitor. All experiments were conducted with cells passaged fewer than twenty times. For BMP4 treatment, cells were cultured in Neurocult supplemented with 100 ng/ml BMP4 (R&D Systems, 314-BP-010/CF). Control cells were cultured in Neurocult supplemented with 10 ng/ml FGF and 20 ng/ml EGF.

Polyacrylamide gel synthesis

Polyacrylamide (PA) gels of “soft” (100-250 Pa) and “stiff” (40-60 kPa) elastic moduli were synthesized and functionalized with laminin via the cross-linker Sulfo-SANPAH for RNA extraction and functionalized with laminin via 2-pyridinecarboxaldehyde (2PCA) for all other assays as described previously (191). Briefly, acrylamide (A) and N-N’-methylene-bis-acrylamide (B) were mixed at 3%A/0.04%B (soft) and 15%A/1.2%B (stiff) and dissolved oxygen was removed by bubbling with nitrogen gas. For gels functionalized with 2PCA, 2PCA was added directly to the acrylamide/bis solution at a 0.1% mole fraction relative to acrylamide monomer content. The gels were polymerized with ammonium persulfate (Bio-Rad, 10% w/v stock made in ultrapure water, to a final concentration of 0.1%) and tetramethylethylenediamine (Bio-Rad, 0.1% v/v) while sandwiched between a glass coverslip activated with bind-silane (Sigma Aldrich, GE17-1330-01) and a glass slide treated with water repellent (Rain-X). After 30 minutes, the hydrophobic glass slide was removed from the polymerized gels. Gels functionalized with Sulfo-SANPAH were submerged in Sulfo-SANPAH (ThermoFischer Scientific, 22589) for 8 minutes under a UV lamp

and then rinsed twice in PBS. Regardless of functionalization method, gels were then incubated in 0.1 mg/mL laminin (Invitrogen, 23017-015) overnight at 37˚C.

Cell Area Measurements

Cells were seeded at 10,000 cells/cm^2 on PA gels functionalized with laminin via 2PCA and cultured in BMP4- or GF-supplemented media for 2 days. For ATP synthase inhibition, a solution of media and oligomycin (EMD Millipore, 495455) was added to the culture media to a final concentration of 5 μM, and cells were imaged before treatment and 30 minutes after treatment. Phase contrast images were taken with a Nikon TE2000-E2 microscope and the perimeter of the cells were manually traced on ImageJ to calculate the cell area. Cells were excluded from analysis if >5% of the cell perimeter was in contact with another cell.

Immunocytochemistry

Cells were seeded at 10,000 cells/cm^2 on 2PCA-functionalized PA gels and cultured in BMP4- or GF-supplemented media for 7 days. Cells were fixed in 4% paraformaldehyde (PFA; Fisher Scientific, #30525-89-4) in Dulbecco's PBS (Sigma-Aldrich, D1283) for 10 minutes. The samples were treated with 0.1% sodium borohydride (Spectrum Chemical, S1187) for 10 minutes to reduce nonspecific antibody binding with the PA gels, then permeabilized with 0.5% Triton-X100 (EMD Millipore, 9410) for 12 minutes. Samples were blocked with 5% goat serum (GS; Thermo Fisher Scientific, 16210064) for at least 1 hour then incubated overnight in primary antibodies diluted in 1% GS at 4˚C. Samples were then washed in 1% GS and stained in secondary antibodies and 1: 400 DAPI (Sigma-Aldrich, 10236276001) diluted in 1% GS for 1 hr at room temperature. The following antibodies and dilutions were used: 1:100 anti-TAZ clone M2-616 (produced in mouse, BD Biosciences, 560235), 1:100 anti-ITGA2 (produced in mouse, Abcam, ab10800), 1:200 goat anti-mouse Alexa Fluor 647 conjugate (Thermo Fisher Scientific, A21235). Samples were then washed in 1% GS then in PBS. Representative images have background signal subtracted for display purposes.

Nuclear Localization of TAZ

Epifluorescent images of cells probed for TAZ (WWTR1) were taken with a Nikon TE2000-E2 microscope equipped with a 20X objective. Image analysis was performed using ImageJ (NIH). TAZ images were overlaid with DAPI stains and background was subtracted. The DAPI channel was used to create a mask of the nucleus and nuclear intensity of TAZ was divide by the total background-subtracted intensity of TAZ. Nuclear localization is calculated per field of view, with each image containing 5-20 individual cells. Due to the 1-week culture period, cells often overlapped too much to allow segmentation of individual cells.

RNA Sequencing Sample Preparation

Cells were seeded at 20,000 cells/cm^2 on PA gels functionalized with laminin via Sulfo-SANPAH. BMP4-treated cells were cultured for 7 days while untreated cells were cultured for 3 days due to their more rapid growth and arrival at confluence. Cells were lysed with TRIzol reagent (Life Technologies, 15596026) and RNA was extracted using the RNeasy Micro Kit (Qiagen, 74004)

according to the manufacturer's protocol. Duplicate samples were collected in two distinct experiments with cells of separate passage numbers. Total RNA samples were submitted to the University of California, Berkeley QB3 Functional Genomics Laboratory (FGL) for sequencing preparation. Total RNA was checked on a Bioanalyzer (Agilent) for quality, and only high-quality RNA samples (RIN > 8) were used. At the FGL, Oligo $(dT)_{25}$ magnetic beads (Thermofisher) were used to enrich mRNA. The treated RNAs were rechecked on Bioanalyzer for integrity. The Library preparation for Illumina sequencing was done on the Apollo 324^{TM} with PrepXTM RNA-Seq Library Preparation Kits (WaferGen Biosystems, Fremont, CA) according to the manufacturer's recommendation. Libraries were then visualized again on the Bioanalyzer and transferred to the UC Berkeley-QB3 Vincent J. Coates Genomics Sequencing Laboratory where they were qualified by real-time PCR on a Roche Lightcycler 480II (Roche Applied Biosciences, Indianapolis, IN) with Kapa Biosystems Illumina quantification reagents (Kapa biosystems, Wilbur, MA). Libraries were then pooled in equimolar ratios and sequenced on the Illumina HiSeq2000 in High Output Mode using v3 single-end 50 base-pair chemistry (Illumina Inc., San Diego, CA).

RNA Sequencing Analysis

Read quality was assessed using FastQC (279) and Phred scores were found to be greater than 28. Low quality ends and adaptor sequences were removed using the FASTQ Trimmer and FASTQ Clipper. Sequences were aligned to the human reference genome GRCh38 using TopHat2 (280) and differential expression analysis was conducted with the Cufflinks package (281).

Pathway Enrichment Analysis

DAVID Bioinformatics Resources version 6.8 (2016) (282) was queried with gene lists of interest to determine Kyoto Encyclopedia of Genes and Genome (KEGG) pathway enrichment. For Figure 4.3A, the two gene lists were the sets of named genes significantly (FDR < 0.05) upregulated (712 genes) or downregulated (608 genes) by BMP4 by a factor of $2^{1.5}$ or higher for stiffness-matched comparisons. For Figure 4.3C and 4.3D, the gene lists were the set of 171 or 466 named genes significantly differentially expressed (FDR <0.05) between the two matrix stiffnesses for GF-treated cells or BMP4-treated cells, respectively.

Western Blots

Cells were lysed in 1% protease inhibitor cocktail (Cell Signaling Technologies, #5871S), 1% phosphatase inhibitor (EMD Millipore, 524624), 4.1 μg/ml sodium molybdate and 1.4 μg/ml sodium fluoride in radioimmunoprecipitation assay (RIPA) buffer (Sigma-Aldrich, R0278). Protein concentration was measured by bicinchonic acid (BCA) assay (Thermo Fisher Scientific, 23228) according to manufacturer's specifications and samples were brought to equal protein concentrations with additional lysis buffer. Lysates were mixed with LDS (Thermo Fisher Scientific, NP0007) and reducing agent (Life Technologies, NP0009) and heated at 95˚C for 5 minutes. Samples were run on 4-12% Bis-Tris gels (Invitrogen, NP0323) in MOPS buffer (Life Technologies, NP001) at 170 V for 65 minutes and transferred onto nitrocellulose membranes (LI-COR, 926-31092) at 50 V for 150 minutes in 10% methanol and transfer buffer (NP0006). Membranes were blocked for at least 1 hour in blocking buffer (LI-COR, 927), then primary antibodies were added and the membranes were incubated overnight at 4˚C. Membranes were

washed in tris-buffered saline and Tween-20 (TBST), incubated in secondary antibodies diluted in blocking buffer, washed in TBST and imaged on an Odyssey system. The following antibodies were used: anti-cofilin clone D3F9 (Cell Signaling Technologies, 5175), anti-α-actinin-1 (Sigma-Aldrich, A5044), anti-MAP2K1 (Cell Signaling Technologies, 9124), anti-TAZ clone M2-616 (BD Biosciences, 560235), anti-zyxin (Abcam, ab58210), anti-ITGA2 (Abcam, ab133557 or ab10800), IRDye 680RD goat anti-rabbit (LI-COR, 925-68071), IRDye 800RD goat anti-mouse (LI-COR, 925-32210). Bands were quantified using ImageJ's standard gel analyzer tool, with background signal subtracted.

Statistical Analysis

For the RNA sequencing data, statistical analysis was performed as described above. All other analyses and all graphing were performed in R. Data normality was assessed with the Shapiro-Wilk Normality Test, and datasets where $p < 0.1$ were assessed using non-parametric tests as noted in the figure legends. Experiments were performed independently at least thrice, except for RNA sequencing samples, which were collected in duplicate only. Experiments were deemed independent if the gels were made on different days, the cells were passaged and seeded on different days and the assay was conducted on different days.

Figures & Figure Legends

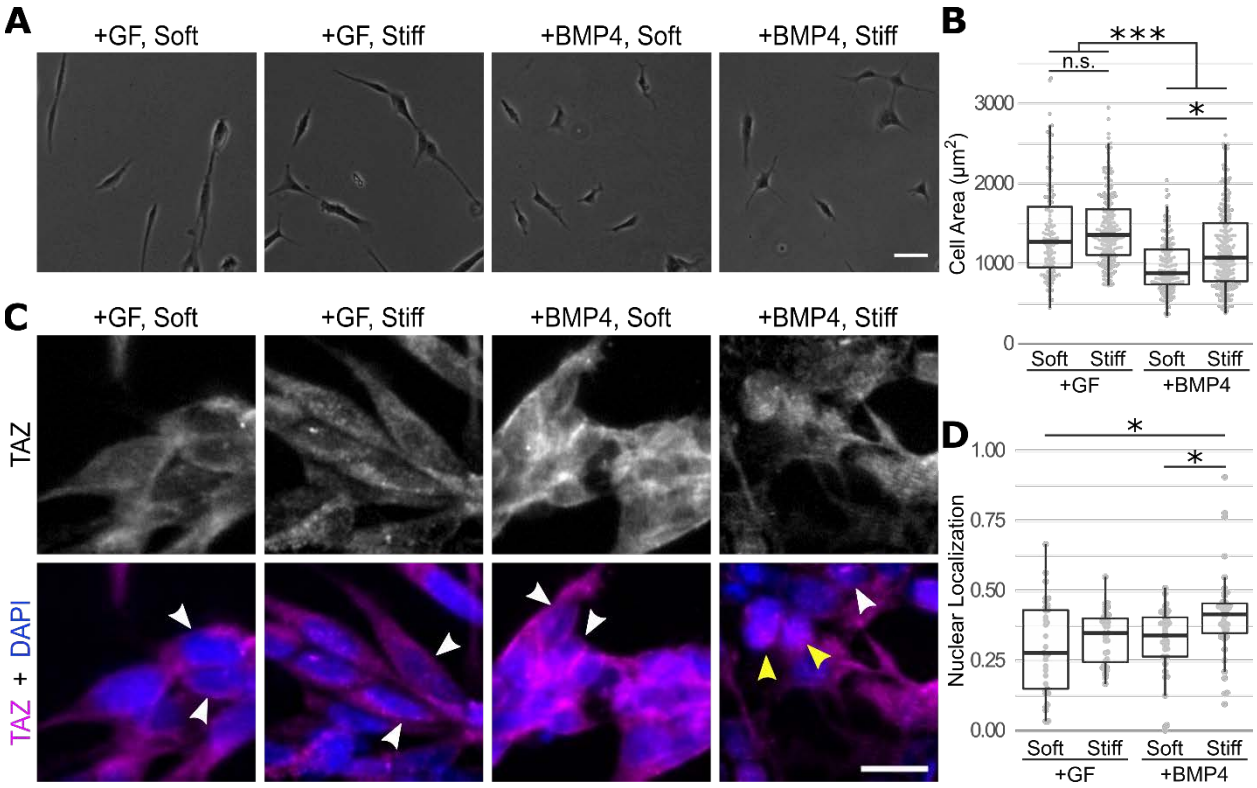

Figure 4.1: BMP4-treatment sensitizes cell spreading and TAZ (WWTR1) localization to substrate stiffness. (A) Representative phase-contrast images of cells grown in growth factor-supplemented (GF) or BMP4-supplemented (BMP4) media on soft (200 Pa) or stiff (40 kPa) ECMs. Scale bar indicates 50 μm. (B) Quantification of cell area of cells cultured in GF- or BMP4-supplemented media on soft or stiff gels (n = 134, 207, 156, 232 respectively from left to right, collected from three independent experiments for each condition). Asterisks indicate significance as calculated with a Kruskal-Wallis one-way analysis of variance followed by a posthoc Kruskal-Dunn test with Holm's method for adjusting for multiple comparisons: * $p_{adj} < 0.05$, *** $p_{adj} < 0.001$, n.s. $p_{adj} > 0.05$. (C) Representative images of cells grown in GF- or BMP4-supplemented media on soft (200 kPa) or stiff (40 kPa) gels stained for TAZ (WWTR1). Top row: TAZ channel. Bottom row: TAZ (magenta) merged with DAPI (blue). Scale bar indicates 5 μm. Arrows indicate cells with particularly prominent TAZ exclusion from (white arrows) or localization to (yellow arrows) the nucleus. (D) Quantification of immunofluorescence intensity of nuclear TAZ normalized to total TAZ intensity per field of view (n = 43, 48, 61 and 61 images respectively from left to right, collected from three independent experiments for each condition). Asterisks indicate significance as calculated by a Kruskal-Wallis one-way analysis of variance followed by a posthoc Kruskal-Dunn test with Holm's method for adjusting for multiple comparisons, : * $p_{adj} < 0.05$.

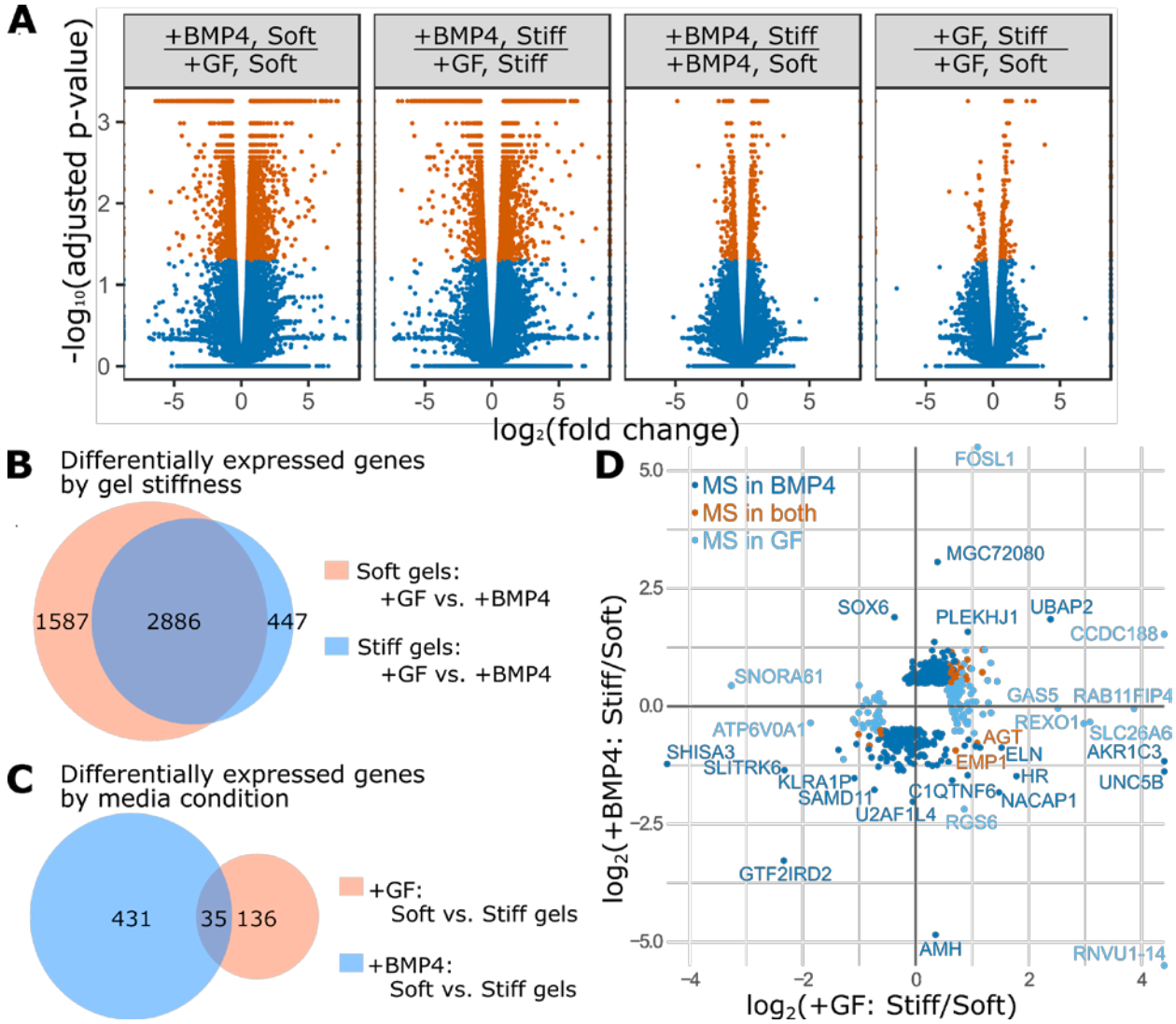

Figure 4.2: Initial analysis of RNA sequencing results. (A) Volcano plots of false discovery rate (FDR) adjusted p-value versus fold-change for each comparison, with significantly differentially expressed (FDR < 0.05) genes highlighted in orange. From left to right: BMP4-treated cells versus growth factor (GF)-treated cells on stiff (40-60 kPa) gels, BMP4-treated cells versus GF-treated cells on soft (0.1-0.25 kPa) gels, BMP4-treated cells on stiff versus soft gels, GF-treated cells on stiff versus soft gels. (B) Breakdown of number of genes significantly (FDR < 0.05) influenced by BMP4 treatment by relationship to substrate stiffness. (C) Breakdown of mechanosensitive genes, defined here as genes that are significantly differentially expressed (FDR < 0.05) on soft versus stiff gels. (D) Fold-change of mechanosensitive (MS) genes for BMP4-treated cells versus GF-treated cells, coded by whether they are significantly differentially expressed (FDR < 0.05) in both media conditions, or only significantly differentially expressed in one of the treatment conditions. Gene names are shown for genes that show mechanosensitivity in either treatment condition with a fold change of at least $2^{1.5}$ and for the two genes that change their direction of mechanosensitivity.

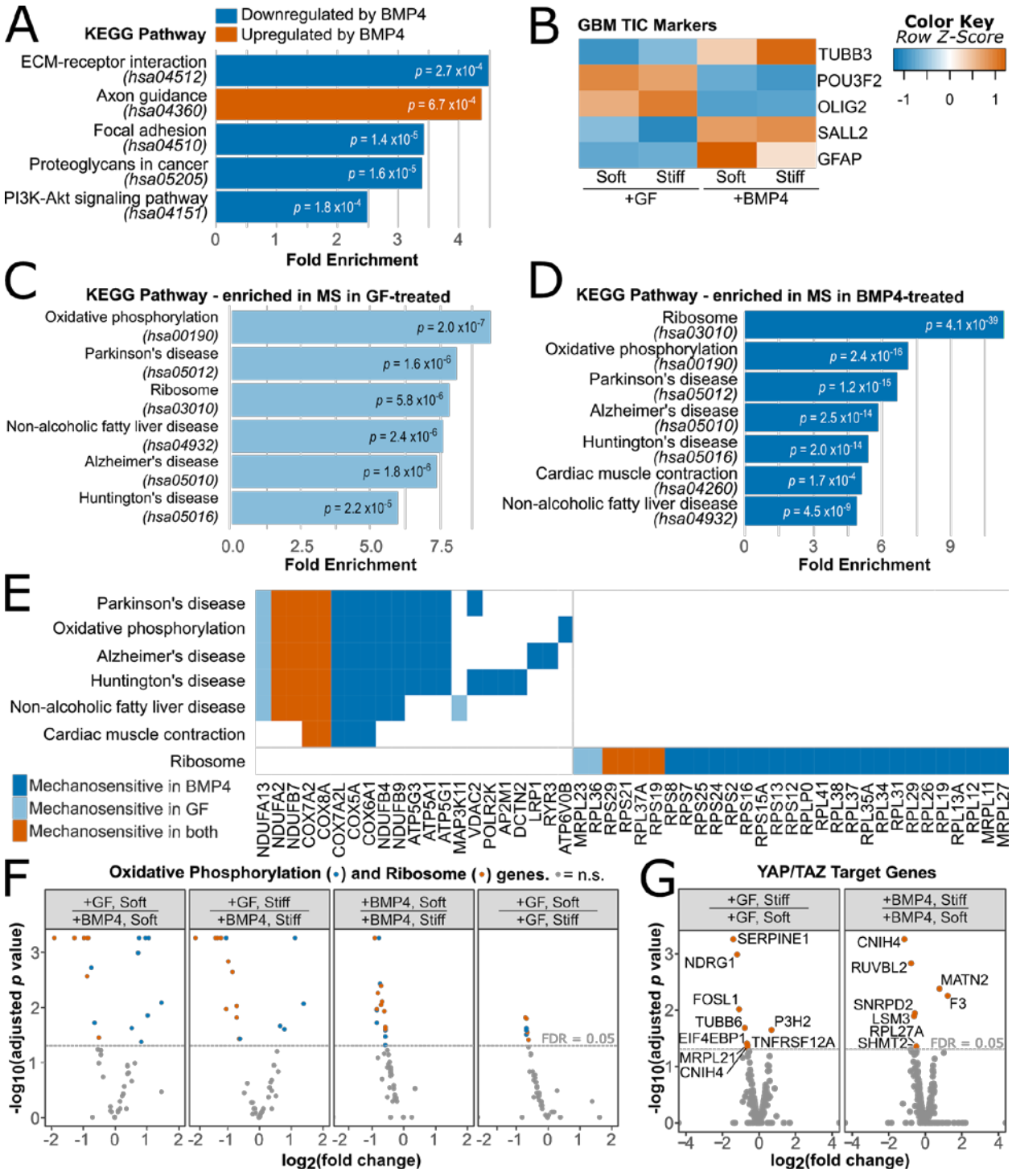

Figure 4.3: Pathway analysis shows BMP4 signaling downregulates ECM communication and upregulates neural markers while stiffness cues influence ribosome proteins and oxidative phosphorylation genes. **(A)** KEGG pathway enrichment analysis for genes that are differentially expressed (FDR < 0.05) with a fold change of at least $2^{1.5}$ in response to BMP4 treatment for cells grown on either stiff or soft gels. The displayed *p* values are adjusted according to Benjamini, and only pathways with Benjamini $p < 0.001$ and with a fold enrichment > 2 are shown. **(B)** Heat map

analysis showing genes associated with neural stem cell differentiation and GBM cancer stemness for which BMP4 significantly (FDR < 0.05) impacted transcription for cells grown on at least one of the two stiffnesses studied. Genes that were run through this analysis but excluded from this plot due to lack of significance were: SOX2, GALC. Rows are clustered based on the mean gene count across each row, and values are then scaled to have a mean of zero and a standard deviation of one before the color value is assigned to each cell. **(C-D)** KEGG pathway enrichment analysis for genes that are differentially expressed (FDR < 0.05) in response to differences in substrate stiffness for cells cultured in **(C)** GF-enriched media or **(D)** BMP4-supplemented media. The displayed *p* values are adjusted according to Benjamini, and all pathways with Benjamini $p < 0.001$ and with a fold enrichment > 2 are plotted. **(E)** Stiffness-regulated genes belonging to the pathways identified in (C-D) color-coded by the conditions under which they are mechanosensitive to demonstrate degree of overlap. **(F)** Volcano plots for genes in the KEGG pathways hsa03010: Ribosomes and hsa:00190 Oxidative phosphorylation. **(G)** Volcano plots for YAP/TAZ targets as identified previously (66, 255), with gene names shown for significantly differentially expressed genes.

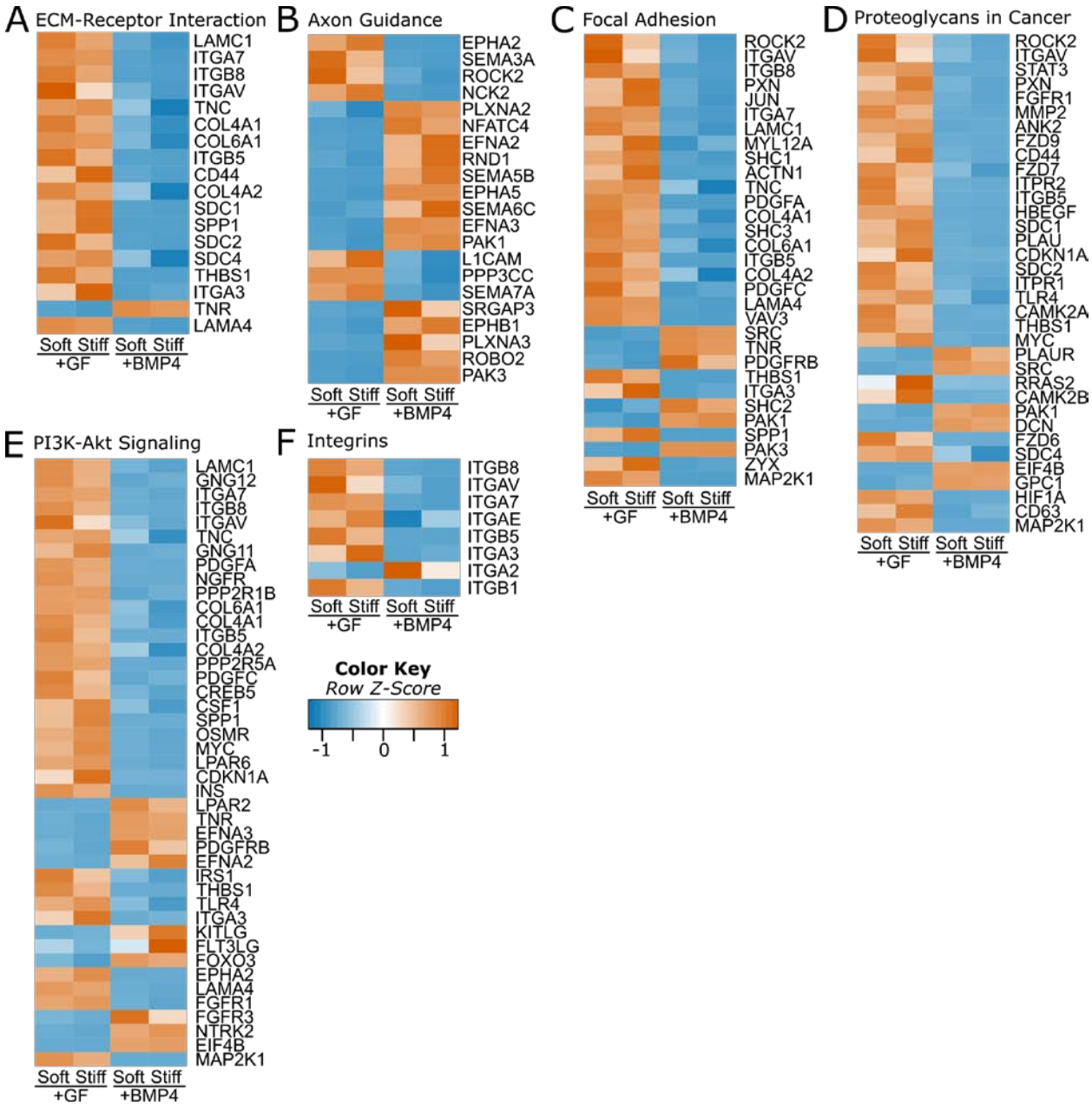

Figure 4.4: Gene expression changes by signaling pathway (shown in Fig 3A) or protein family. Heat map showing significantly differentially expressed genes (FDR < 0.05) with fold changes of at least $2^{1.3}$ for at least one of the comparisons for **(A)** ECM-receptor interaction (hsa04512), **(B)** Axon guidance (hsa04360), **(C)** Focal adhesions (hsa04510), **(D)** Proteoglycans in cancer (hsa05205), **(E)** PI3K-Akt signaling pathway (hsa04151). **(F)** Heat map showing significantly differentially expressed genes (FDR < 0.05) for at least one of the comparisons for integrin subunits.

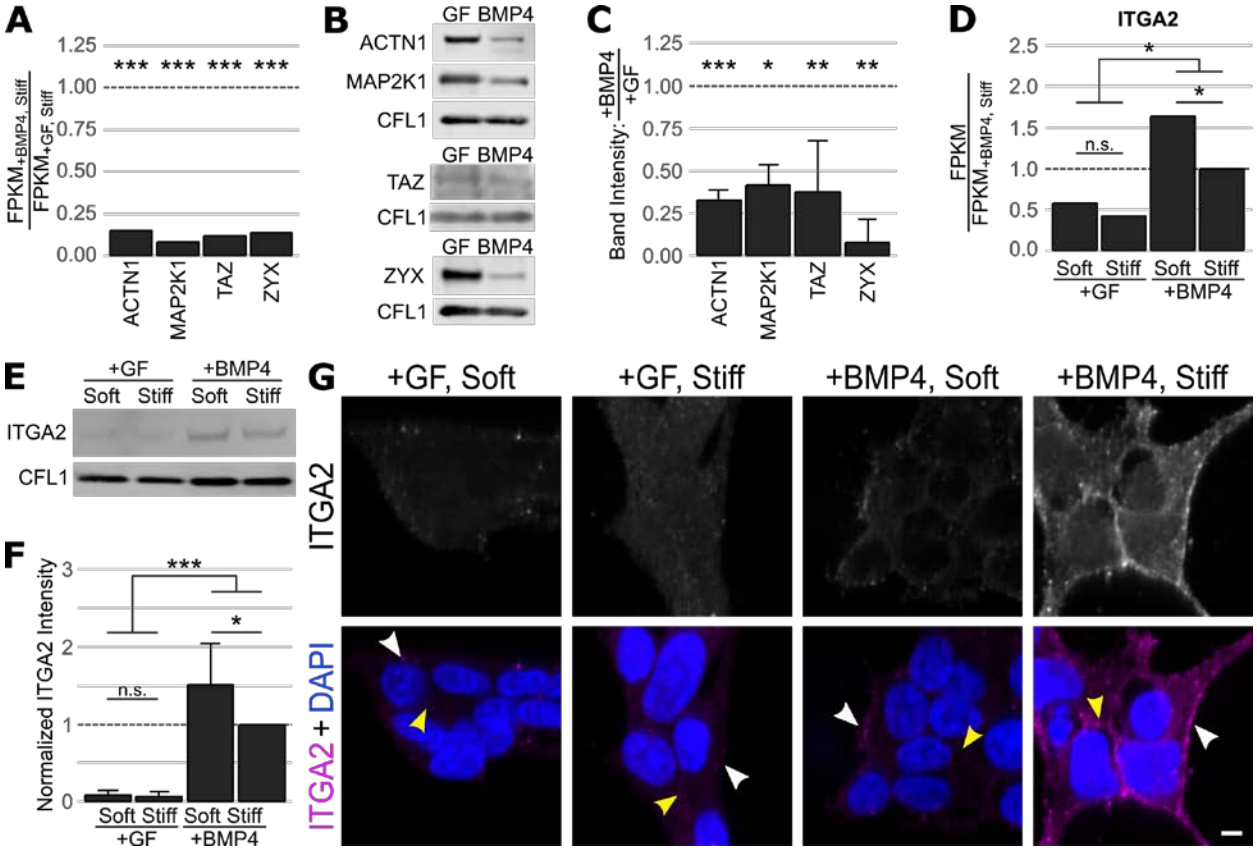

Figure 4.5: RNA sequencing predictions for genes altered by BMP4 treatment hold at the proteomic level. (A) Replotting of RNA sequencing data of targets selected for proteomic confirmation; ratio of FPKM for the BMP4-treated condition to the control GF-enriched condition for cells grown on stiff gels. (B) Representative western blots and (C) quantification for targets shown in (A). Lysates were collected from cells were grown on laminin-coated tissue culture plates for 7 days in either growth factor-enriched conditions (GF) or 100 ng/ml BMP4 (BMP4). Each blot was also probed for cofilin as a loading control. Band intensities were normalized first to cofilin, and then to the intensity of the GF-treated condition. Bars represent mean, error bars represent standard deviation, and p-values were calculated by a Student's t-test (n = 4, 3, 5, 3; respectively, from left to right). (D) Replotting of RNA sequencing data for ITGA2. (E) Representative western blot and (F) quantification for ITGA2. Lysates were collected from cells grown on gels of the denoted stiffness for 7 days in the denoted media condition. Band intensities were normalized first to cofilin and then to the band intensity of the BMP4-treated cells cultured on stiff gels. Bars represent mean, error bars represent standard deviation and asterisks indicate statistically significant differences calculated with a one-way ANOVA followed by Tukey's range test (n = 7). (G) Representative images for cells probed for ITGA2. Arrowheads indicate areas with presence or absence of staining at cell periphery. n.s.: $p > 0.05$, *: $p < 0.05$, **: $p < 0.01$, *** $p < 0.001$.

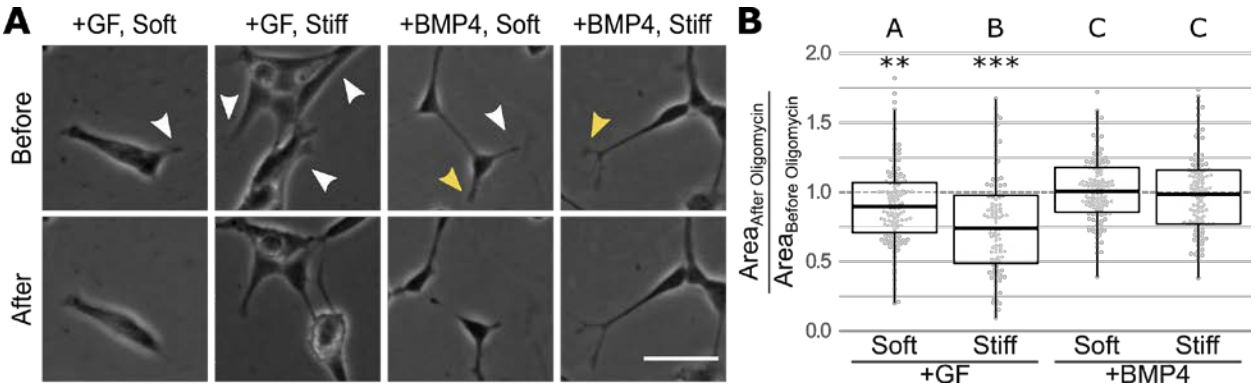

Figure 4.6: Oligomycin inhibition of oxidative phosphorylation influences spreading of stem-like TICs in a stiffness-dependent manner but not differentiated TICs. **(A)** Representative images of TICs prior to and 30 minutes after addition of 5 μM oligomycin. White arrows indicate protrusions that retract after inhibition of ATP synthase, yellow arrows indicate protrusions that showed extension after oligomycin treatment. **(B)** Quantification of cell area changes in response to oligomycin. A ratio of 1 indicates that after 30 minutes in 5 μM oligomycin cells showed no net change in cell area while a ratio of less than 1 indicates a decrease in area. Asterisks indicate ratios statistically distinct from 1, as determined by a 2-sided Mann Whitney U test (n.s.: $p > 0.05$, **: $p < 0.01$, *** $p < 0.001$). Letters indicate statistically distinct ($p_{adj} < 0.05$) distributions as calculated by a Kruskal-Wallis one-way analysis of variance followed by a post-hoc Kruskal Dunn test with Holm's method for adjusting for multiple comparisons. (n = 119, 113, 123, 113 cells per condition, respectively from left to right).

References

1. Shyer AE, et al. (2017) Emergent cellular self-organization and mechanosensation initiate follicle pattern in the avian skin. *Science (80-)* 357(6353):811–815.
2. Paszek MJ, et al. (2005) Tensional homeostasis and the malignant phenotype. *Cancer Cell* 8(3):241–254.
3. Keung AJ, de Juan-Pardo EM, Schaffer D V, Kumar S (2011) Rho GTPases mediate the mechanosensitive lineage commitment of neural stem cells. *Stem Cells* 29(11):1886–97.
4. Na S, et al. (2008) Rapid signal transduction in living cells is a unique feature of mechanotransduction. *Proc Natl Acad Sci* 105(18):6626–6631.
5. Vartak N, Bastiaens P (2010) Spatial cycles in G-protein crowd control. *EMBO J* 29(16):2689–2699.
6. Kinkhabwala A, Bastiaens PI (2010) Spatial aspects of intracellular information processing. *Curr Opin Genet Dev* 20(1):31–40.
7. Inder K, et al. (2008) Activation of the MAPK module from different spatial locations generates distinct system outputs. *Mol Biol Cell* 19(11):4776–84.
8. Toettcher JE, Weiner OD, Lim WA (2013) Using optogenetics to interrogate the dynamic control of signal transmission by the Ras/Erk module. *Cell* 155(6):1422–34.
9. Isenberg BC, DiMilla PA, Walker M, Kim S, Wong JY (2009) Vascular Smooth Muscle Cell Durotaxis Depends on Substrate Stiffness Gradient Strength. *Biophys J* 97(5):1313–1322.
10. Kim D-H, et al. (2009) Mechanosensitivity of fibroblast cell shape and movement to anisotropic substratum topography gradients. *Biomaterials* 30(29):5433–5444.
11. Wang X, Chen X, Yang Y (2012) Spatiotemporal control of gene expression by a light-switchable transgene system. *Nat Methods* 9(3):266–9.
12. Polstein LR, Gersbach CA (2015) A light-inducible CRISPR-Cas9 system for control of endogenous gene activation. *Nat Chem Biol* 11(3):198–200.
13. Shin K-J, et al. (2006) A single lentiviral vector platform for microRNA-based conditional RNA interference and coordinated transgene expression. *Proc Natl Acad Sci* 103(37):13759–13764.
14. Fussenegger M, et al. (2000) Streptogramin-based gene regulation systems for mammalian cells. *Nat Biotechnol* 18(11):1203–8.
15. Braselmann S, Graninger P, Busslinger M (1993) A selective transcriptional induction system for mammalian cells based on Gal4-estrogen receptor fusion proteins. *Proc Natl Acad Sci U S A* 90(5):1657–61.
16. No D, Yao TP, Evans RM (1996) Ecdysone-inducible gene expression in mammalian cells and transgenic mice. *Proc Natl Acad Sci U S A* 93(8):3346–51.
17. Gitzinger M, et al. (2011) The food additive vanillic acid controls transgene expression in mammalian cells and mice. *Nucleic Acids Res* 40(5):e37–e37.
18. Liu HS, Lee CH, Lee CF, Su IJ, Chang TY (1998) Lac/Tet dual-inducible system functions in mammalian cell lines. *Biotechniques* 24(4):624–8, 630–2.
19. MacKay JL, Keung AJ, Kumar S (2012) A genetic strategy for the dynamic and graded control of cell mechanics, motility, and matrix remodeling. *Biophys J* 102(3):434–42.
20. MacKay JL, Kumar S (2014) Simultaneous and independent tuning of RhoA and Rac1 activity with orthogonally inducible promoters. *Integr Biol (Camb)* 6(9):885–94.
21. Javaherian S, Anesiadis N, Mahadevan R, McGuigan AP (2013) Design principles for

generating robust gene expression patterns in dynamic engineered tissues. *Integr Biol* 5(3):578.
22. Zhang Y, Gazit Z, Pelled G, Gazit D, Vunjak-Novakovic G (2011) Patterning osteogenesis by inducible gene expression in microfluidic culture systems. *Integr Biol (Camb)* 3(1):39–47.
23. Deans TL, Singh A, Gibson M, Elisseeff JH (2012) Regulating synthetic gene networks in 3D materials. *Proc Natl Acad Sci U S A* 109(38):15217–22.
24. Baraniak PR, et al. (2011) Spatial control of gene expression within a scaffold by localized inducer release. *Biomaterials* 32(11):3062–3071.
25. Inoue T, Heo W Do, Grimley JS, Wandless TJ, Meyer T (2005) An inducible translocation strategy to rapidly activate and inhibit small GTPase signaling pathways. *Nat Methods* 2(6):415–8.
26. Karginov A V, Ding F, Kota P, Dokholyan N V, Hahn KM (2010) Engineered allosteric activation of kinases in living cells. *Nat Biotechnol* 28(7):743–7.
27. Karginov A V, et al. (2014) Dissecting motility signaling through activation of specific Src-effector complexes. *Nat Chem Biol* 10(4):286–290.
28. Kapp GT, et al. (2012) Control of protein signaling using a computationally designed GTPase/GEF orthogonal pair. *Proc Natl Acad Sci U S A* 109(14):5277–82.
29. Banaszynski LA, Liu CW, Wandless TJ (2005) Characterization of the FKBP·Rapamycin·FRB Ternary Complex. *J Am Chem Soc* 127(13):4715–4721.
30. Feng S, et al. (2014) A rapidly reversible chemical dimerizer system to study lipid signaling in living cells. *Angew Chem Int Ed Engl* 53(26):6720–3.
31. Liu P, et al. (2014) A bioorthogonal small-molecule-switch system for controlling protein function in live cells. *Angew Chem Int Ed Engl* 53(38):10049–55.
32. Miyamoto T, et al. (2012) Rapid and orthogonal logic gating with a gibberellin-induced dimerization system. *Nat Chem Biol* 8(5):465–70.
33. Lin Y-C, et al. (2013) Rapidly reversible manipulation of molecular activity with dual chemical dimerizers. *Angew Chem Int Ed Engl* 52(25):6450–4.
34. Karginov A V, et al. (2011) Light regulation of protein dimerization and kinase activity in living cells using photocaged rapamycin and engineered FKBP. *J Am Chem Soc* 133(3):420–3.
35. Umeda N, Ueno T, Pohlmeyer C, Nagano T, Inoue T (2011) A photocleavable rapamycin conjugate for spatiotemporal control of small GTPase activity. *J Am Chem Soc* 133(1):12–4.
36. Wright CW, Guo Z-F, Liang F-S (2015) Light control of cellular processes by using photocaged abscisic acid. *Chembiochem* 16(2):254–61.
37. Ballister ER, Aonbangkhen C, Mayo AM, Lampson MA, Chenoweth DM (2014) Localized light-induced protein dimerization in living cells using a photocaged dimerizer. *Nat Commun* 5:5475.
38. Lin B, et al. (2012) Synthetic spatially graded Rac activation drives cell polarization and movement. *Proc Natl Acad Sci U S A* 109(52):E3668-77.
39. Park JS, et al. (2014) Synthetic control of mammalian-cell motility by engineering chemotaxis to an orthogonal bioinert chemical signal. *Proc Natl Acad Sci U S A* 111(16):5896–901.
40. Weitzman M, Hahn KM (2014) Optogenetic approaches to cell migration and beyond. *Curr Opin Cell Biol* 30:112–20.

41. Guo Q, et al. (2012) Light activated cell migration in synthetic extracellular matrices. *Biomaterials* 33(32):8040–6.
42. Bryson JB, et al. (2014) Optical control of muscle function by transplantation of stem cell-derived motor neurons in mice. *Science* 344(6179):94–7.
43. Xu Y, et al. (2014) Optogenetic control of chemokine receptor signal and T-cell migration. *Proc Natl Acad Sci U S A* 111(17):6371–6.
44. Bruegmann T, et al. (2010) Optogenetic control of heart muscle in vitro and in vivo. *Nat Methods* 7(11):897–900.
45. Bruegmann T, et al. (2015) Optogenetic control of contractile function in skeletal muscle. *Nat Commun* 6:7153.
46. Sakar MS, et al. (2012) Formation and optogenetic control of engineered 3D skeletal muscle bioactuators. *Lab Chip* 12(23):4976–85.
47. Mills E, Pham E, Truong K (2010) Structure based design of a Ca2+-sensitive RhoA protein that controls cell morphology. *Cell Calcium* 48(4):195–201.
48. Mills E, Pham E, Nagaraj S, Truong K (2012) Engineered Networks of Synthetic and Natural Proteins To Control Cell Migration. *ACS Synth Biol* 1(6):211–220.
49. Pham E, Mills E, Truong K (2011) A synthetic photoactivated protein to generate local or global Ca(2+) signals. *Chem Biol* 18(7):880–90.
50. Mannix RJ, et al. (2008) Nanomagnetic actuation of receptor-mediated signal transduction. *Nat Nanotechnol* 3(1):36–40.
51. Bharde AA, et al. (2013) Magnetic nanoparticles as mediators of ligand-free activation of EGFR signaling. *PLoS One* 8(7):e68879.
52. Chen O, et al. (2014) Magneto-fluorescent core-shell supernanoparticles. *Nat Commun* 5:5093.
53. Etoc F, et al. (2013) Subcellular control of Rac-GTPase signalling by magnetogenetic manipulation inside living cells. *Nat Nanotechnol* 8(3):193–8.
54. Hoffmann C, et al. (2013) Spatiotemporal control of microtubule nucleation and assembly using magnetic nanoparticles. *Nat Nanotechnol* 8(3):199–205.
55. Etoc F, et al. (2015) Magnetogenetic Control of Protein Gradients Inside Living Cells with High Spatial and Temporal Resolution. *Nano Lett* 15(5):3487–3494.
56. Bonnemay L, Hostachy S, Hoffmann C, Gautier J, Gueroui Z (2013) Engineering spatial gradients of signaling proteins using magnetic nanoparticles. *Nano Lett* 13(11):5147–52.
57. Goodwill PW, et al. (2012) X-Space MPI: Magnetic Nanoparticles for Safe Medical Imaging. *Adv Mater* 24(28):3870–3877.
58. Weinberg BH, et al. (2017) Large-scale design of robust genetic circuits with multiple inputs and outputs for mammalian cells. *Nat Biotechnol* 35(5):453–462.
59. del Rio A, et al. (2009) Stretching Single Talin Rod Molecules Activates Vinculin Binding. *Science (80-)* 323(5914):638–641.
60. Giaever G, Nislow C (2014) The yeast deletion collection: a decade of functional genomics. *Genetics* 197(2):451–65.
61. Li Z, et al. (2011) Systematic exploration of essential yeast gene function with temperature-sensitive mutants. *Nat Biotechnol* 29(4):361–367.
62. Baryshnikova A, et al. (2010) Quantitative analysis of fitness and genetic interactions in yeast on a genome scale. *Nat Methods* 7(12):1017–1024.
63. Roberts B, et al. (2017) Systematic gene tagging using CRISPR/Cas9 in human stem cells to illuminate cell organization. *Mol Biol Cell* 28(21):2854–2874.

64. Regev A, et al. The Human Cell Atlas AND HUMAN CELL ATLAS MEETING PARTICIPANTS. Available at: https://doi.org/10.7554/eLife.27041.001 [Accessed April 10, 2018].
65. Wang T, Wei JJ, Sabatini DM, Lander ES (2014) Genetic screens in human cells using the CRISPR-Cas9 system. *Science* 343(6166):80–4.
66. Dupont S, et al. (2011) Role of YAP/TAZ in mechanotransduction. *Nature* 474(7350):179–183.
67. Koike-Yusa H, Li Y, Tan E-P, Velasco-Herrera MDC, Yusa K (2014) Genome-wide recessive genetic screening in mammalian cells with a lentiviral CRISPR-guide RNA library. *Nat Biotechnol* 32(3):267–273.
68. Zhou Y, et al. (2014) High-throughput screening of a CRISPR/Cas9 library for functional genomics in human cells. *Nature* 509(7501):487–491.
69. Kaykas A, Moon RT (2004) A plasmid-based system for expressing small interfering RNA libraries in mammalian cells. *BMC Cell Biol* 5(1):16.
70. Flaim CJ, Chien S, Bhatia SN (2005) An extracellular matrix microarray for probing cellular differentiation. *Nat Methods* 2(2):119–125.
71. Gobaa S, et al. (2011) Artificial niche microarrays for probing single stem cell fate in high throughput. *Nat Methods* 8(11):949–955.
72. Fu J, et al. (2010) Mechanical regulation of cell function with geometrically modulated elastomeric substrates. *Nat Methods* 7(9):733–6.
73. Syed S, Karadaghy A, Zustiak S (2015) Simple polyacrylamide-based multiwell stiffness assay for the study of stiffness-dependent cell responses. *J Vis Exp* (97). doi:10.3791/52643.
74. Semler EJ, Lancin PA, Dasgupta A, Moghe P V. (2005) Engineering hepatocellular morphogenesis and function via ligand-presenting hydrogels with graded mechanical compliance. *Biotechnol Bioeng* 89(3):296–307.
75. Lyra-Leite DM, et al. (2017) Mitochondrial function in engineered cardiac tissues is regulated by extracellular matrix elasticity and tissue alignment. *Am J Physiol Circ Physiol* 313(4):H757–H767.
76. Rape AD, Zibinsky M, Murthy N, Kumar S (2015) A synthetic hydrogel for the high-throughput study of cell–ECM interactions. 6:8129.
77. Vega SL, et al. (2018) Combinatorial hydrogels with biochemical gradients for screening 3D cellular microenvironments. *Nat Commun* 9(1):614.
78. Hadden WJ, et al. (2017) Stem cell migration and mechanotransduction on linear stiffness gradient hydrogels. *Proc Natl Acad Sci* 114(22):5647–5652.
79. Mih JD, et al. (2011) A Multiwell Platform for Studying Stiffness-Dependent Cell Biology. *PLoS One* 6(5):e19929.
80. Ranga A, et al. (2014) 3D niche microarrays for systems-level analyses of cell fate. *Nat Commun* 5:4324.
81. Elosegui-Artola A, et al. (2016) Mechanical regulation of a molecular clutch defines force transmission and transduction in response to matrix rigidity. *Nat Cell Biol* 18(5):540–548.
82. Oria R, et al. (2017) Force loading explains spatial sensing of ligands by cells. *Nature* 552(7684):219.
83. Morimatsu M, Mekhdjian AH, Adhikari AS, Dunn AR (2013) Molecular Tension Sensors Report Forces Generated by Single Integrin Molecules in Living Cells. *Nano Lett* 13(9):3985–3989.

84. Grashoff C, et al. (2010) Measuring mechanical tension across vinculin reveals regulation of focal adhesion dynamics. *Nature* 466(7303):263–266.
85. Borghi N, et al. (2012) E-cadherin is under constitutive actomyosin-generated tension that is increased at cell-cell contacts upon externally applied stretch. *Proc Natl Acad Sci U S A* 109(31):12568–73.
86. HAND AJ, SUN T, BARBER DC, HOSE DR, MACNEIL S (2009) Automated tracking of migrating cells in phase-contrast video microscopy sequences using image registration. *J Microsc* 234(1):62–79.
87. Prager-Khoutorsky M, et al. (2011) Fibroblast polarization is a matrix-rigidity-dependent process controlled by focal adhesion mechanosensing. *Nat Cell Biol* 13(12):1457–65.
88. Sliogeryte K, et al. (2016) Differential effects of LifeAct-GFP and actin-GFP on cell mechanics assessed using micropipette aspiration. *J Biomech* 49(2):310–317.
89. Tanner K, Boudreau A, Bissell MJ, Kumar S (2010) Dissecting regional variations in stress fiber mechanics in living cells with laser nanosurgery. *Biophys J* 99(9):2775–83.
90. Kuribayashi-Shigetomi K, Takahashi R, Subagyo A, Sueoka K, Okajima T (2015) High-throughput Measurements of Single Cell Rheology by Atomic Force Microscopy. *Hyper Bio Assembler for 3D Cellular Systems* (Springer Japan, Tokyo), pp 57–67.
91. Nowell CS, et al. (2016) Chronic inflammation imposes aberrant cell fate in regenerating epithelia through mechanotransduction. *Nat Cell Biol* 18(2):168–180.
92. Benham-Pyle BW, Pruitt BL, Nelson WJ (2015) Cell adhesion. Mechanical strain induces E-cadherin-dependent Yap1 and β-catenin activation to drive cell cycle entry. *Science* 348(6238):1024–7.
93. Lee LM, Lee JW, Chase D, Gebrezgiabhier D, Liu AP (2016) Development of an advanced microfluidic micropipette aspiration device for single cell mechanics studies. *Biomicrofluidics* 10(5):54105.
94. Guo Q, Park S, Ma H (2012) Microfluidic micropipette aspiration for measuring the deformability of single cells. *Lab Chip* 12(15):2687.
95. Guillou L, et al. (2016) Measuring Cell Viscoelastic Properties Using a Microfluidic Extensional Flow Device. *Biophys J* 111(9):2039–2050.
96. Golfier S, et al. (2017) High-throughput cell mechanical phenotyping for label-free titration assays of cytoskeletal modifications. *Cytoskeleton* 74(8):283–296.
97. Kumachev A, et al. (2011) High-throughput generation of hydrogel microbeads with varying elasticity for cell encapsulation. *Biomaterials* 32(6):1477–1483.
98. Rosendahl P, et al. (2018) Real-time fluorescence and deformability cytometry. *Nat Methods*. doi:10.1038/nmeth.4639.
99. Lin J-MG, et al. (2018) Lab on a Chip Linking invasive motility to protein expression in single tumor cells. 18. doi:10.1039/c7lc01008g.
100. Gomez-Cabrero D, et al. (2014) Data integration in the era of omics: current and future challenges. *BMC Syst Biol* 8(Suppl 2):I1.
101. Maglott D, Ostell J, Pruitt KD, Tatusova T (2011) Entrez Gene: gene-centered information at NCBI. *Nucleic Acids Res* 39(Database):D52–D57.
102. Eyre TA, et al. (2006) The HUGO Gene Nomenclature Database, 2006 updates. *Nucleic Acids Res* 34(90001):D319–D321.
103. Caspi R, et al. (2016) The MetaCyc database of metabolic pathways and enzymes and the BioCyc collection of pathway/genome databases. *Nucleic Acids Res* 44(D1):D471-80.
104. Kanehisa M, et al. (2007) KEGG for linking genomes to life and the environment. *Nucleic*

Acids Res 36(Database):D480–D484.
105. Gene Ontology Consortium (2004) The Gene Ontology (GO) database and informatics resource. *Nucleic Acids Res* 32(90001):258D–261.
106. Tomlins P (2016) Practical relevance and interpretation of characterization data. *Characterisation and Design of Tissue Scaffolds* (Elsevier), pp 245–268.
107. Sun M, Spill F, Zaman MH (2016) A Computational Model of YAP/TAZ Mechanosensing. *Biophys J* 110(11):2540–2550.
108. Swift J, et al. (2013) Nuclear lamin-A scales with tissue stiffness and enhances matrix-directed differentiation. *Science (80-)* 341(6149):1240104.
109. Byron KL, Puglisi JL, Holda JR, Eble D, Samarel AM (1996) Myosin heavy chain turnover in cultured neonatal rat heart cells: effects of [Ca2+]i and contractile activity. *Am J Physiol Physiol* 271(5):C1447–C1456.
110. Dingal PCDP, Discher DE (2014) Systems Mechanobiology: Tension-Inhibited Protein Turnover Is Sufficient to Physically Control Gene Circuits. *Biophys J* 107(11):2734–2743.
111. Bangasser BL, et al. (2017) Shifting the optimal stiffness for cell migration. *Nat Commun* 8:15313.
112. Bangasser BL, Odde DJ (2013) Master equation-based analysis of a motor-clutch model for cell traction force. *Cell Mol Bioeng* 6(4):449–459.
113. Oakes PW, et al. (2018) Lamellipodium is a myosin-independent mechanosensor. *Proc Natl Acad Sci U S A* 115(11):2646–2651.
114. Hoffmann M, Schwarz US (2013) A kinetic model for RNA-interference of focal adhesions. *BMC Syst Biol* 7(1):2.
115. Kassianidou E, Brand CA, Schwarz US, Kumar S (2017) Geometry and network connectivity govern the mechanics of stress fibers. *Proc Natl Acad Sci* 114(10):2622–2627.
116. Oakes PW, et al. (2017) Optogenetic control of RhoA reveals zyxin-mediated elasticity of stress fibres. *Nat Commun* 8:15817.
117. McMeeking RM, Deshpande VS (2017) A Bio-chemo-mechanical Model for Cell Contractility, Adhesion, Signaling, and Stress-Fiber Remodeling. *Biomechanics: Trends in Modeling and Simulation* (Springer, Cham), pp 53–81.
118. Pathak A, McMeeking RM, Evans AG, Deshpande VS (2011) An Analysis of the Cooperative Mechano-Sensitive Feedback Between Intracellular Signaling, Focal Adhesion Development, and Stress Fiber Contractility. *J Appl Mech* 78(4):41001.
119. Buganza Tepole A, Kuhl E (2016) Computational modeling of chemo-bio-mechanical coupling: a systems-biology approach toward wound healing. *Comput Methods Biomech Biomed Engin* 19(1):13–30.
120. Buganza Tepole A (2017) Computational systems mechanobiology of wound healing. *Comput Methods Appl Mech Eng* 314:46–70.
121. Szymanski WG, et al. (2015) Cytoskeletal Components Define Protein Location to Membrane Microdomains. *Mol Cell Proteomics* 14(9):2493–509.
122. Loverdo C, Bénichou O, Moreau M, Voituriez R (2008) Enhanced reaction kinetics in biological cells. *Nat Phys* 4(2):134–137.
123. Chaudhuri A, Bhattacharya B, Gowrishankar K, Mayor S, Rao M (2011) Spatiotemporal regulation of chemical reactions by active cytoskeletal remodeling. *Proc Natl Acad Sci* 108(36):14825–14830.
124. Provenzano PP, Inman DR, Eliceiri KW, Keely PJ (2009) Matrix density-induced

mechanoregulation of breast cell phenotype, signaling and gene expression through a FAK–ERK linkage. *Oncogene* 28(49):4326–4343.
125. Dupont S, et al. (2011) Role of YAP/TAZ in mechanotransduction. *Nature* 474(7350):179–184.
126. Steed E, et al. (2016) klf2a couples mechanotransduction and zebrafish valve morphogenesis through fibronectin synthesis. *Nat Commun* 7:11646.
127. McCormick ME, et al. (2017) Spatial phenotyping of the endocardial endothelium as a function of intracardiac hemodynamic shear stress. *J Biomech* 50:11–19.
128. Rolfe RA, et al. (2014) Identification of mechanosensitive genes during skeletal development: alteration of genes associated with cytoskeletal rearrangement and cell signalling pathways. *BMC Genomics* 15(1):48.
129. Kelly NH, Schimenti JC, Ross FP, van der Meulen MCH (2016) Transcriptional profiling of cortical versus cancellous bone from mechanically-loaded murine tibiae reveals differential gene expression. *Bone* 86:22–9.
130. Alam SG, et al. (2016) The mammalian LINC complex regulates genome transcriptional responses to substrate rigidity. *Sci Rep* 6(1):38063.
131. Kuo J-C, Han X, Hsiao C-T, Yates III JR, Waterman CM (2011) Analysis of the myosin-II-responsive focal adhesion proteome reveals a role for β-Pix in negative regulation of focal adhesion maturation. *Nat Cell Biol* 13(4):383–393.
132. Mili S, Moissoglu K, Macara IG (2008) Genome-wide screen reveals APC-associated RNAs enriched in cell protrusions. *Nature* 453(7191):115–119.
133. Wang T, Hamilla S, Cam M, Aranda-Espinoza H, Mili S (2017) Extracellular matrix stiffness and cell contractility control RNA localization to promote cell migration. *Nat Commun* 8(1):896.
134. Moffitt JR, et al. (2016) High-throughput single-cell gene-expression profiling with multiplexed error-robust fluorescence in situ hybridization. *Proc Natl Acad Sci* 113(39):11046–11051.
135. Ingolia NT (2016) Ribosome Footprint Profiling of Translation throughout the Genome. *Cell* 165(1):22–33.
136. Burnette DT, et al. (2014) A contractile and counterbalancing adhesion system controls the 3D shape of crawling cells. *J Cell Biol* 205(1):83–96.
137. Downing TL, et al. (2013) Biophysical regulation of epigenetic state and cell reprogramming. *Nat Mater* 12(12):1154–1162.
138. Tambe DT, et al. (2011) Collective cell guidance by cooperative intercellular forces. *Nat Mater* 10(6):469–475.
139. Heisenberg C-P, Bellaïche Y (2013) Forces in Tissue Morphogenesis and Patterning. *Cell* 153(5):948–962.
140. Tamada M, Perez TD, Nelson WJ, Sheetz MP (2007) Two distinct modes of myosin assembly and dynamics during epithelial wound closure. *J Cell Biol* 176(1):27–33.
141. Soiné JRD, et al. (2014) Model-based traction force microscopy reveals diferential tension in cellular actin bundles. *PLoS Comput Biol*.
142. Kassianidou E, Kumar S (2015) A biomechanical perspective on stress fiber structure and function. *Biochim Biophys Acta - Mol Cell Res* 1853(11, Part B):3065–3074.
143. Chang C-W, Kumar S (2013) Vinculin tension distributions of individual stress fibers within cell-matrix adhesions. *J Cell Sci* 126(Pt 14):3021–30.
144. Lee S, Kumar S (2016) Actomyosin stress fiber mechanosensing in 2D and 3D.

F1000Research 5:F1000 Faculty Rev-2261.
145. Vicente-Manzanares M, Ma X, Adelstein RS, Horwitz AR (2009) Non-muscle myosin II takes centre stage in cell adhesion and migration. *Nat Rev Mol Cell Biol* 10(11):778–90.
146. Beach JR, et al. (2014) Nonmuscle myosin II isoforms coassemble in living cells. *Curr Biol* 24(10):1160–6.
147. SEKINE T, YAMAGUCHI M (1963) Effect of ATP on the Binding of N-Ethylmaleimide to SH Groups in the Active Site of Myosin ATPase. *J Biochem* 54(2):196–198.
148. Wendt T, Taylor D, Trybus KM, Taylor K (2001) Three-dimensional image reconstruction of dephosphorylated smooth muscle heavy meromyosin reveals asymmetry in the interaction between myosin heads and placement of subfragment 2. *Proc Natl Acad Sci* 98(8):4361–4366.
149. Umemoto S, Bengur AR, Sellers JR (1989) Effect of multiple phosphorylations of smooth muscle and cytoplasmic myosins on movement in an in vitro motility assay. *J Biol Chem* 264(3):1431–6.
150. Mizutani T, Haga H, Koyama Y, Takahashi M, Kawabata K (2006) Diphosphorylation of the Myosin Regulatory Light Chain Enhances the Tension Acting on Stress Fibers in Fibroblasts. 731(December 2005):726–731.
151. Kamisoyama H, Araki Y, Ikebe M (1994) Mutagenesis of the Phosphorylation Site (Serine 19) of Smooth Muscle Myosin Regulatory Light Chain and Its Effects on the Properties of Myosin. *Biochemistry* 33(3):840–847.
152. Watanabe T, Hosoya H, Yonemura S (2007) Regulation of Myosin II Dynamics by Phosphorylation and Dephosphorylation of Its Light Chain in Epithelial Cells □. 18(February):605–616.
153. Blue EK, et al. (2002) 220- and 130-kDa MLCKs have distinct tissue distributions and intracellular localization patterns. *Am J Physiol - Cell Physiol* 282(3):C451 LP-C460.
154. Hirano M, Hirano K (2016) Myosin di-phosphorylation and peripheral actin bundle formation as initial events during endothelial barrier disruption. *Sci Rep* 6:20989.
155. Getz TM, Dangelmaier CA, Jin J, Daniel JL, Kunapuli SP (2010) Differential Phosphorylation of Myosin Light Chain (Thr)18 and (Ser)19 and Functional Implications in Platelets. *J Thromb Haemost* 8(10):2283–2293.
156. Ikebe M, Hartshorne DJ, Elzinga M (1986) Identification, phosphorylation, and dephosphorylation of a second site for myosin light chain kinase on the 20,000-dalton light chain of smooth muscle myosin. *J Biol Chem* 261(1):36–39.
157. Ikebe M, Hartshorne DJ (1985) Phosphorylation of smooth muscle myosin at two distinct sites by myosin light chain kinase. *J Biol Chem* 260(18):10027–10031.
158. Newell-Litwa KA, et al. (2015) ROCK1 and 2 differentially regulate actomyosin organization to drive cell and synaptic polarity. *J Cell Biol* 210(2):225–242.
159. Yoneda A, Multhaupt HAB, Couchman JR (2005) The Rho kinases I and II regulate different aspects of myosin II activity. *J Cell Biol* 170(3):443–453.
160. Yoneda A, Ushakov D, Multhaupt HAB, Couchman JR (2007) Fibronectin Matrix Assembly Requires Distinct Contributions from Rho Kinases I and -II. *Mol Biol Cell* 18(1):66–75.
161. Totsukawa G, et al. (2000) Distinct roles of ROCK (Rho-kinase) and MLCK in spatial regulation of MLC phosphorylation for assembly of stress fibers and focal adhesions in 3T3 fibroblasts. *J Cell Biol* 150(4):797–806.
162. Katoh K, Kano Y, Amano M, Kaibuchi K, Fujiwara K (2001) Stress fiber organization

regulated by MLCK and Rho-kinase in cultured human fibroblasts. *Am J Physiol Cell Physiol* 280:1669–1679.
163. Saitoh T, et al. (2001) Differential localization of non-muscle myosin II isoforms and phosphorylated regulatory light chains in human MRC-5 fibroblasts. *FEBS Lett* 509(3):365–9.
164. Sakurada K, Seto M, Sasaki Y (1998) Dynamics of myosin light chain phosphorylation at Ser 19 and Thr 18 / Ser 19 in smooth muscle cells in culture. *Am J Physiol Cell Physiol* 274:1563–1672.
165. Vicente-Manzanares M, Horwitz AR (2010) Myosin light chain mono- and di-phosphorylation differentially regulate adhesion and polarity in migrating cells. *Biochem Biophys Res Commun* 402(3):537–42.
166. Wong SY, et al. (2015) Constitutive activation of myosin-dependent contractility sensitizes glioma tumor-initiating cells to mechanical inputs and reduces tissue invasion. *Cancer Res* 75(6):1113–22.
167. MacKay JL, Kumar S (2014) Simultaneous and independent tuning of RhoA and Rac1 activity with orthogonally inducible promoters. *Integr Biol* 6(9):885–894.
168. Ishizaki T, et al. (1997) p160ROCK, a Rho-associated coiled-coil forming protein kinase, works downstream of Rho and induces focal adhesions. *FEBS Lett* 404(2–3):118–124.
169. Gallagher PJ, Herring BP, Trafny A, Sowadski J, Stull JT (1993) A molecular mechanism for autoinhibition of myosin light chain kinases. *J Biol Chem* 268(35):26578–26582.
170. Leung T, Manser E, Tan L, Lim L (1995) A Novel Serine/Threonine Kinase Binding the Ras-related RhoA GTPase Which Translocates the Kinase to Peripheral Membranes. *J Biol Chem* 270(49):29051–29054.
171. MacKay JL, Sood A, Kumar S (2014) Three-dimensional patterning of multiple cell populations through orthogonal genetic control of cell motility. *Soft Matter* 10(14):2372–80.
172. Hughes JH, Kumar S (2016) Synthetic mechanobiology: engineering cellular force generation and signaling. *Curr Opin Biotechnol* 40:82–89.
173. Smith L, Stull JT (2000) Myosin light chain kinase binding to actin filaments. *FEBS Lett* 480(2):298–300.
174. Chang C-W, Kumar S (2015) Differential Contributions of Nonmuscle Myosin II Isoforms and Functional Domains to Stress Fiber Mechanics. *Sci Rep* 5:13736.
175. Kumar S, et al. (2006) Viscoelastic retraction of single living stress fibers and its impact on cell shape, cytoskeletal organization, and extracellular matrix mechanics. *Biophys J* 90(10):3762–73.
176. Takeo Itoh, Mitsuo Ikebe, Kargacin Gary, Hartshorne David, Kemp Bruce FF (1989) Effects of modulators of myosin light-chain kinase activity in singly smooth muscle cells.
177. Kaneko-Kawano T, et al. (2012) Dynamic Regulation of Myosin Light Chain Phosphorylation by Rho-kinase. *PLoS One* 7(6):e39269.
178. Beach JR, et al. (2017) Actin dynamics and competition for myosin monomer govern the sequential amplification of myosin filaments. *Nat Cell Biol* 19(2):85–93.
179. Mertsch S, Thanos S (2014) Opposing Signaling of ROCK1 and ROCK2 Determines the Switching of Substrate Specificity and the Mode of Migration of Glioblastoma Cells. *Mol Neurobiol* 49(2):900–915.
180. Priya R, et al. (2017) ROCK1 but not ROCK2 contributes to RhoA signaling and NMIIA-mediated contractility at the epithelial zonula adherens. *Mol Biol Cell* 28(1):12—20.

181. Kümper S, et al. (2016) Rho-associated kinase (ROCK) function is essential for cell cycle progression, senescence and tumorigenesis. *Elife* 5:e12203.
182. Wang Y, et al. (2009) ROCK Isoform Regulation of Myosin Phosphatase and Contractility in Vascular Smooth Muscle Cells. *Circ Res* 104(4):531–540.
183. Vasquez CG, Heissler SM, Billington N, Sellers JR, Martin AC (2016) Drosophila non-muscle myosin II motor activity determines the rate of tissue folding. *Elife* 5:e20828.
184. Sweeney HL, Yang Z, Zhi G, Stull JT, Trybus KM (1994) Charge replacement near the phosphorylatable serine of the myosin regulatory light chain mimics aspects of phosphorylation. *Proc Natl Acad Sci U S A* 91(4):1490–1494.
185. Stachowiak MR, et al. (2014) A mechanical-biochemical feedback loop regulates remodeling in the actin cytoskeleton. *Proc Natl Acad Sci U S A* 111(49). doi:10.1073/pnas.1417686111.
186. Stachowiak MR, O'Shaughnessy B (2008) Kinetics of stress fibers. *New J Phys* 10(2):25002.
187. Colombelli J, et al. (2009) Mechanosensing in actin stress fibers revealed by a close correlation between force and protein localization. *J Cell Sci* 122(11):1928–1928.
188. Schwarz AB and US (2007) Coupling biochemistry and mechanics in cell adhesion: a model for inhomogeneous stress fiber contraction. *New J Phys* 9(11):425.
189. Russell RJ, Xia S-L, Dickinson RB, Lele TP (2009) Sarcomere mechanics in capillary endothelial cells. *Biophys J* 97(6):1578–1585.
190. Gallagher PJ, Herring BP, Griffin SA, Stull JT (1991) Molecular characterization of a mammalian smooth muscle myosin light chain kinase. *J Biol Chem* 266(35):23936–23944.
191. Lee JP, Kassianidou E, MacDonald JI, Francis MB, Kumar S (2016) N-terminal Specific Conjugation of Extracellular Matrix Proteins to 2-Pyridinecarboxaldehyde Functionalized Polyacrylamide Hydrogels. *Biomaterials* 102:268–276.
192. Stepanenko AA, Kavsan VM (2014) Karyotypically distinct U251, U373, and SNB19 glioma cell lines are of the same origin but have different drug treatment sensitivities. *Gene* 540(2):263–265.
193. Tseng Q, et al. (2012) Spatial organization of the extracellular matrix regulates cell-cell junction positioning. *Proc Natl Acad Sci U S A* 109(5):1506–11.
194. Isogai T, Danuser G (2018) Discovery of functional interactions among actin regulators by analysis of image fluctuations in an unperturbed motile cell system. *Philos Trans R Soc Lond B Biol Sci* 373(1747):20170110.
195. Gupton SL, Waterman-Storer CM (2006) Spatiotemporal Feedback between Actomyosin and Focal-Adhesion Systems Optimizes Rapid Cell Migration. *Cell* 125(7):1361–1374.
196. Gardel ML, et al. (2008) Traction stress in focal adhesions correlates biphasically with actin retrograde flow speed. *J Cell Biol* 183(6):999–1005.
197. Kenney RE, Hoar PE, Kerrick WG (1990) The relationship between ATPase activity, isometric force, and myosin light-chain phosphorylation and thiophosphorylation in skinned smooth muscle fiber bundles from chicken gizzard. *J Biol Chem* 265(15):8642–9.
198. Kassianidou E, Hughes JH, Kumar S (2017) Activation of ROCK and MLCK tunes regional stress fiber formation and mechanics via preferential myosin light chain phosphorylation. *Mol Biol Cell*:mbc.E17-06-0401.
199. Chan CE, Odde DJ (2008) Traction Dynamics of Filopodia on Compliant Substrates. *Science (80-)* 322(5908):1687–1691.

200. Herring BP, El-Mounayri O, Gallagher PJ, Yin F, Zhou J (2006) Regulation of myosin light chain kinase and telokin expression in smooth muscle tissues. *Am J Physiol Cell Physiol* 291(5):C817-27.
201. Chen M, et al. (2013) Regulation of 130-kDa smooth muscle myosin light chain kinase expression by an intronic CArG element. *J Biol Chem* 288(48):34647–57.
202. Verin AD, et al. (1998) Expression of a Novel High Molecular-Weight Myosin Light Chain Kinase in Endothelium. *Am J Respir Cell Mol Biol* 19(5):758–766.
203. Isotani E, et al. (2004) Real-time evaluation of myosin light chain kinase activation in smooth muscle tissues from a transgenic calmodulin-biosensor mouse. *Proc Natl Acad Sci U S A* 101(16):6279–84.
204. Chen C, et al. (2014) Myosin light chain kinase (MLCK) regulates cell migration in a myosin regulatory light chain phosphorylation-independent mechanism. *J Biol Chem* 289(41):28478–88.
205. Yin F, Hoggatt AM, Zhou J, Herring BP (2006) 130-kDa smooth muscle myosin light chain kinase is transcribed from a CArG-dependent, internal promoter within the mouse mylk gene. *AJP Cell Physiol* 290(6):C1599–C1609.
206. Somlyo A V., et al. (2004) Myosin light chain kinase knockout. *J Muscle Res Cell Motil* 25(3):241–242.
207. He W, et al. (2008) Myosin Light Chain Kinase Is Central to Smooth Muscle Contraction and Required for Gastrointestinal Motility in Mice. *Gastroenterology* 135(2):610–620.e2.
208. Bain J, Mclauchlan H, Elliott M, Cohen P (2003) The specificities of protein kinase inhibitors : an update. *Biochem J* 371:199–204.
209. Saitoh M, Ishikawa T, Matsushima S, Naka M, Hidaka H (1987) Selective inhibition of catalytic activity of smooth muscle myosin light chain kinase. *J Biol Chem* 262(16):7796–801.
210. Dulyaninova NG, Patskovsky Y V, Bresnick AR (2004) The N-terminus of the long MLCK induces a disruption in normal spindle morphology and metaphase arrest. *J Cell Sci* 117(8):1481–1493.
211. Kim DY, Helfman DM (2016) Loss of MLCK leads to disruption of cell–cell adhesion and invasive behavior of breast epithelial cells via increased expression of EGFR and ERK/JNK signaling. *Oncogene* 35(34):4495–4508.
212. Ammit AJ, Armour CL, Black JL (2000) Smooth-muscle myosin light-chain kinase content is increased in human sensitized airways. *Am J Respir Crit Care Med* 161(1):257–263.
213. Amano M, et al. (1996) Phosphorylation and activation of myosin by Rho-associated kinase (Rho-kinase). *J Biol Chem* 271(34):20246–9.
214. Heigwer F, Kerr G, Boutros M (2014) E-CRISP: fast CRISPR target site identification. *Nat Methods* 11(2):122–123.
215. Sanjana NE, Shalem O, Zhang F (2014) Improved vectors and genome-wide libraries for CRISPR screening. *Nat Methods* 11(8):783–784.
216. Guen VJ, et al. (2017) EMT programs promote basal mammary stem cell and tumor-initiating cell stemness by inducing primary ciliogenesis and Hedgehog signaling. *Proc Natl Acad Sci U S A* 114(49):E10532–E10539.
217. Dewitt M, Wong J (2015) Cas9 RNP nucleofection for cell lines using Lonza 4D Nucleofector. *Protocols.io* March 20th:10–11.
218. Schneider CA, Rasband WS, Eliceiri KW (2012) NIH Image to ImageJ: 25 years of image

analysis. *Nat Methods* 9(7). doi:10.1038/nmeth.2089.
219. Schindelin J, et al. (2012) Fiji: an open-source platform for biological-image analysis. *Nat Methods* 9(7):676–682.
220. Sage D, Neumann FR, Hediger F, Gasser SM, Unser M (2005) Automatic tracking of individual fluorescence particles: application to the study of chromosome dynamics. *IEEE Trans Image Process* 14(9):1372–1383.
221. Chen J, et al. (2012) A restricted cell population propagates glioblastoma growth after chemotherapy. *Nature* 488. doi:10.1038/nature11287.
222. Nassar D, Blanpain C (2016) Cancer Stem Cells: Basic Concepts and Therapeutic Implications. *Annu Rev Pathol Mech Dis* 11(1):47–76.
223. Lathia JD, Mack SC, Mulkearns-Hubert EE, Valentim CLL, Rich JN (2015) Cancer stem cells in glioblastoma. *Genes Dev* 29(12):1203–17.
224. Deleyrolle LP, et al. (2011) Evidence for label-retaining tumour-initiating cells in human glioblastoma. *Brain* 134(5):1331–1343.
225. Galli R, et al. (2004) Isolation and Characterization of Tumorigenic, Stem-like Neural Precursors from Human Glioblastoma. *Cancer Res* 64:7011–7021.
226. Lathia JD, et al. (2011) Direct In Vivo Evidence for Tumor Propagation by Glioblastoma Cancer Stem Cells. *PLoS One* 6(9):e24807.
227. Piccirillo SGM, et al. (2006) Bone morphogenetic proteins inhibit the tumorigenic potential of human brain tumour-initiating cells. *Nature* 444(7120):761–765.
228. Lim DA, et al. (2007) Relationship of glioblastoma multiforme to neural stem cell regions predicts invasive and multifocal tumor phenotype. *Neuro Oncol* 9(4):424–429.
229. Sanai N, Alvarez-Buylla A, Berger MS (2005) Neural Stem Cells and the Origin of Gliomas. *N Engl J Med* 353(8):811–822.
230. Quiñones-Hinojosa A, Chaichana K (2007) The human subventricular zone: A source of new cells and a potential source of brain tumors. *Exp Neurol* 205(2):313–324.
231. Chin LK, Xia Y, Discher DE, Janmey PA (2016) Mechanotransduction in cancer. *Curr Opin Chem Eng* 11:77–84.
232. Saha K, et al. (2008) Substrate Modulus Directs Neural Stem Cell Behavior. *Biophys J* 95(9):4426–4438.
233. Dellatore SM, Garcia AS, Miller WM (2008) Mimicking stem cell niches to increase stem cell expansion. *Curr Opin Biotechnol* 19(5):534–540.
234. Chen J, Kumar S (2017) Biophysical regulation of cancer stem/initiating cells: Implications for disease mechanisms and translation. *Curr Opin Biomed Eng* 1:87–95.
235. Miroshnikova YA, et al. (2016) Tissue mechanics promote IDH1-dependent HIF1α–tenascin C feedback to regulate glioblastoma aggression. *Nat Cell Biol* 18(12):1336–1345.
236. Tan Y, et al. (2014) Matrix softness regulates plasticity of tumour-repopulating cells via H3K9 demethylation and Sox2 expression. *Nat Commun* 5:4619.
237. Pang M-F, et al. (2016) Tissue Stiffness and Hypoxia Modulate the Integrin-Linked Kinase ILK to Control Breast Cancer Stem-like Cells. *Cancer Res* 76(18):5277–87.
238. Grundy TJ, et al. (2016) Differential response of patient-derived primary glioblastoma cells to environmental stiffness. *Sci Rep* 6:23353.
239. Ruiz-Ontañon P, et al. (2013) Cellular plasticity confers migratory and invasive advantages to a population of glioblastoma-initiating cells that infiltrate peritumoral tissue. *Stem Cells* 31(6):1075–85.
240. Jabbari E, Sarvestani SK, Daneshian L, Moeinzadeh S (2015) Optimum 3D matrix

stiffness for maintenance of cancer stem cells is dependent on tissue origin of cancer cells. *PLoS One* 10(7). doi:10.1371/journal.pone.0132377.
241. Tan Y, et al. (2014) Matrix softness regulates plasticity of tumour-repopulating cells via H3K9 demethylation and Sox2 expression. *Nat Commun* 5. doi:10.1038/ncomms5619.
242. Nakada M, et al. (2013) Integrin α3 is overexpressed in glioma stem-like cells and promotes invasion. *Br J Cancer* 108(12):2516–2524.
243. Lathia JD, et al. (2010) Integrin alpha 6 regulates glioblastoma stem cells. *Cell Stem Cell* 6(5):421–32.
244. Riemenschneider MJ, Mueller W, Betensky RA, Mohapatra G, Louis DN (2005) In Situ Analysis of Integrin and Growth Factor Receptor Signaling Pathways in Human Glioblastomas Suggests Overlapping Relationships with Focal Adhesion Kinase Activation. *Am J Pathol* 167(5):1379–1387.
245. Thomas D, et al. (2016) Increased cancer stem cell invasion is mediated by myosin IIB and nuclear translocation. *Oncotarget* 7(30):47586–47592.
246. Munthe S, et al. (2016) Glioma cells in the tumor periphery have a stem cell phenotype. *PLoS One* 11(5). doi:10.1371/journal.pone.0155106.
247. Bleau A-M, et al. (2009) PTEN/PI3K/Akt Pathway Regulates the Side Population Phenotype and ABCG2 Activity in Glioma Tumor Stem-like Cells. *Cell Stem Cell* 4(3):226–235.
248. Ulrich TA, de Juan Pardo EM, Kumar S (2009) The Mechanical Rigidity of the Extracellular Matrix Regulates the Structure, Motility, and Proliferation of Glioma Cells. *Cancer Res* 69(10):4167–4174.
249. Bond AM, Bhalala OG, Kessler JA (2012) The dynamic role of bone morphogenetic proteins in neural stem cell fate and maturation. *Dev Neurobiol* 72(7):1068–1084.
250. Halder G, Dupont S, Piccolo S (2012) Transduction of mechanical and cytoskeletal cues by YAP and TAZ. *Nat Rev Mol Cell Biol* 13(9):591–600.
251. Suvà ML, et al. (2014) Reconstructing and Reprogramming the Tumor-Propagating Potential of Glioblastoma Stem-like Cells. *Cell* 157(3):580–594.
252. Sung CK, Li D, Andrews E, Drapkin R, Benjamin T (2013) Promoter methylation of the SALL2 tumor suppressor gene in ovarian cancers. *Mol Oncol* 7(3):419–427.
253. Hermosilla VE, et al. (2017) Developmental SALL2 transcription factor: A new player in cancer. *Carcinogenesis* 38(7):680–690.
254. Sung CK, Yim H (2015) The tumor suppressor protein p150Sal2 in carcinogenesis. *Tumor Biol* 36(2):489–494.
255. Zanconato F, et al. (2015) Genome-wide association between YAP/TAZ/TEAD and AP-1 at enhancers drives oncogenic growth. *Nat Cell Biol* 17(9):1218–1227.
256. Takada Y, Ye X, Simon S (2007) The integrins. *Genome Biol* 8(5). doi:10.1186/gb-2007-8-5-215.
257. Ramirez NE, et al. (2011) The α 2 β 1 integrin is a metastasis suppressor in mouse models and human cancer. *J Clin Invest* 121(1):226–237.
258. Zutter MM, Mazoujian G, Santoro S a (1990) Decreased expression of integrin adhesive protein receptors in adenocarcinoma of the breast. *Am J Pathol* 137(4):863–870.
259. Jovanović B, et al. (2014) Transforming growth factor beta receptor type III is a tumor promoter in mesenchymal-stem like triple negative breast cancer. *Breast Cancer Res* 16(4):R69.
260. Symersky J, Osowski D, Walters DE, Mueller DM (2012) Oligomycin frames a common

drug-binding site in the ATP synthase. *Proc Natl Acad Sci U S A* 109(35):13961–5.
261. Cerniglia GJ, et al. (2015) The PI3K/Akt Pathway Regulates Oxygen Metabolism via Pyruvate Dehydrogenase (PDH)-E1alpha Phosphorylation. *Mol Cancer Ther* 14(8):1928–1938.
262. Elstrom RL, et al. (2004) Akt Stimulates Aerobic Glycolysis in Cancer Cells. *Cancer Res* 64(11):3892–3899.
263. Sarosiek KA, Ni Chonghaile T, Letai A (2013) Mitochondria: Gatekeepers of response to chemotherapy. *Trends Cell Biol* 23(12):612–619.
264. Venneti S, Thompson CB (2017) Metabolic Reprogramming in Brain Tumors. *Annu Rev Pathol Mech Dis* 12(1):515–545.
265. Vlashi E, et al. (2011) Metabolic state of glioma stem cells and nontumorigenic cells. *Proc Natl Acad Sci* 108(38):16062–16067.
266. Bartolák-Suki E, Imsirovic J, Nishibori Y, Krishnan R, Suki B (2017) Regulation of Mitochondrial Structure and Dynamics by the Cytoskeleton and Mechanical Factors. *Int J Mol Sci* 18(8). doi:10.3390/ijms18081812.
267. Tung JC, et al. (2015) Tumor mechanics and metabolic dysfunction. *Free Radic Biol Med* 79:269–280.
268. Zanotelli MR, et al. (2018) Regulation of ATP utilization during metastatic cell migration by collagen architecture. *Mol Biol Cell* 29(1):1–9.
269. Bays JL, Campbell HK, Heidema C, Sebbagh M, DeMali KA (2017) Linking E-cadherin mechanotransduction to cell metabolism through force-mediated activation of AMPK. *Nat Cell Biol* 19(6):724–731.
270. Hu H, et al. (2016) Phosphoinositide 3-Kinase Regulates Glycolysis through Mobilization of Aldolase from the Actin Cytoskeleton. *Cell* 164(3):433–446.
271. Tharp KM, et al. (2018) Actomyosin-Mediated Tension Orchestrates Uncoupled Respiration in Adipose Tissues. *Cell Metab* 27(3):602–615.e4.
272. Ozawa S, et al. (2015) Glycolysis, but not Mitochondria, responsible for intracellular ATP distribution in cortical area of podocytes. *Sci Rep* 5. doi:10.1038/srep18575.
273. Carén H, et al. (2015) Glioblastoma Stem Cells Respond to Differentiation Cues but Fail to Undergo Commitment and Terminal Cell-Cycle Arrest. *Stem Cell Reports* 5(5):829–842.
274. Berezovsky AD, et al. (2014) Sox2 promotes malignancy in glioblastoma by regulating plasticity and astrocytic differentiation. *Neoplasia (United States)* 16(3):193–206.
275. Carén H, Beck S, Pollard SM (2016) Differentiation therapy for glioblastoma – too many obstacles? *Mol Cell Oncol* 3(2):e1124174.
276. Safa AR, Saadatzadeh MR, Cohen-Gadol AA, Pollok KE, Bijangi-Vishehsaraei K (2015) Glioblastoma stem cells (GSCs) epigenetic plasticity and interconversion between differentiated non-GSCs and GSCs. *Genes Dis* 2(2):152–163.
277. Streitberger KJ, et al. (2014) High-resolution mechanical imaging of glioblastoma by multifrequency magnetic resonance elastography. *PLoS One* 9(10). doi:10.1371/journal.pone.0110588.
278. Acerbi I, et al. (2015) Human breast cancer invasion and aggression correlates with ECM stiffening and immune cell infiltration. *Integr Biol* 7(10):1120–1134.
279. Bioinformatics B FastQC: a quality control tool for high throughput sequence data. Available at: http://www.bioinformatics.bbsrc.ac.uk/projects/fastqc/.
280. Kim D, et al. (2013) TopHat2: accurate alignment of transcriptomes in the presence of

insertions, deletions and gene fusions. *Genome Biol* 14(4):R36.
281. Trapnell C, et al. (2012) Differential analysis of gene regulation at transcript resolution with RNA-seq. *Nat Biotechnol* 31. doi:10.1038/nbt.2450.
282. Jiao X, et al. (2012) DAVID-WS: a stateful web service to facilitate gene/protein list analysis. *Bioinformatics* 28(13):1805–6.